

Fabrication of Surface Assisted Liquid Manipulation Systems

by

M. Zeeshan Rashid

A Dissertation Submitted to the
Graduate School of Sciences and Engineering
in Partial Fulfillment of the Requirements for

the Degree of

Doctor of Philosophy

in

Electrical and Electronics Engineering



August 13, 2018

Fabrication of Surface Assisted Liquid Manipulation Systems

Koç University

Graduate School of Sciences and Engineering

This is to certify that I have examined this copy of a doctoral dissertation by


M. Zeeshan Rashid

and have found that it is complete and satisfactory in all respects,
and that any and all revisions required by the final
examining committee have been made.

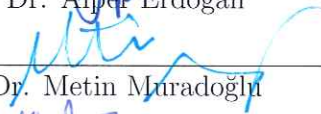
Committee Members:



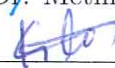
Prof. Dr. Alper Kiraz



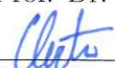
Prof. Dr. Alper Erdoğan



Prof. Dr. Metin Muradoğlu



Assist. Prof. Dr. Kenan Çiçek



Assist. Prof. Dr. Ahmet Erten

Date:

13/08/2018

To my teachers and beloved parents

ABSTRACT

In this thesis, controlled motion of various polar liquids along patterned tracks defined over certain polymer surfaces is demonstrated. The liquid motion along the tracks is maintained due to their relatively hydrophilic (water attractive) nature as compared to the surrounding hydrophobic (water repellent) region. As a result, liquid, either in the form of droplets or bulk, is driven along the tracks in the direction of external pressure flow. Such polymer microfluidic devices are fabricated using polydimethylsiloxane (PDMS) which allows easy handling, artificial roughness addition, reconfigurability, nontoxic nature and sensitivity to certain external stimulus.

Fabrication of reconfigurable polymer surfaces are demonstrated which switch their wettability from superhydrophobic to superhydrophilic upon exposure to oxygen plasma and return to their original state after appropriate thermal treatment for many cycles. This is a purely chemical process taking place due to the migration of functional groups from surface to the bulk and vice versa which causes dramatic transition of wetting state and also allows absolute recovery of surface hydrophobicity. Wetting properties of these surfaces are determined by measuring their static, advancing and receding water contact angle. A specific PDMS mask with narrow openings is developed which allows selective exposure to the surface to make hydrophilic channels. Over these channels, water filaments are produced due to surface tension driven transport phenomenon from one side called input reservoir to the other side, output reservoir. Those patterns are absolutely erasable by thermal treatment, so that, new patterns can be made in the same way for many times.

Hydrophilic tracks can also be defined by exposing PDMS-coated glass slides via

laser ablation which is an irreversible process and only changes the topography. Laser ablation is a process of exposure of a high power extremely focused laser pulses to remove PDMS coating, thus, uncovering the glass substrate. Since the wettability contrast is not too much, instead of surface driven transport, this protocol is adopted to manipulate droplets of nanoliter volume immersed in oil in a closed microfluidic environment. The difference in wettability of glass and PDMS surfaces together with the shallow step-like transverse topographical profile of the ablated tracks allow polar droplets wetting preferentially the glass surface to follow the track. Droplets with smaller wettability are found to be unguided even in the presence of topographic step. Based on this phenomenon, passive sorting of microdroplets of different chemistry injected in the same microfluidic chip is also explored. A comprehensive experimental and theoretical study is done with different droplet liquids, flow speeds and geometry of guiding tracks to gain deep and detailed understanding of the system.

Liquid filaments over patterned surface are of paramount importance in photonics for fabricating fluidic optical waveguides. Guiding of light through these liquid waveguides can benefit bio-sensing, bio-lasing mostly within the visible spectrum in a highly efficient way. The theoretical implementation of an optofluidic rhodamine B dye laser based on holey fiber is demonstrated in the last chapter of the thesis. Conventional dye laser is also modeled for a comparison with the fiber laser. It is concluded that a specific fiber based variant of dye laser is superior to the conventional dye laser for having smaller lasing threshold and higher slope efficiency. These types of fluidic lasers can also be established by fluidic waveguiding over reconfigurable patterned surfaces.

ÖZETÇE

Bu tezde, belirli polimer yüzeyler üzerinde tanımlanan desenli paletler boyunca çeşitli polar sıvıların kontrollü hareketi gösterilmiştir. Yüzey boyunca sıvı hareketi, çevredeki hidrofobik (su itici) bölgeye kıyasla nispeten hidrofilik (su çekici) tabiatlarına bağlı olarak korunur. Sonuç olarak, ya damlacıklar ya da yığınlar halinde sıvı, dış basınç akışı yönünde yüzey boyunca sürülür. Bu tür polimer mikroakışkan cihazlar, kolay kullanım, yapay pürüzlülük ilavesi, yeniden yapılandırılabilirlik, ve belirli dış uyaranlara karşı hassasiyet sağlayan ve toksik olmayan bir malzeme olan polidimetil siloksan (PDMS) kullanılarak imal edilir.

Yeniden yapılandırılabilir polimer yüzeylerin üretilmesi, süperhidrofobikten süperhidrofilliğe kadar ıslanabilmelerini; oksijen plazmasına maruz bırakarak değiştirerek, birçok döngü için uygun ısıl işlemde sonra orijinal hallerine geri dönecek şekilde tanımlanabilir. Bu, fonksiyonel grupların yüzeyden kütleye göç etmesinden dolayı meydana gelen tamamen kimyasal bir işlemdir ve bunun tersi, ıslatma durumunun dramatik geçişine neden olur ve ayrıca yüzey hidrofobisitesinin mutlak olarak geri kazanılmasına izin verir. Bu yüzeylerin ıslanma özellikleri, statik, ilerleyen ve azalan su temas açıları ölçülerek belirlenir. Dar açıklıklara sahip spesifik bir PDMS maskesi, hidrofilik kanalların yapılması için yüzeye seçici maruz kalmaya imkan verecek şekilde geliştirilmiştir. Bu kanallar üzerinden, su filamanları, bir taraftan giriş rezervuarı olarak adlandırılan diğer tarafa, çıkış rezervuarına, yüzey gerilimi ile taşınan nakil olayı nedeniyle üretilmektedir. Bu modeller ısıl işlemle tamamen silinebilir, böylece yeni desenler birçok kez aynı şekilde yapılabilir.

Hidrofilik yüzeyler ayrıca; PDMS-kaplanmış cam altlıkların geri dönüşümsüz bir

işlem olan ve yalnızca topografiyi değiştiren lazer ablasyonu işlemine maruz kalması ile açıklanabilir. Lazer ablasyonu, PDMS kaplamasını kaldırmak ve böylece cam substratı açığa çıkarmak için yüksek güçlü, son derece odaklanmış bir lazer ışınının uygulandığı bir işlemdir. Islatılabilirlik kontrastı çok fazla olmadığı için, yüzey güdümlü nakil yerine bu protokol, kapalı bir mikroakışkan ortamda yağa batırılmış nanolitre hacimli damlacıklarını manipüle etmek için benimsenmiştir. Camın ve PDMS yüzeylerinin ıslatılabilirliğindeki fark, lazer ablasyonuna uğramış yüzeylerin, yüzeysel basamaksı enine topografik profili ile birlikte, polar damlacıkların, cam yüzeyini tercihen yüzeyi takip etmek için ıslatmasına izin verir. Topografik adımın varlığında bile daha küçük ıslanabilirlik içeren damlacıkların güdümsüz olduğu bulunmuştur. Bu fenomene dayanarak, aynı mikroakışkan çipte enjekte edilen farklı kimyasalların mikro damlacıklarının pasif ayıklanması da araştırılmaktadır. Sistemin derin ve ayrıntılı anlaşılması için farklı damlacık sıvıları, akış hızları ve kılavuz rayların geometrisi ile kapsamlı bir deneysel ve teorik çalışma yapılmıştır.

Desenli yüzey üzerindeki sıvı filamentler, akışkan optik dalga kılavuzlarının üretilmesi için çok önemlidir. Bu sıvı dalga kılavuzları aracılığıyla ışığın yönlendirilmesi, biyo-algılama, biyo-lasing'i çoğunlukla görünür spektrumda oldukça verimli bir şekilde kullanabilir. Tezin son bölümünde holey fiberine dayanan optofluidrodamin B boya lazerin teorik uygulaması gösterilmiştir. Geleneksel boya lazeri ayrıca fiber lazeri ile bir karşılaştırma için modellenmiştir. Boya lazerinin spesifik bir fiber bazlı varyantının, daha küçük lasing eşiği ve daha yüksek eğim verimi elde etmek için geleneksel boya lazerinden üstün olduğu sonucuna varılmıştır. Bu tip akışkan lazerler, yeniden yapılandırılabilir desenli yüzeyler üzerinde akışkan dalga kılavuzlamasıyla da oluşturulabilir.

ACKNOWLEDGMENTS

I would like to express my deepest gratitude to my advisor Prof. Dr. Alper Kiraz for giving me the opportunity to work with him, his guidance and the experiences I earned throughout my studies during the past four years. I thank him for his confidence, guidance and continuous support and for his way of solving problems.

Specifically, I thank Prof. Dr. Iskendr Yilgor for guiding me towards fabricating reconfigurable polymer surfaces and study the chemical changes taking place after exposure to certain stimulus. I thank Dr. Alexandr Jonas for his great contribution in understanding droplet tracking algorithms, physics of microdroplets, scientific writing and learning surface chemistry. I thank Dr. Ahmet Erten for his help in explaining the theory of microfluidics, fabricating droplet microfluidic devices and his expertise in microdroplet experiments. I would like to thank Profs. Alper Erdoğan, Metin Muradoğlu, Kenan Çiçek and Ahmet Erten for joining my thesis committee.

I would like to express my gratitude to former and current members of Kirazlab who produced a productive research environment, discussed and suggested innovative ideas and being good friends and helpful coworkers. Specifically, Dr. Mehdi Aas, Dr. Asuman Aşıkoğlu Bozkurt, Dr. Suman Anand, Dr. Berna Morova, Dr. Mustafa Eryurek, Ayşenur Eser, Adil Mustafa, Rana Muhammad Armaghan Ayaz, Nima Bavili, Ahmet Burak Gököz, Berk Zengin, Ömer Yaman, Ateeq Ur Rehman and Gamze Gül. I would like to also thank Dr. Barış Yağci and Dr. Selçuk Çakmak for their interest, help, and support in many different parts of my thesis. I would like to express my appreciation to my friends Anwaar Nazeer, Rehan Chaudhary, Aatif Ejaz, Shoaib Soomro, Shadi Khan, Haris Shehzad Marwat, Muhammad Zakwan, Im-

ran Khan, Talha Irfan Khan, Zaheer Ahmed, Hamza Humayun, Adeel Afridi, Umair Akbar and Syed Sultan Shah Bukhari for their selfless support and discussions related not only to research but also to life itself.

I thank HEC Pakistan for Ph.D. scholarship and I thank my dearest friend Dr. Ghulam Amjad Hussain for helping me in completing the legal documents and other requirements for availing the funding opportunity.

I am grateful to my parents in law, Muhammad Riaz Ahmed and Naseem Akhter for their love and prayers over the last few years. I am also lucky to have wonderful brothers in law Kashif Riaz, Asif Riaz and Aatif Riaz whose care and best wishes are always with me. I would like to thank my brother Rizwan Rashid for his constant support and encouragement throughout my life. I express my deep gratitude to my wife, Gul-e-Nayab, who has enriched all aspects of my life in the last seven years. It is hard to explain that, without her constant love and support, the completion of thesis would not be possible. Finally, I do not have words to express my thankfulness to my parents, Rashid Iqbal and Yasmeen Akhter, as I would not be able to reach this level today without their guidance and prayers.

TABLE OF CONTENTS

List of Figures	xii
Nomenclature	xx
Chapter 1: Introduction	1
1.1 Polymer Surfaces with Switchable Wettability	1
1.1.1 Literature Review	2
1.1.2 Erasable Patterning of Liquid Filaments	4
1.2 Droplet Microfluidics	5
1.2.1 Literature Review	7
1.3 Optofluidics	9
1.4 Thesis Organization	12
Chapter 2: Reversible Switching of Wetting Properties for Erasable Patterned Surface Microfluidics	13
2.1 Preparation of Polymeric Coatings	14
2.2 Surface Characterization Techniques	14
2.3 Results and Discussion	15
2.3.1 Oxygen Plasma Treatment and Thermal Annealing	17
2.3.2 Annealing of Polymers with Time	19
2.3.3 Characterization of Surface Chemical Composition	20
2.3.4 Characterization of Surface Texture and Topography	27
2.3.5 Rewritable Hydrophilic Channels	28

Chapter 3:	Guiding of Emulsion Droplets Along Optically Patterned Shallow Tracks	31
3.1	Preparation of Microfluidic Chips with Droplet Guiding Tracks	32
3.2	Emulsion Systems Used in Droplet Experiments	35
3.3	Computational Fluid Dynamics Study	36
3.3.1	Solver Settings	37
3.3.2	Governing Equations	37
3.3.3	Computational Domain and Boundary Conditions	38
3.3.4	Mesh Dependency	39
3.4	Results and Discussion	40
3.4.1	Experiments With Different Depths of the Wetting Track . . .	41
3.4.2	Numerical Results of Droplet Guiding	47
3.4.3	Experiments With Other Droplet Liquids	48
Chapter 4:	Passive Sorting of Emulsion Droplets	53
4.1	Materials and Methods	54
4.2	Modeling	56
4.2.1	Volume of a Flattened Droplet	57
4.2.2	Surface Area of a Flattened Droplet	60
4.2.3	Confinement Force Due to Droplet Shape	62
4.2.4	Equations of Motion	63
4.3	Results and Discussion	64
Chapter 5:	Modeling of Optofluidic Holey Fiber Dye Laser	68
5.1	Geometry of Holey Fibers and Characterization of Their Guided Modes	70
5.2	Modeling of Holey Fiber Dye Lasers	72
5.2.1	Spatial Variations of Upper Lasing Level Population	75
5.2.2	Spatial Variations of Pump and Signal Powers	76

5.2.3	Threshold Pump Power and Slope Efficiency	79
5.2.4	Optofluidic Fiber Dye Laser Summary	81
5.3	Modeling of Conventional Dye Jet Lasers	82
Chapter 6:	Conclusion and Outlook	85
Chapter 7:	Appendix	90
7.1	Droplet Tracking Algorithm	90
Bibliography		101

LIST OF FIGURES

2.1	Schematic representation of the processes used for the preparation of rewritable hydrophilic channels.	14
2.2	SEM images of (a) virgin PMMA and (b) superhydrophobic PMMA.	16
2.3	Water droplet on (a) PMMA and (b) TPSC surfaces after oxygen plasma treatment and thermal annealing.	17
2.4	Reversible switching of wetting properties of (a) PMMA and (b) TPSC surfaces upon cyclic exposure to oxygen plasma followed by thermal annealing.	18
2.5	Water droplet on (a) SHPMMA and (b) SHTPSC surfaces after oxygen plasma treatment and thermal annealing.	18
2.6	Reversible switching of wetting properties of (a) SHPMMA and (b) SHTPSC surfaces upon cyclic exposure to oxygen plasma followed by thermal annealing.	19
2.7	Influence of annealing time on the recovery of hydrophobicity for (a) PMMA and TPSC surfaces (annealed at 100°C), and (b) SHPMMA and SHTPSC surfaces (annealed at 150°C).	19
2.8	Chemical structures of PMMA, dimethylsiloxane (D), methyltrisiloxane (T) and tetrasiloxane (Q).	20
2.9	Deconvoluted XPS peaks of $C1s$ for; (a) fresh (b) oxidized and (c) thermally annealed PMMA surfaces. Black curves correspond to the raw XPS data.	21

2.10	Deconvoluted XPS peaks of <i>O1s</i> for; (a) fresh (b) oxidized and (c) thermally annealed PMMA surfaces. Black curves correspond to the raw XPS data.	21
2.11	Deconvoluted XPS peaks of <i>Si2p</i> for; (a) fresh (b) oxidized and (c) thermally annealed SHPMMA surfaces. Black curves correspond to the raw XPS data.	23
2.12	Deconvoluted XPS peaks of <i>C1s</i> for; (a) fresh (b) oxidized and (c) thermally annealed SHPMMA surfaces. Black curves correspond to the raw XPS data.	23
2.13	Deconvoluted XPS peaks of <i>Si2p</i> for; (a) fresh (b) oxidized and (c) thermally annealed TPSC surfaces. Black curves correspond to the raw XPS data.	24
2.14	Deconvoluted XPS peaks of <i>O1s</i> for; (a) fresh (b) oxidized and (c) thermally annealed TPSC surfaces. Black curves correspond to the raw XPS data.	25
2.15	Deconvoluted XPS peaks of <i>C1s</i> for; (a) fresh (b) oxidized and (c) thermally annealed TPSC surfaces. Black curves correspond to the raw XPS data.	25
2.16	Deconvoluted XPS peaks of <i>Si2p</i> for; (a) fresh (b) oxidized and (c) thermally annealed SHTPSC surfaces. Black curves correspond to the raw XPS data.	27
2.17	SEM images of superhydrophobic surfaces; (a) fresh SHPMMA, (b) plasma oxidized SHPMMA, and (c) thermally annealed SHPMMA, (d) fresh SHTPSC, (e) plasma oxidized SHTPSC, and (f) thermally annealed SHTPSC. All scale bars are 10 μm	29
2.18	Changes in the average values of roughness of polymer surfaces during two plasma exposure/thermal annealing cycles, determined by WLI. .	30

2.19	Fabrication of erasable hydrophilic tracks on hydrophobic TPSC surfaces. (a) PDMS mask used to obtain hydrophilic patterns shown in (b – e). All patterns were created consecutively on the same hydrophobic TPSC film. All scale bars are 6 mm	30
3.1	Microfluidic chip used in droplet guiding experiments. (a) Schematic overall diagram of the chip. (b) Illustration of the channel cross-section with big (top) and small (bottom) guided droplets. $C = 400 \mu m$, $h = 40 \mu m$, $t = 1 - 2 \mu m$ and $w = 62.4 - 70.8 \mu m$. (c) Schematic diagram of T-junction device (d) Snapshot of an actual device. T-junction for the generation of emulsion droplets is visible in the left part of the chip, the actual guiding track of sinusoidal shape fabricated in the main fluidic channel is visible in the central to right part of the chip. Scale bar is 200 μm	32
3.2	Surface profile of (a) Chip A, (b) Chip B and (c) Chip C after laser ablation.	34
3.3	Microfluidic chip geometry used in computational fluid dynamics simulations. (a) Full chip including the T-junction and droplet guiding region; (b) reduced geometry containing only the droplet guiding region.	39
3.4	(a) An overall top view of the whole computational domain including the mesh. (b) Detail of the channel expansion region (top view). (c) Side view of the channel outlet. (d) Detailed side view of the region near the track within the area denoted by orange rectangle in part (c). L-shaped mesh domain represents the edge of the guiding track. . . .	40
3.5	Schematics showing the droplet trajectory, guiding track center, perpendicular distance d , and angular analysis of droplet guiding. . . .	43

3.6	Droplet guiding as a function of the track depth. Experimental trajectories observed for water/SDS droplets in (a) Chip A with $1.0\ \mu m$ depth, (b) Chip B with $1.5\ \mu m$ depth, (c) Chip C with $2.0\ \mu m$ depth, (Experiments I, II, and III, respectively). Red, green and yellow lines represent unguided, guided and partially guided (guided or unguided) droplet trajectories, respectively, and blue lines represent boundaries of the guiding track. All scale bars are $200\ \mu m$	45
3.7	Guiding performance of surface-ablated tracks of different depths. (a-c) Distance histograms observed for Chips A, B, and C for different droplet size groups. (d-f) Angular deviation histograms observed for Chip A, Chip B, and Chip C for different droplet size groups. Mean values of the separation distances and angular deviations for different droplet size groups are indicated in figure legends. Total numbers of small/medium/big droplets studied are 10/10/10 for Chip A, 11/9/11 for Chip B and 14/16/15 for Chip C.	46
3.8	Numerical simulation of guiding of water/SDS droplets in (a) Chip A (track depth: $1\ \mu m$), and (b) Chip C (track depth: $2\ \mu m$) corresponding to Experiments I and III. All scale bars are $200\ \mu m$	47
3.9	Droplet guiding experiments performed with (a) water/SDS and (b) pure water droplets in Chip A (Experiments IV and V). Parts (c) and (d) show the simulation results for the experiments presented in parts (a) and (b), respectively. Droplet spreading in part (d) of the figure results from the low CA of pure water on the clean glass surface which is actually not achieved in the experiments (see discussion in the text.) All scale bars are $200\ \mu m$	50

3.10	Droplet guiding experiments performed with (a) pure ethylene glycol and (b) pure water droplets in Chip A (Experiments VI and VII). Parts (c) and (d) show the simulation results for the experiments presented in parts (a) and (b), respectively. All scale bars are $200 \mu m$	51
3.11	Droplet guiding experiments performed with ethylene glycol/SDS droplets. Scale bar is $200 \mu m$	52
4.1	(a) Schematic diagram of the droplet sorting device. (b) Forces acting on a droplet guided in the track.	54
4.2	Simulated profiles of a flattened droplet a) outside the guiding track ($\theta_L = 172^\circ$, $h_1 = 50 \mu m$) and b) inside the guiding track ($\theta_L = 167.5^\circ$, $h_2 = 51 \mu m$). (c) Geometry of an asymmetric flattened droplet assumed in the derivation of expressions for the droplet volume.	57
4.3	(a) Geometry of an asymmetric flattened droplet assumed in the derivation of expressions for the droplet surface area. (b) Top view of the droplet. (c) Full side view of the droplet.	60
4.4	Interpolation of area of moving droplet across the track.	62
4.5	Trapping forces on water droplet passing through the track edges in (a) Chip A ($U_d = 2357 \mu m/s$), (b) Chip B ($U_d = 985 \mu m/s$) and (c) Chip C ($U_d = 528 \mu m/s$).	63
4.6	Experimental (dashed) and simulated (solid) trajectories of water droplets at different U_d in (a) Chip A [$U_{d(1,2,3,4,5)} = (660, 1060, 1218, 1533, 2357) \mu m/s$], (b) Chip B [$U_{d(1,2,3,4,5)} = (378, 463, 490, 510, 985) \mu m/s$] and (c) Chip C [$U_{d(1,2,3,4,5)} = (234, 272, 293, 347, 528) \mu m/s$].	65

4.7	Track exit height ΔH of (a) water and (b) water/SDS droplets as a function of U_d . For each chip shown in part (a), the three solid lines indicate theoretical results carried out with $\theta_p = 172^\circ$, $\theta_t = [161^\circ (- - -), 163^\circ (—), \text{and } 165^\circ (\dots)]$. In part (b), $\theta_t = 172^\circ$ and $\theta_p = 177^\circ$.	66
4.8	Sorting of water ($U_d = 337 \mu\text{m/s}$) and water/SDS ($U_d = 609 \mu\text{m/s}$) droplets in Chip D. (a) Experimental (dashed) and simulated (solid) trajectories of water and water/SDS droplets. (b) Merged image showing trajectories followed by a water and water/SDS droplet in Chip D. Water/SDS droplet can be identified by its slightly lighter color and increased deformation due to higher velocity and lower IFT.	67
5.1	Schematic diagram of a model optofluidic dye laser based on a holey fiber of total length L filled with an aqueous dye solution circulating through the fiber. Fabry-Perot-type laser cavity is formed between the input mirror (reflectivity R_1) and the output mirror (reflectivity R_2). The optofluidic laser is pumped by an external laser source coupled to the system using a dichroic mirror. Pumping efficiency is further increased with a pump mirror (reflectivity R_3) that reflects the pump light back into the fiber while transmitting the signal light.	69
5.2	Suspended-core fiber for optofluidic dye lasers. (a) Double-cladding SCF geometry, (b) magnified view of the hole region filled with dye solution (blue color) and (c) distribution of the electric field amplitude $ E(x, y) $ of the fundamental guided mode at 560 nm. Fiber design parameters: $A^{liquid} = 8.80 \times 10^{-7} \text{cm}^2$	71

5.3	Hollow-core fiber for optofluidic dye lasers. (a) Double-cladding HCF geometry, (b) magnified view of the central hole filled with dye solution (blue color) and (c) distribution of the electric field amplitude $ E(x, y) $ of the fundamental guided mode at 560 nm. Fiber design parameters: $D_c = 4.7 \mu\text{m}$, $D_h = 1.2 \mu\text{m}$, $D_h/\Lambda = 0.9$	72
5.4	Normalized population of the upper lasing level, $N_2(z)/N$, at different N in (a) double-cladding and (b) single-cladding HCF dye lasers. . .	75
5.5	$P_p^+(z)$ (—) and $P_p^-(z)$ (- - -) at different N in (a) double-cladding and (b) single-cladding HCF dye lasers.	77
5.6	$P_s^+(z)$ (—) and $P_s^-(z)$ (- - -) at different N in (a) double-cladding and (b) single-cladding HCF dye lasers, assuming $\alpha_s = 2 \times 10^{-4} \text{ cm}^{-1}$. . .	78
5.7	$P_s^+(z)$ (—) and $P_s^-(z)$ (- - -) at different α_s in (a) double-cladding and (b) single-cladding HCF dye lasers, assuming $N = 33.3 \text{ nM}$	78
5.8	Variation of L_{opt} (- - -) and $P_{out}(L_{opt})$ (—) with N at different α_s in (a) double-cladding and (b) single-cladding HCF dye laser.	79
5.9	Variation of $P_{out}(L_{opt})$ with P_{in} at different N for $\alpha_s = 0$ (- - -) or $\alpha_s = 2 \times 10^{-4} \text{ cm}^{-1}$ (—) in (a) double-cladding and (b) single-cladding HCF dye laser.	80
5.10	Variation of P_{th} and η_{slope} with R_2 at $N = 33.3 \text{ nM}$ in (a) double-cladding and (b) single-cladding HCF dye laser.	80
5.11	Variation of P_{th} , L_{opt} and η_{slope} with N for $\alpha_s = 0$ (- - -) and $\alpha_s = 2 \times 10^{-4} \text{ cm}^{-1}$ (—) in (a) double-cladding and (b) single-cladding HCF dye laser.	81
5.12	(a) Variation of $P_{out}(L_{opt})$ with P_{in} at different N for $\alpha_s = 0$ (- - -) or $\alpha_s = 2 \times 10^{-4} \text{ cm}^{-1}$ (—) in double-cladding SCF dye laser. (b) Variation of P_{th} , L_{opt} and η_{slope} with N for $\alpha_s = 0$ (- - -) and $\alpha_s = 2 \times 10^{-4} \text{ cm}^{-1}$ (—) in double-cladding SCF dye laser.	82

5.13 Dye jet laser characteristics as a function of N for different values of ϱ . (a) T_{opt} (b) η_{slope} (left ordinate) and P_{th} (right ordinate).	84
---	----

NOMENCLATURE

AC	Alternating current
BE	Binding energy
CA	Contact angle
CAH	Contact angle hysteresis
CCD	Charge coupled device
CFD	Computational fluid dynamics
CMC	Critical micelle concentration
CMOS	Complementary metal oxide semiconductor
<i>COOH</i>	Carboxyl group
<i>CO₂</i>	Carbon dioxide
CW	Continuous wave
<i>D</i>	Dimethylsiloxane
<i>eV</i>	Electron volt
FEM	Finite element method
FESEM	Field emission scanning electron microscope
<i>HCl</i>	Hydrochloric acid
HCF	Hollow core fiber
HDK	Fumed silica H2000
IPA	Isopropyl alcohol
IFT	Interfacial tension
<i>N</i>	Nitrogen

$NaOH$	Sodium hydroxide
O	Oxygen
PAH	Polyallylamine hydrochloride
PDMS	Polydimethylsiloxane
PEEK	Poly(ether ether ketone)
pH	Potential hydrogen
PISO	Pressure implicit with splitting of operator
PMMA	Poly(methyl methacrylate)
PS	Polystyrene
PSN	Photopatternable superhydrophobic nanocomposite
PTFE	Polytetrafluoroethylene
Q	Tetrasiloxane
SCF	Suspended core fiber
SDS	Sodium dodecyl sulphate
SEM	Scanning electron microscopy
SHPMMA	Superhydrophobic PMMA
SHTPSC	Superhydrophobic TPSC
SiO_2	Silica nanoparticles
SU-8	Negative photoresist
T	Methyltrisiloxane
TiO_2	Titanium dioxide nanoparticles
TPSC	Thermoplastic polydimethylsiloxane-urea copolymer
UV	Ultra violet light
VOF	Volume of fluid
VSI	Vertical scanning interferometry
WLI	White light interferometry
XPS	X-ray photoelectron spectroscopy

ZnO	Zinc oxide
A	Area
A_p	Area of pump overlap with liquid gain medium
A_s	Area of signal overlap with liquid gain medium
α	Droplet to oil speed ratio
α_p	Scattering loss at pump wavelength
α_s	Scattering loss at signal wavelength
σ_{ap}	Absorption cross section at pump wavelength
σ_{as}	Absorption cross section at signal wavelength
σ_{ep}	Stimulated emission cross section at pump wavelength
σ_{es}	Stimulated emission cross section at signal wavelength
β	Frictional coefficient
c	Speed of light
C	Carbon
d	Center distance between droplet and track
D_h	Diameter of holes
D_L	Droplet length over left track edge
D_R	Droplet length over right track edge
E	Energy
fs	Femtosecond laser
F_D	Drag force
$F_{D,p}$	Pressure drag
$F_{D,v}$	Viscous drag
F_f	Frictional force
F_γ	Trapping force
$F_{\gamma,s}$	Trapping force due to surface energy gradient
$F_{\gamma,w}$	Trapping force due to wetting defect

h	height of microfluidic channel
ΔH	Relative track exit height of droplet
K_0, K_1	Modified Bessel functions of the second kind
L	Length of the fiber
L_c	Cavity loss
L_{opt}	Optimum length
n	Refractive index
η_{slope}	Slope efficiency
P_{out}	Output power
P_p^+	Forward propagating pump light
P_p^-	Backward propagating pump light
P_s^+	Forward propagating signal light
P_s^-	Backward propagating signal light
P_{th}	Threshold pump power
ϕ	Angular difference between droplet and track
Φ	Angle of the guiding track
R_a	Average roughness
Re	Reynolds number
R_1	Central radius of squeezed droplet outside track
R_2	Central radius of squeezed droplet inside track
R_U	Upper radius of squeezed droplet inside track
R_L	Lower radius of squeezed droplet inside track
Si	Silicon
Γ_p	Pump filling factor
Γ_s	Signal filling factor
t	Thickness of PDMS coating
τ	fluorescence lifetime

θ_t	CA over track
θ_p	CA over PDMS
μ	Viscosity of oil
U_d	Droplet speed
U_o	Oil speed
ϱ	Beam diameter ratio
w	Width of track
ω_{p0}	spot size of pump light at the beam waist
x	x-coordinate of droplet position
y	y-coordinate of droplet position
ξ	Drag coefficient
γ	Surface tension
Λ	Lattice pitch
λ	Wavelength
λ_p	Pump laser wavelength
λ_s	Signal laser wavelength

Chapter 1

INTRODUCTION

1.1 Polymer Surfaces with Switchable Wettability

Smart surfaces with wettability tunable between superhydrophobic and superhydrophilic regimes have received widespread scientific attention in the last two decades due to their potential applications in industry and basic research [Sun et al., 2013]. Apart from daily life applications such as anti-fogging, anti-reflection, cooling, corrosion resistance and self-cleaning, reconfigurable surfaces provide a simple platform for droplet manipulations, directed motility of biological cells, chemical reagent delivery, biosensing and rewritable surface microfluidics [Petroffe et al., 2015]. Furthermore, advancements with respect to ease and flexibility in microfluidic manipulation require the development of reconfigurable surfaces which can be controlled quickly and efficiently, and which can operate reliably over several cycles of wetting transitions.

Reversible switching of surface wetting properties can be achieved by various approaches such as temperature change [Shirtcliffe et al., 2005], solvent treatment [Minko et al., 2003], pH change [Sun et al., 2013], adjustment of electric potential [Krupenkin et al., 2007], light irradiation [Lim et al., 2006a] and plasma exposure [Xue et al., 2014]. Among these, light and plasma treatments are especially convenient since they are dry processes offering non-contact exposure free of contamination, and enable low temperature surface processing without altering the bulk properties of the polymers [Tsougeni et al., 2009]. In addition, they allow for selective, localized change in surface wetting properties by the use of simple masks [Herold and Rasooly, 2009]. A large

number of stimuli responsive polymeric surfaces have been developed in recent years with the major focus on simplifying the transition process, increasing the number of switching cycles and enhancing the wetting contrast between the two states [Sun et al., 2013], [Petroffe et al., 2015], [Xue et al., 2014]. It is expected that changes in wettability can be increased in both directions (hydrophobic and hydrophilic) after introducing roughness in the wetted surface by stimuli responsive nanoparticles [Lim et al., 2006a], [Jin et al., 2011].

1.1.1 Literature Review

Over the past few years, numerous studies have been reported on the fabrication of surfaces that switch their wetting behavior from superhydrophobic to superhydrophilic when triggered with ultraviolet (UV) radiation. Lim *et al.* developed silica/polyallylamine hydrochloride (SiO_2/PAH) surfaces modified with fluorinated azobenzene, which displayed switchable superhydrophobicity with erasable and rewritable patterns upon UV/visible light irradiation causing reversible photoisomerization of fluorinated azobenzene [Lim et al., 2006a]. To this end, the top most surface layer was coated with fluorinated azobenzene after silanization, which provided binding sites for photoswitchable moieties. The contact angle (CA) contrast was then investigated as a function of the number of layers deposited by layer-by-layer coating technique which introduced higher roughness to the film surface. After nine deposition cycles of SiO_2/PAH , the CA of water droplet was observed to change from 152° to 5° after 20 *min* of UV irradiation ($\lambda = 365\text{ nm}$) and back to 152° by 3 *hr* of visible irradiation ($\lambda = 440\text{ nm}$). Sun *et al.* fabricated poly(styrene-*n*-butyl acrylate-acrylic acid) films mixed with photoresponsive TiO_2 nanoparticles [Sun et al., 2013]. After UV illumination at 150 *W* for 2 hours, the CA of water droplets changed from 156° to 0° ; original superhydrophobicity was then recovered after annealing at $150^\circ C$ for 1 *hr*. In addition to UV exposure, the same film was also demonstrated to switch from superhydrophobic to superhydrophilic wetting characteristics as a function of

pH. The as-obtained film was treated with $NaOH$ solution ($pH = 12$), which caused deprotonation of covalently bonded $COOH$ group to ionic and highly hydrophilic COO^-Na^+ groups. After dipping $NaOH$ treated film in HCl solution ($pH = 2$), COO^- groups were reverted to $COOH$ groups. Petroffe *et al.* achieved fast reversible switching of CA between 118° and 18° , which was achieved by 12 *min* of UV exposure followed by annealing at $150^\circ C$ for 20 *min* [Petroffe et al., 2015]. To this end, they used photosensitive TiO_2 nanoparticles mixed in 11-(4-phenylazo)phenoxy undecanoic acid.

In spite of the simplicity of light activated switchable surfaces explored in recent years, UV induced chemical reactions that change wettability from superhydrophobic to superhydrophilic are slow even with the use of high power lamps. In contrast, oxygen plasma allows abrupt chemical modification by tuning gas phase chemistry and ion bombardment energy. Extremely short and highly reactive exposure of the target surface is of paramount importance because it ensures maximum modification of chemical structure and minimum physical or topographical change or damage. Any irreversible physical alteration in the surface topography limits the performance of the exposed surfaces in terms of absolute recovery and count of useful switching cycles even if the surface returns to its original chemical state. Tsougeni et al. performed comprehensive analysis of PMMA and poly(ether ether ketone) (PEEK) surfaces using scanning electron microscopy (SEM) and X-ray photoelectron spectroscopy (XPS) at different plasma powers and exposure times to investigate self-recovery of hydrophobicity, roughness and chemical composition under ambient conditions, which they termed as aging [Tsougeni et al., 2009]. Depending on the duration of the oxygen plasma treatment, recovery time for PEEK surfaces from superhydrophilic to superhydrophobic varied between 140 and 240 days. PMMA surfaces were only able to reach a CA value of 70° after 120 days of annealing at room temperature and never recovered to become superhydrophobic. Xue *et al.* prepared reconfigurable surfaces by spraying polystyrene/silica (PS/SiO_2) core/shell nanoparticles as a base and poly-

dimethylsiloxane (PDMS) as the hydrophobic coating [Xue et al., 2014]. After plasma treatment, obtained hydrophilic surfaces could be switched to the original hydrophobic state in 12 hours at room temperature or by heating to 150°C for 1 hour and tetrahydrofuran treatment, which is a good solvent for PS. Thermal treatment at 150°C was the most efficient recovery method, however, it could only provide three full switching cycles; in the fourth cycle, thermal annealing of the hydrophilic surface only provided the CA recovery of 40° .

Numerous methods have been reported for the preparation of superhydrophobic polymer surfaces; these include; phase separation [Han et al., 2005], physical or chemical etching [Yan et al., 2011, Erbil et al., 2003], electrospinning [Acatay et al., 2004], UV or X-ray lithography [Oner and McCarthy, 2000, Soz et al., 2015], templating [Sun et al., 2005], sol-gel processing [Shirtcliffe et al., 2003], layer-by-layer deposition [Soz et al., 2015, Shirtcliffe et al., 2003, Yilgor et al., 2012], various wet coating techniques [Soz et al., 2015, Yilgor et al., 2012, Manoudis et al., 2008, Tang et al., 2013, Tang et al., 2014] and many others [Yan et al., 2011, Roach et al., 2007, Liu and Jiang, 2012, Latthe et al., 2012, Guo et al., 2011]. Some of these processes are rather complex, some need specialized equipment and more critically, some approaches are polymer specific. It is well established that a simple method for the preparation of superhydrophobic polymer surfaces is through incorporation of various hydrophobically coated inorganic oxide nanoparticles, such as TiO_2 , SiO_2 and ZnO , at a specific concentration [Petroffe et al., 2015]. Despite this, only a limited number of reports are available in the literature on the evaluation of switchability of these surfaces from superhydrophobic to superhydrophilic and back by plasma and subsequent thermal treatment.

1.1.2 Erasable Patterning of Liquid Filaments

Light and plasma treatment can be combined with masks to obtain patterned fluidic channels for surface microfluidics and optofluidics applications. Hong *et al.*

demonstrated droplet transport along structured surfaces fabricated by a single step lithographic process using superhydrophobic photosensitive nanocomposite formula [Hong and Pan, 2010]. In particular, they used photopatternable superhydrophobic nanocomposite (PSN) which incorporates polytetrafluoroethylene (PTFE) nanoparticles into SU-8 (negative photoresist) polymer matrix. PTFE nanoparticles contributed to surface roughness required for superhydrophobicity and SU-8 provided photopatternability and adhesion to glass substrate. Hydrophilic glass surface having water CA of 10° was used as a route for liquid transport which was surrounded by superhydrophobic nanocomposite region. Xing *et al.* performed transport of aqueous droplets along hydrophilic patterns fabricated using two-step laser micromachining [Xing et al., 2011]. In the first step, they treated PDMS coating deposited on a glass substrate with a scanned CO_2 pulsed laser beam at optimized power and scanning speed and obtained extremely porous nanostructures with high water CAs. In the second step, they locally removed the previously prepared nanostructured superhydrophobic PDMS layer following the target pattern again by the same laser beam but at different operating conditions to expose underlying hydrophilic glass. Both techniques reported above are irreversible in nature; moreover, apart from generating contrast of wetting properties they also produced a topographic feature (a shallow hydrophilic channel) which provides additional liquid confinement.

1.2 Droplet Microfluidics

Digital microfluidic systems using chemical microreactors based on isolated liquid droplets represent an attractive platform for carrying out routine reactions and screening tests in clinical, biological and chemistry labs. Since micron-sized droplets have high surface-to-volume ratios, they offer reduced sample requirements and enable rapid mixing of reagents with precision and homogeneity impossible to achieve with conventional macroscopic liquid-dispensing methods, thus allowing new applications in a broad spectrum of analytical and screening assays [Hummer et al., 2016, Rak-

szewska et al., 2014]. When the droplets containing target reagents are placed within an appropriately designed microfluidic chip, a large number of independent operations can be programmed and applied sequentially to each droplet; hence, chemical reactions of interest can be performed in a highly parallelized, flexible manner at reduced reaction times [Abbyad et al., 2010b].

In order to fully exploit the potential of digital microfluidic systems, it is crucial to be able to manipulate selectively individual droplets moving in a continuous stream, as this allows controlled fusion and mixing of the droplet contents and sorting of the droplets on the basis of their chemical composition, size, or mechanical properties. In recent years, several droplet manipulation techniques have been proposed and demonstrated for droplet-based microfluidic systems. In general, these techniques can be divided into two broad classes: active manipulation methods such as optical [Pit et al., 2015], magnetic [Chetouani et al., 2006], acoustic [Franke et al., 2009], and electrokinetic [Ahn et al., 2006] that require a suitable external force to be applied to the target droplet and passive manipulation methods that rely on modifications of the droplet surface energy during its interaction with prepatterned features and structures in the microfluidic environment [Pit et al., 2015].

Active manipulation allows flexible on-demand control of droplets by an external user-controlled mechanism which can reliably and accurately target any selected droplet in the stream. An example of active droplet manipulation is the work by Fradet *et al.* where laser light was used for localized droplet heating for obtaining surface tension gradients within the droplet surface. Induced Marangoni-type flows then resulted in a "pushing" force repelling the droplet from the laser spot location. In addition, laser light could be used to merge the contents of chemically distinct droplets, thus triggering a chemical reaction of interest [Fradet et al., 2011]. Lee *et al.* controlled the motion of biological cells attached to magnetic beads inside a microfluidic channel via external magnetic field. Because of spatially-patterned microscopic magnetic fields produced by a microcoil array, biological cells were trapped and guided

actively in microfluidic channel [Lee et al., 2006]. Ahn *et al.* performed active dielectrophoretic manipulation of emulsion droplets using AC electric field created between planar microelectrodes integrated into a microfluidic chip. By turning the AC electric field on and off, they could switch the stream of flowing droplets between collect and waste channels with different hydrodynamic resistances, thus achieving droplet sorting with an effective rate of more than 1.6 kHz [Ahn et al., 2006].

Active manipulation techniques are attractive since they can be combined with the detection of the droplet contents preceding the actual manipulation step. Subsequent manipulation can then be guided by the results of this analysis, thus allowing maximal flexibility in controlling the droplet fate. However, external control and sensing mechanisms increase the complexity and limit the use of such techniques only to sophisticated systems. In contrast, passive manipulation schemes are more straightforward and offer autonomous solutions for microfluidic systems. As a downside, they are generally fixed and cannot be altered once they are implemented. Passive manipulation can be achieved by creating a gradient of surface interaction energy E between the droplet and its environment via suitable patterning of the environmental chemical and/or mechanical properties. The presence of such a gradient then results in an effective force that drives the droplet so as to minimize its interaction energy. Typically, this is associated with alternations of the droplet shape which lead to minimization of the overall droplet surface energy $E = \gamma A$, where γ is the interfacial tension and A is the area of interaction surface [Baroud, 2014].

1.2.1 Literature Review

Abbyad *et al.* achieved guiding and trapping of droplet microreactors of nanoliter volumes contained within a thin microchannel (a Hele-Shaw flow cell) by etching patterns into the top surface of the microchannel [Abbyad et al., 2010a]. Since the height of main flow channel of the cell ($35\text{ }\mu\text{m}$) was much smaller than the free-droplet diameter of $180\text{ }\mu\text{m}$, the droplets were forced into a flattened pancake-like shape with

big surface area and correspondingly high surface energy. Upon contacting a surface-etched pattern (either a hole or a channel) of depth comparable to the height of the main channel, the droplets entered partially into the hole/channel, thus decreasing their surface area and surface energy. This change of droplet surface energy upon entering the pattern then provided an effective confinement mechanism for droplet guiding and trapping [Dangla et al., 2014].

Xu *et al.* performed fusion and sorting of microdroplets using railroad-like guiding rails. In this demonstration, the droplets were moving along two parallel rails which came closer to each other at the fusion region. At this region, an additional fusion rail started, located symmetrically in the middle between the two original guiding rails. Two droplets moving along the two guiding rails and meeting simultaneously at the fusion region were merged together electrically and guided along the fusion rail toward the fusion outlet. In contrast, droplets arriving at the fusion region individually did not undergo fusion and proceeded to the waste outlets of their corresponding rails. The droplets were squeezed in a $50\ \mu\text{m}$ deep main channel and guided along a $15\ \mu\text{m}$ deep rail [Xu et al., 2012]. As compared to the previous work by Abbyad *et al.*, this configuration caused less deformation due to smaller rail depth, resulting in a smaller surface energy modification.

Yoon *et al.* performed passive sorting of droplets using variations in their sizes and/or capillary numbers [Yoon et al., 2014]. In their approach, droplets guided along a groove in a Hele-Shaw cell similar to the one used by Abbyad *et al.* encountered another parallel groove displaced laterally from the original guiding rail. The presence of this additional groove resulted in the appearance of hydrodynamic forces in both axial (along the rail) and transverse (perpendicular to the rail) directions. Depending on the droplet size and surface tension, the transverse hydrodynamic forces could eventually deform the droplet, overcome the Laplace pressure keeping the droplet in its original rail and move it to the parallel rail.

Another possibility for guiding emulsion droplets along a solid surface relies on

selective patterning of the surface wetting properties. In fact, such controlling of the motion of water droplets along surface heterogeneities is an everyday phenomenon experienced on rainy days on glass windows. This phenomenon has also found many technological applications including cleaning and coating technology. In addition, with carefully designed systems, wetting defects can be externally controlled. As an example of such active control, guiding of conductive water droplets has been demonstrated recently along electrically switchable guides fabricated on an inclined plane [Mannetje et al., 2014].

1.3 Optofluidics

Optofluidics synergistically merges technological advances in photonics and microfluidics, enabling numerous novel applications that range from the fabrication of photonic devices controlled through liquid actuation and mixing (e.g. optofluidic lenses [Fei et al., 2011] or tunable optical resonators [Levy et al., 2006]) to the development of technologies for renewable energy production and storage [Erickson et al., 2011]. A major strand of current optofluidics research is directed towards devising unconventional sources of laser light which utilize liquids as their fundamental structural element. The most prominent representatives of this class of photonic devices are bio-lasers that exploit biomolecules or living cells suspended in an aqueous buffer as their gain medium [Gather and Yun, 2011, Jonáš et al., 2014]. Enhanced interaction of light with fluorescent biological particles located either directly inside the laser cavity or in its evanescent-field region enables building of highly sensitive biochemical sensors [Fan and White, 2011, Fan and Yun, 2014]. Moreover, specific self-recognition and self-assembly of biological molecules can be used for programmable modulation and switching of lasing action [Chen et al., 2013]. Other recent applications of optofluidic lasers include the development of compact tunable sources of coherent light [Song et al., 2012, Bakal et al., 2015], temperature sensors [Lahoz et al., 2017], and flow rate sensors [Gong et al., 2015].

Typically, cavities of optofluidic lasers are integrated into specially designed microfluidic chips. The cavity itself can be based either on a miniaturized version of the standard Fabry-Perot etalon [Vezenov et al., 2005, Aubry et al., 2011] or it can employ distributed feedback mechanism [Li et al., 2006, Bakal et al., 2015]. Another strategy makes use of whispering gallery mode (WGM) resonators formed by a thin-wall capillary; here, the resonant mode resides in the capillary wall and the gain medium located inside the capillary is coupled to the mode field evanescently [Chen et al., 2013]. Alternatively, solid materials can be avoided altogether with self-assembled all-liquid WGM cavities based on spherical liquid droplets that contain the gain medium dissolved in the droplet liquid [Jonáš et al., 2014]. While all these schemes work well for miniaturized analytical and sensing applications that require only picomoles of the gain medium and operate with laser emission powers in the range of microwatts [Fan and White, 2011], they cannot be readily scaled up in order to build high-power optofluidic lasers capable of delivering watts of coherent optical power. Therefore, an alternative cavity design is needed for implementing such lasers.

Holey fibers (also known as photonic crystal fibers or microstructured fibers) represent the most recent addition to the family of fiber-based optical waveguides. Generally characterized by the presence of carefully arranged arrays of air holes in their cross-section, holey fibers can be fabricated with parameters that are impossible to achieve in standard optical fibers, such as endlessly single-mode light guiding, large mode area, high numerical aperture ($NA \approx 0.9$), and high damage threshold [Broeng et al., 1999, Russell, 2006]. Air-filled openings in holey fibers that run along the whole length of the fiber can also serve as microfluidic channels compatible with a wide range of liquids. Such a combination of light guiding and fluid confinement in a single optofluidic element [Sudirman and Margulis, 2014] has been recently exploited to achieve sensing of temperature, pressure, electric/magnetic field [Ertman et al., 2017] and refractive index [Shuai et al., 2012]. In this way, combining light and fluid in a micro-structured fiber [Sudirman and Margulis, 2014] is possible which is

recently exploited to achieve sensing of temperature, pressure, electric/magnetic field [Ertman et al., 2017] and refractive index [Shuai et al., 2012]. selectively injecting a fluorophore-containing solution into the vacant space, the fiber can be turned into an effective housing for the gain medium of an optofluidic laser that is then formed by placing the liquid-filled fiber inside an external optical cavity (see Fig. 5.1 for illustration). With a proper design, the liquid-filled fiber can retain its light-guiding properties, ensuring an optimal overlap between the gain medium and the propagating pump and signal modes over a long distance along the fiber. Thus, optofluidic lasers based on holey fibers can potentially deliver high output powers, far exceeding 1 – 5 W that is typically achieved by conventional dye jet lasers [T. F. Johnston et al., 1982] Similarly to the conventional fiber lasers, fiber geometry with large surface-to-volume ratio is advantageous for good thermal management critical in high-power applications [Richardson et al., 2010]. Specifically, in fiber lasers, both pump and signal focused beams are distributed over fiber length. Due to this reason, fiber lasers offer dramatic heat resilience in the core region which enhances its thermal capacity and overall efficiency [Richardson et al., 2010]. In a standard dye laser, pumping with a focused laser beam results in only a very small region over which population inversion can be achieved; in fact, most of the gain medium is not used. Moreover, high intensity of the focused pump beam can potentially cause damage to the windows of the dye cell [Wellegehausen et al., 1974]. These favorable properties make optofluidic fiber dye lasers an attractive alternative to conventional dye jet lasers, in which the dye solution circulates through a flow cell or propagates through open space in the form of a liquid jet stream. Because of their ability to generate monochromatic light over a broad range of visible wavelengths, tunable dye lasers have been a subject of intense research since their introduction in the early 1970s and have found numerous applications in medicine and spectroscopy [Peterson et al., 1970, T. F. Johnston et al., 1982, Duarte, 1991].

1.4 Thesis Organization

This thesis is organized as follows: In chapter 2, preparation of polymer surfaces which are able to switch their wetting properties are discussed. As an application, reconfigurable tracks to transport water in the form of filaments are demonstrated which find use in the modern field of free surface microfluidics. Chapter 3 deals with fabrication of microfluidic device for generation of microdroplets of various liquids and guiding them over optically defined tracks of different wettability. In chapter 4, droplets of two liquids with different physical and chemical properties are generated with a novel microfluidic device and those droplets are separated in their paths because of their inherent dynamic properties. In chapter 5, modeling of optofluidic fiber laser is carried out using rhodamine B dye as an aqueous gain medium in the holes of holey fibers. Conventional dye jet laser is also modeled and the performance of both the laser systems is compared.

Chapter 2

REVERSIBLE SWITCHING OF WETTING PROPERTIES FOR ERASABLE PATTERNED SURFACE MICROFLUIDICS

In this chapter, preparation of superhydrophobic Poly(methyl methacrylate) (PMMA) and thermoplastic polydimethylsiloxane-urea copolymer (TPSC) surfaces by incorporation of hydrophobic fumed silica particles into polymer layers deposited on supporting glass substrates [Soz et al., 2016] is demonstrated. Surfaces obtained in this way could be converted to superhydrophilic upon oxygen plasma exposure and back to superhydrophobic by thermal annealing for six cycles. The recovery of hydrophobicity of unmodified, smooth polymer surfaces that served as control samples is also reported. In order to correlate the change in the wetting behavior to surface chemistry and topography, all surfaces were characterized by X-ray Photoelectron Spectroscopy (XPS), Scanning Electron Microscopy (SEM) and White Light Interferometry (WLI).

In addition to modifying the wetting properties of the target surfaces, the approach is also extended to the preparation of erasable and rewritable hydrophilic channels surrounded by bulk hydrophobic areas for controlled liquid transport in surface microfluidic applications. With this simple approach, filaments of polar liquids can be guided along hydrophilic channels without any physical or structural support. The patterns of surface wettability are generated by using a thin (1 *mm*) PDMS mask with good adhesion to TPSC-coated surfaces. The mask with narrow openings is sealed over the TPSC-coated substrate, allowing plasma to react only with the exposed region. Schematic diagram illustrating this process for the production

of rewritable hydrophilic channels is shown in Fig. 2.1. Such surfaces can be used to obtain reconfigurable fluidic channels, optofluidic waveguides and droplet guiding tracks for applications in surface microfluidics [Hong and Pan, 2010, Xing et al., 2011], optofluidics [Jonas et al., 2014] and droplet microfluidics [de Ruiter et al., 2014].

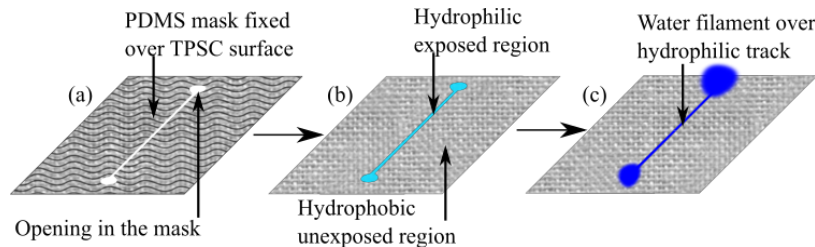


Figure 2.1: Schematic representation of the processes used for the preparation of rewritable hydrophilic channels.

2.1 Preparation of Polymeric Coatings

PMMA and TPSC solutions were prepared at a concentration of 0.5% by weight in toluene and Isopropyl alcohol (IPA) respectively by stirring overnight with a magnetic stirrer. Fumed silica, H2000 (HDK) was added to these solutions to the final polymer/silica ratio of 1/10 by weight. Subsequently, PMMA and TPSC solutions and PMMA/HDK and TPSC/HDK dispersions were spin-coated on clean glass slides ($20\text{ mm} \times 20\text{ mm} \times 0.15\text{ mm}$) at 1000 rpm for 70 sec to obtain films with an average thickness of 20 to $30\text{ }\mu\text{m}$. Samples were subsequently dried in a hood overnight and in a vacuum oven at room temperature for 24 hr .

2.2 Surface Characterization Techniques

CA measurements were performed by placing $5\text{ }\mu\text{L}$ droplets of deionized water on the film surface. Snapshots of droplets were captured and stored using a CMOS camera and a matched achromatic doublet pair placed between the sample and the camera

such that both the sample and the camera were at the foci of the two lenses forming the pair. The sample was illuminated from the direction opposite to the lens/camera location. The CA of the droplet from each recorded snapshot was measured by ImageJ software with a Drop Snake plug in [F.Stalder et al., 2010]. At least five CA measurements were made on each sample surface and their average and standard deviation were used to characterize the surfaces.

Surface images of polymer layers deposited on the substrates were obtained at each step of the process by Field Emission Scanning Electron Microscope (FESEM) operating at 2 – 10 *kV*. To minimize surface charging, all sample surfaces were sputtered by 10 *nm* of gold prior to SEM investigation. Furthermore, topographies of virgin polymer surfaces and polymer-silica composite surfaces coated with 50 *nm* gold films were examined by WLI mounted on a Surface Profiler in the vertical scanning interferometry (VSI) mode. Using WLI, it is possible to measure feature sizes from sub nanometer to millimeter range [Xu et al., 2009]. In VSI mode, average surface roughness of the samples with height discontinuities ranging between 150 *nm* to several *mm* can be precisely measured. In our studies, 10 surface maps with dimensions of 126 $\mu\text{m} \times 94 \mu\text{m}$ were obtained from different sections of the silica-coated samples to determine the values of the average surface roughness.

Chemical compositions of sample surfaces were investigated using XPS equipped with an aluminium anode at 90° electron take-off angle (between the film surface and the axis of the analyzer lens). A flood gun was employed to reduce surface charging. All C1s peaks corresponding to hydrocarbons were calibrated at a binding energy of 284.5 *eV* to correct for the energy shift caused by surface charging.

2.3 Results and Discussion

In this section, preparation and characterization of polymer-based surfaces reversibly switchable from superhydrophobic to superhydrophilic and back upon exposure to oxygen plasma followed by thermal annealing is demonstrated. In addition, the influ-

ence of the chemical structure of the polymer, surface topography and annealing time on the wetting behavior of the studied surfaces is also investigated. Four polymer surfaces considered in this study are hydrophilic PMMA, hydrophobic TPSC, superhydrophobic PMMA (SHPMMA) and superhydrophobic TPSC (SHTPSC). SEM images of surfaces of fairly smooth and featureless PMMA and rough SHPMMA covered with micron sized, agglomerated silica particles are provided in Fig. 2.2 as general examples.

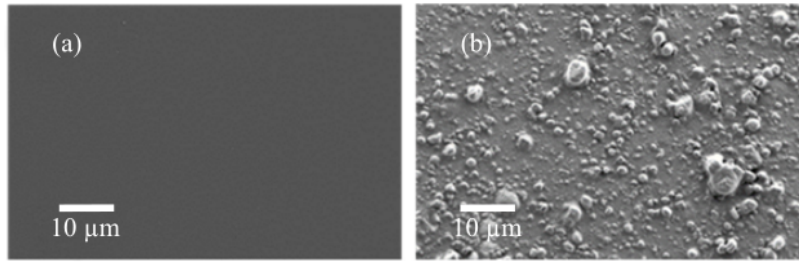


Figure 2.2: SEM images of (a) virgin PMMA and (b) superhydrophobic PMMA.

Average surface roughness (R_a), static, advancing and receding contact angles (CA) and contact angle hysteresis (CAH) values of all polymer surfaces investigated in this study are provided in Table 2.1.

Table 2.1: Values of average surface roughness (R_a), static, advancing and receding water contact angles (CA) and contact angle hysteresis (CAH) of investigated surfaces.

Sample	R_a (nm)	Static CA ($^\circ$)	Adv. CA ($^\circ$)	Rec. CA ($^\circ$)	CAH ($^\circ$)
PMMA	13.0 ± 5.2	67.5 ± 0.6	72.5 ± 1.5	52.5 ± 0.6	20
SHPMMA	250.0 ± 82	160.1 ± 0.5	162.2 ± 0.3	157.0 ± 2.8	5.2
TPSC	6.3 ± 1.0	110.3 ± 0.7	115.0 ± 1.0	93.6 ± 0.6	21.4
SHTPSC	125.0 ± 17	163.9 ± 0.6	166.7 ± 1.4	164.9 ± 1.2	1.8

As shown in Table 2.1, virgin PMMA and TPSC surfaces are extremely smooth with R_a values of 13 nm and 6.3 nm respectively. On the contrary, SHPMMA and

SHTPSC surfaces have an order of magnitude higher R_a values. Owing to their roughness, these surfaces display truly superhydrophobic behavior with average static water CAs of 160.1° and 163.9° respectively and very small CAH values of 5.2° and 1.8° respectively.

2.3.1 Oxygen Plasma Treatment and Thermal Annealing

Polymeric films were oxidized in an oxygen plasma generator operating at a base pressure of 500 *mT* and 1 *W* power for 10 *sec*. After oxidation, CA of water droplets were determined. Subsequently, the films were transferred to a constant-temperature vacuum oven to recover back their original hydrophobic state. For each full treatment cycle, virgin PMMA and TPSC samples were annealed in a 100°C oven for 20 *min*. Images of water droplets on smooth PMMA and TPSC surfaces after treatment with oxygen plasma treatment followed by thermal annealing are provided in Figs. 2.3(a) and 2.3(b) respectively. Slightly hydrophilic virgin PMMA surface, which displays a CA of $67.5^\circ \pm 0.6^\circ$ before plasma exposure, becomes highly hydrophilic and displays an average water CA of $26^\circ \pm 3^\circ$. Upon annealing, water CA increases back to the original value of $65^\circ \pm 3^\circ$. Fairly hydrophobic virgin TPSC surface with a water CA of $110.3^\circ \pm 0.7^\circ$, becomes hydrophilic upon plasma exposure and displays an average CA of $23^\circ \pm 2^\circ$. After annealing, the CA increases back to $100^\circ \pm 2^\circ$. These results clearly demonstrate reversible switching of wetting behavior of PMMA and TPSC surfaces, which can be repeated for many cycles as shown in Fig. 2.4.

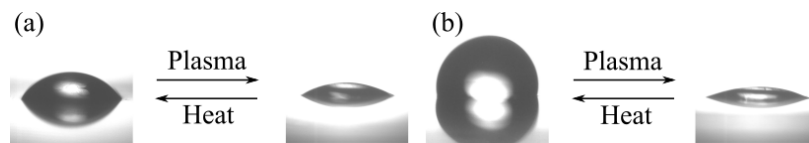


Figure 2.3: Water droplet on (a) PMMA and (b) TPSC surfaces after oxygen plasma treatment and thermal annealing.

For superhydrophobic polymeric surfaces containing HDK, the difference of water

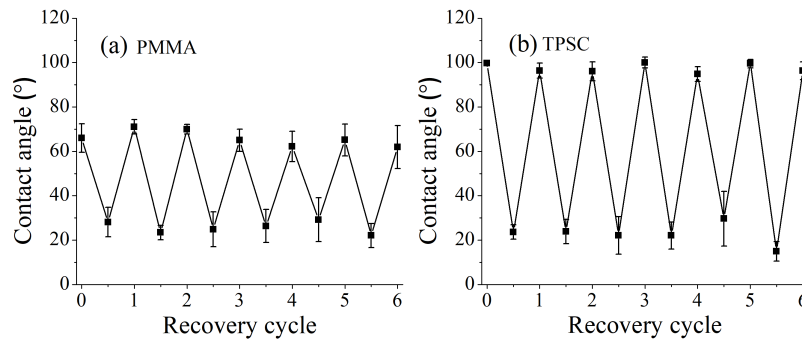


Figure 2.4: Reversible switching of wetting properties of (a) PMMA and (b) TPSC surfaces upon cyclic exposure to oxygen plasma followed by thermal annealing.

CA after plasma treatment and thermal annealing is much more dramatic. As can be seen in Figs. 2.5(a) and 2.5(b), when SHPMMA and SHTPSC surfaces are treated with oxygen plasma at 1 W for 10 sec, they both show instantaneous and complete wetting and, therefore, display truly superhydrophilic behavior. Upon annealing at 150°C for 1 hr, both surfaces recover nicely. Thermally annealed SHPMMA displays CA around 125° upon recovery, whereas, SHTPSC displays much higher CA around 140°. As shown in Fig. 2.5, the surfaces can be reversibly switched between the two extremal wetting states for at least 6 cycles without any significant degradation of their wetting characteristics.

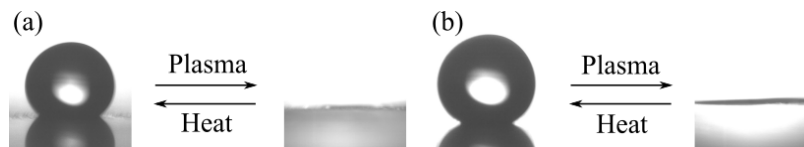


Figure 2.5: Water droplet on (a) SHPMMA and (b) SHTPSC surfaces after oxygen plasma treatment and thermal annealing.

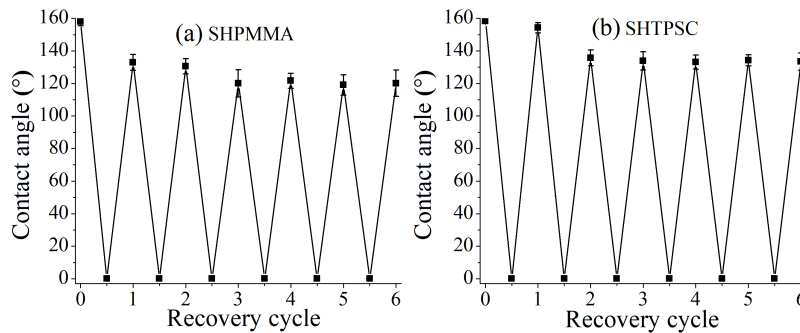


Figure 2.6: Reversible switching of wetting properties of (a) SHPMMA and (b) SHTPSC surfaces upon cyclic exposure to oxygen plasma followed by thermal annealing.

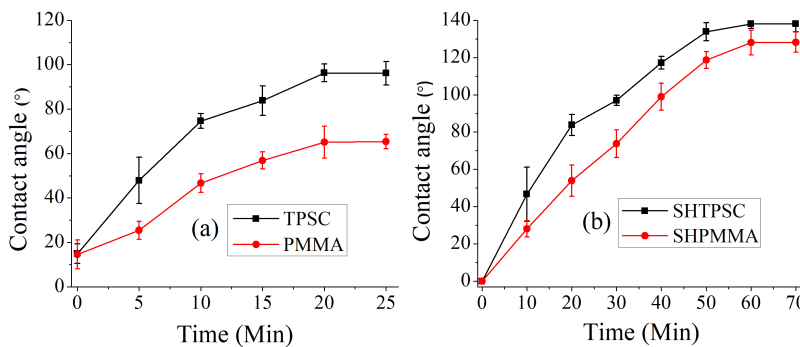


Figure 2.7: Influence of annealing time on the recovery of hydrophobicity for (a) PMMA and TPSC surfaces (annealed at 100°C), and (b) SHPMMA and SHTPSC surfaces (annealed at 150°C).

2.3.2 Annealing of Polymers with Time

Annealing temperature and time play critical roles in the recovery of hydrophobic character of the surface. After investigating various annealing temperatures, it was decided to use 100°C for PMMA and TPSC samples and 150°C for SHPMMA and SHTPSC samples. 100°C is very close to the glass transition temperature of PMMA, which is 105°C and also to the temperature where hydrogen bonding between urea linkages in TPSC starts weakening [Yilgor et al., 2000]. This allows the polymer chains to move fairly freely in the bulk and also at the surface for optimum recovery.

After deciding on the annealing temperatures, influence of annealing time on the recovery of surface hydrophobicity was systematically studied. As expected and as shown in Fig. 2.7(a), for TPSC and PMMA, CAs increased with time and reached to a plateau value after 20 *min*. On the other hand, for SHPMMA and SHTPSC, it took about 60 *min* to reach maximum CA recovery as shown in Fig. 2.7(b).

2.3.3 Characterization of Surface Chemical Composition

Chemical compositions of polymeric surfaces after exposure to oxygen plasma and subsequent thermal annealing were determined by XPS. Changes in the surface chemical compositions were correlated with the wetting behavior of the surfaces. As it is well known, XPS is a very sensitive quantitative method for studying the surface atomic compositions of polymeric materials.

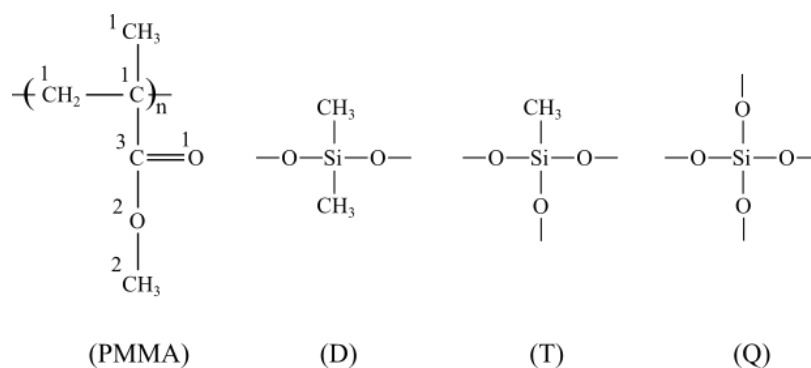


Figure 2.8: Chemical structures of PMMA, dimethylsiloxane (*D*), methyltrisiloxane (*T*) and tetrasiloxane (*Q*).

Chemical structures of PDMS which constitutes the main backbone of TPSC and that of PMMA are shown in Fig. 2.8. Also included in Fig. 2.8 are methyltrisiloxane (*T*) and tetrasiloxane (*Q*) units, which are generated by oxidation of dimethylsiloxane units (*D*). Various carbon and oxygen atoms in the PMMA unit are marked since they can be differentiated by XPS. In particular, binding energies (BEs) for 1s electrons of *C*1, *C*2 and *C*3 in PMMA are 284.5 *eV*, 286.2 *eV* and 288.5 *eV* respectively and

for $O1$ and $O2$, BEs are 531.5 eV and 533.0 eV respectively. Similarly, BEs for $2p_{3/2}$ electrons of silicon atoms in D , T and Q are 102.0 eV , 102.7 eV and 103.2 eV respectively.

XPS studies on PMMA and SHPMMA

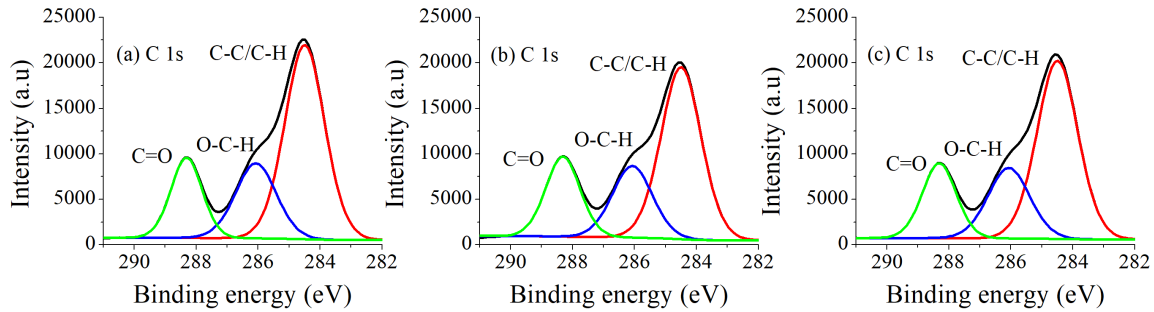


Figure 2.9: Deconvoluted XPS peaks of $C1s$ for; (a) fresh (b) oxidized and (c) thermally annealed PMMA surfaces. Black curves correspond to the raw XPS data.

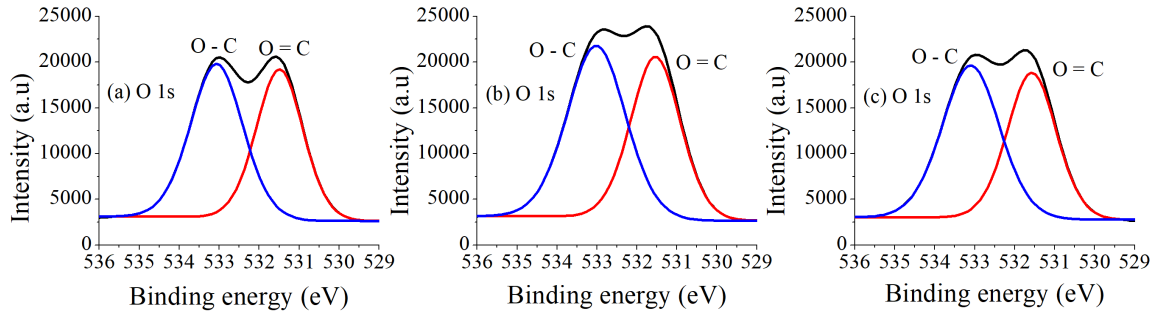


Figure 2.10: Deconvoluted XPS peaks of $O1s$ for; (a) fresh (b) oxidized and (c) thermally annealed PMMA surfaces. Black curves correspond to the raw XPS data.

Deconvoluted regions of XPS spectra corresponding to $C1s$ and $O1s$ for fresh, oxidized and thermally annealed PMMA surfaces are reproduced in Fig. 2.9 and Fig. 2.10 respectively. As expected, upon oxidation concentrations of $C2$ and $C3$ increase whereas the concentration of $C1$ decreases due to the oxidation of hydrophobic methyl

Table 2.2: Atomic percentages of $O1$, $O2$, $C1$, $C2$, and $C3$ determined from the XPS spectra of fresh, plasma oxidized and thermally annealed PMMA surfaces together with the theoretical values.

Atom	BE (eV)	Percent atomic composition			
		Thr. (%)	Fresh (%)	Oxid. (%)	Annl. (%)
O1	531.5	14.28	12.40	14.20	12.80
O2	533.0	14.28	14.19	17.39	15.46
C1	284.5	42.86	42.70	37.66	40.79
C2	286.2	14.28	16.89	15.68	16.53
C3	288.5	14.28	13.83	15.07	14.24
O/C	–	0.40	0.36	0.46	0.40
O2/C1	–	0.33	0.33	0.46	0.38

groups [Slaughter and Stevens, 2014]. Upon thermal annealing at 100°C for 20 min, this trend is reversed. This is attributed to dehydroxylation [Davydov et al., 1963] and migration of low molecular weight species to the surface [Hillborg et al., 2004]. Similar behavior is observed in the XPS spectra of $O1s$ peaks, where an increase in surface oxygen concentration upon oxidation and a decrease of this concentration upon annealing is observed. Atomic percentages obtained from the XPS spectra together with the theoretical values for PMMA are given in Table 2.2.

Bulk composition of SHPMMA films consists of 9% by weight of PMMA and 91% by weight of HDK, which is mainly SiO_2 . Therefore XPS spectra of SHPMMA surfaces display very strong $Si2p$ peaks at 103.2 eV and $Si3p_{1/2}$ peak at 103.85 eV (with the spin-orbit splitting $\Delta = 0.65$ eV), as shown in Fig. 2.11 No major change in the concentration of $Si2p$ is observed upon plasma oxidation or thermal annealing as shown in Figs. 2.11(b) and 2.11(c) and Table 2.3. This is expected, since the majority of the film consists of already fully oxidized SiO_2 agglomerates. Deconvoluted $C1s$ region of the XPS spectra for SHPMMA surfaces are reproduced in Fig. 2.12 and the

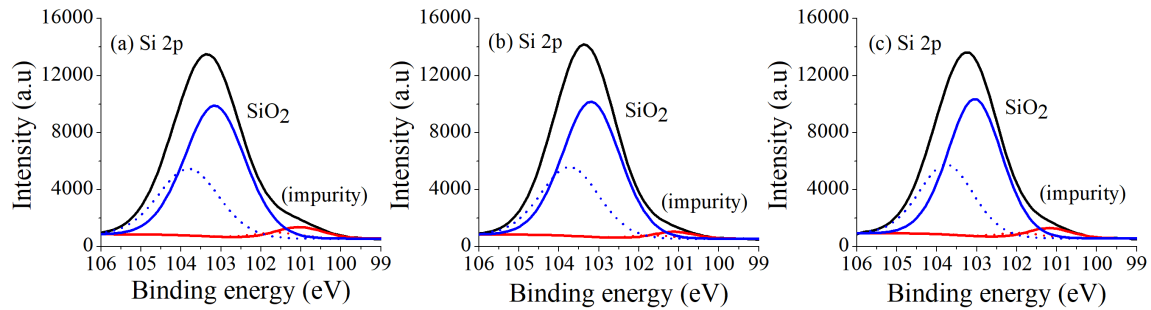


Figure 2.11: Deconvoluted XPS peaks of $Si2p$ for; (a) fresh (b) oxidized and (c) thermally annealed SHPMMA surfaces. Black curves correspond to the raw XPS data.

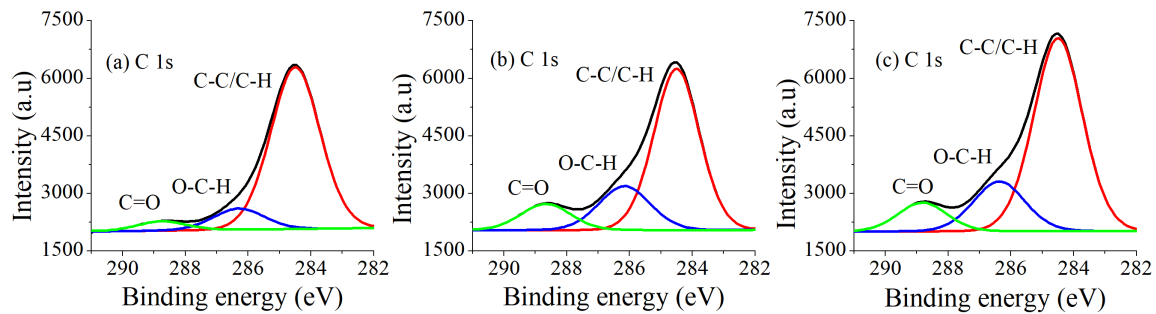


Figure 2.12: Deconvoluted XPS peaks of $C1s$ for; (a) fresh (b) oxidized and (c) thermally annealed SHPMMA surfaces. Black curves correspond to the raw XPS data.

atomic percentages calculated from these spectra are provided in Table 2.3.

Main contribution of oxygen with BE of 532.9 eV comes from SiO_2 which is 10 times higher in concentration than PMMA in nanocomposites. After plasma exposure, slight increase in oxygen from 57.29% to 58.56% (Table 2.3) is attributed to the oxidation of PMMA surface. In addition, hydrophobic silica [$Si(CH_3)_2$] also converts to hydrophilic ($Si-O_x$), which may not cause considerable increase in oxygen concentration but contributes to superhydrophilicity of the surface. Si peak from SiO_2 at a BE of 103.2 eV does not undergo any change after exposure or recovery as shown in Fig. 2.11. Carbon spectra of SHPMMA look fairly similar to those of pure PMMA,

Table 2.3: Atomic percentages of Si , O_2 , C_1 , C_2 , and C_3 determined from the XPS spectra of fresh, plasma oxidized and thermally annealed SHPMMA surfaces together with the theoretical values.

Atom	BE (eV)	Percent atomic composition			
		Thr. (%)	Fresh (%)	Oxid. (%)	Annl. (%)
Si(Q)	103.2	30.3	30.95	28.82	27.78
O ₂	532.9	60.7	57.29	58.56	56.43
C ₁	284.5	5.4	9.84	8.48	11.10
C ₂	286.2	1.8	1.35	2.62	3.02
C ₃	288.5	1.8	0.58	1.52	1.67

where C_1 , C_2 and C_3 concentrations decrease slightly upon plasma exposure and increase after thermal annealing (Table 2.3), as expected.

XPS studies on TPSC and SHTPSC

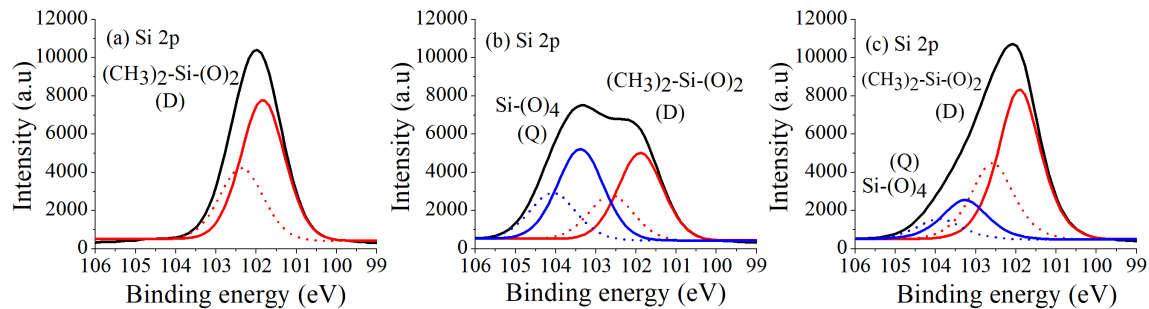


Figure 2.13: Deconvoluted XPS peaks of $Si2p$ for; (a) fresh (b) oxidized and (c) thermally annealed TPSC surfaces. Black curves correspond to the raw XPS data.

TPSC is composed of alternating PDMS and urea segments. As shown in Fig. 2.13(a), in the XPS spectrum of fresh TPSC film, $Si2p_{3/2}$ peak of dimethylsiloxane unit (D) is at BE of 102.0 eV. When the film is exposed to plasma, oxidation of D units takes place. This results in splitting of the original Si peak into two

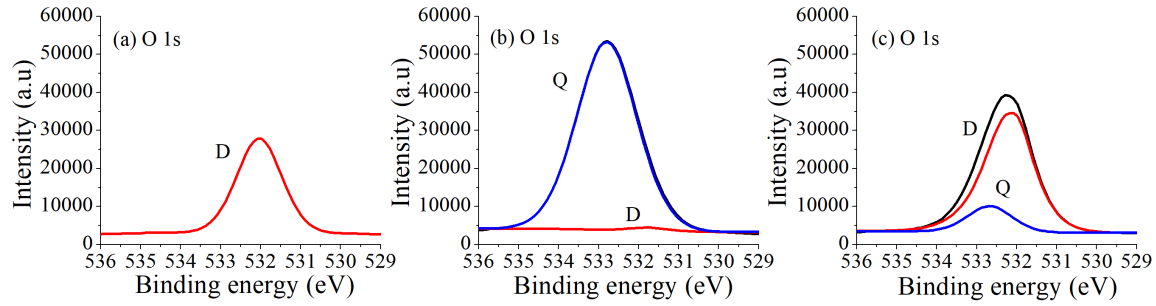


Figure 2.14: Deconvoluted XPS peaks of $O1s$ for; (a) fresh (b) oxidized and (c) thermally annealed TPSC surfaces. Black curves correspond to the raw XPS data.

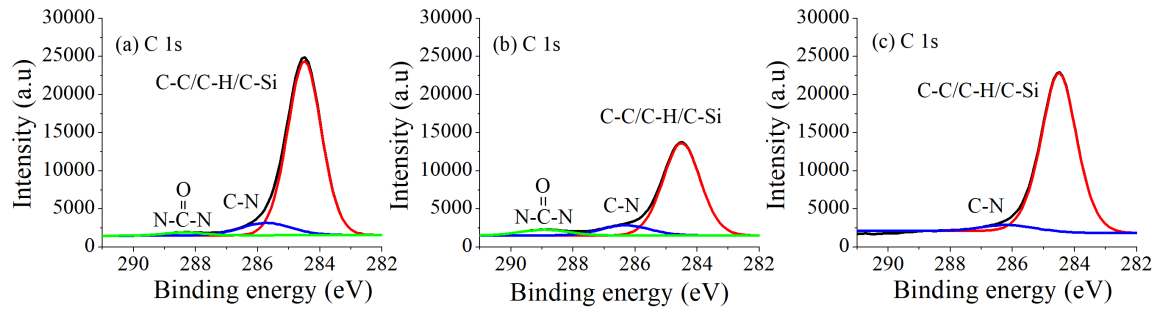


Figure 2.15: Deconvoluted XPS peaks of $C1s$ for; (a) fresh (b) oxidized and (c) thermally annealed TPSC surfaces. Black curves correspond to the raw XPS data.

peaks, representing D units and completely oxidized Q units, characterized by BE of 103.2 eV [Fig. 2.13(b)]. Interestingly, no T unit formation is observed in the XPS data. After thermal annealing, Q unit peak decreases and D unit peak increases, clearly demonstrating recovery of surface hydrophobicity [2.13(c)]. This recovery is mainly due to the migration of soft PDMS segments with a lower surface energy from the bulk TPSC film to the film-air interface, replacing the oxidized Q layer. Atomic percentages determined from XPS spectra for fresh, plasma oxidized and thermally annealed TPSC surfaces together with the theoretical values are provided in Table 2.4.

XPS spectra of oxygen (Fig. 2.14) and carbon (Fig. 2.15) display characteristic trends similar to those observed for PMMA. As shown in Fig. 2.14, a single $O1s$ peak

Table 2.4: Atomic percentages of *Si*, *O*, *C*, and *N* determined from the XPS spectra of fresh, plasma oxidized and thermally annealed TPSC surfaces together with the theoretical values.

Atom	Type	BE (eV)	Thr. (%)	Fresh (%)	Oxid. (%)	Annl. (%)
Si	D	102.0	23.00	22.88	11.66	20.77
Si	Q	103.0	–	–	12.36	5.76
O	D	532.0	23.76	22.15	0.76	26.77
O	Q	532.9	–	–	46.88	4.99
C1	CH3	284.5	49.44	47.33	22.15	14.24
C2	C-N	286.0	1.52	5.14	3.31	2.09
C3	C=O	288.8	0.76	1.07	1.87	–
N	C-N	399.5	1.52	1.43	1.01	0.89
O/C	–	–	0.46	0.41	1.74	0.78
O/C1	–	–	0.48	0.47	2.15	0.82

with BE of 532.0 eV due to *D* units is observed in the fresh sample. After plasma oxidation, this peak shifts to a BE of 532.9 eV of *Q* units. As expected, after thermal recovery, surface concentration of *D* units increases and concentration of *Q* units decreases [Fig. 2.14(c)]. Surface oxidation is further verified by a dramatic decrease in the carbon content upon plasma exposure (see Fig. 2.15). XPS spectrum of TPSC shows three carbon peaks; the most prominent one comes from the methyl groups on PDMS at BE of 284.5 eV, and a fairly small signal originates from the *C* – *N* and *C* = *O* groups present in urea at BE values of 286.0 eV and 288.8 eV, respectively. Upon oxidation, a dramatic decrease is observed in the amount of methyl carbons, which recover again upon thermal annealing. Due to low urea content in TPSC, change in urea carbons are fairly small as summarized in Table 2.4.

XPS spectra of SHTPSC silicon given in Fig. 2.16 show a dominant *Si2p3/2* peak at a BE of 103.2 eV due to the presence of a large amount of fumed silica (*SiO2*) in the film and a minor peak at BE of 101.4 eV due to PDMS backbone. Behavior

similar to PMMA is observed for $O1s$ peaks in XPS, where $O1s$ from SiO_2 at a BE of 532.9 eV is dominant (not shown). Due to very small amount of TPSC binder in the film, XPS spectrum of carbon shows only one $C1s$ peak coming from PDMS backbone at 284.5 eV (not shown). As summarized in Table 2.5, after plasma exposure atomic percentages calculated for Si and C atoms clearly show the conversion of D units to Q units. After thermal annealing, substantial recovery of D units is observed on the surface, which strongly correlates with the CA data discussed earlier.

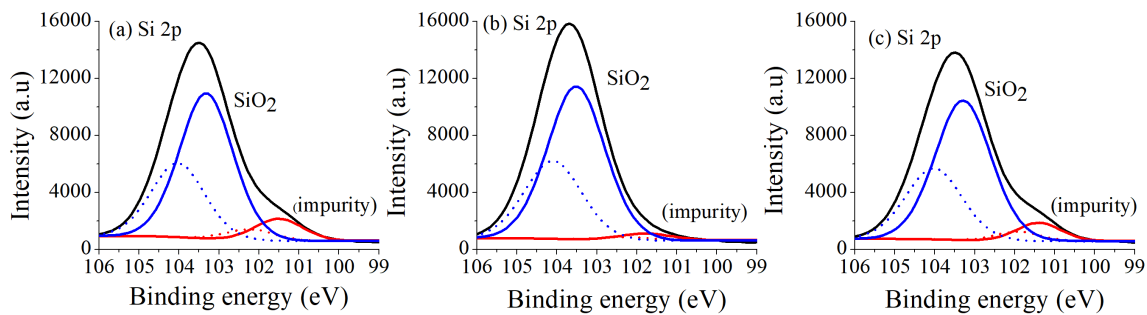


Figure 2.16: Deconvoluted XPS peaks of $Si2p$ for; (a) fresh (b) oxidized and (c) thermally annealed SHTPSC surfaces. Black curves correspond to the raw XPS data.

2.3.4 Characterization of Surface Texture and Topography

Detailed examination of surface texture and topography of all samples before and after plasma oxidation and after thermal annealing was carried out by SEM and WLI studies. Main aim of these studies was to assess if plasma oxidation and/or thermal annealing resulted in any change/damage of the surface texture, roughness or topography of the films. As shown in representative SEM images provided in Fig. 2.17, no noticeable changes were observed in the surface topography of any of the samples upon plasma oxidation and/or thermal annealing. Similar results were obtained by WLI, a non-contact optical technique, which is fairly precise in the determination of average values of surface roughness ranging from nanometer to millimeter scale. Average values of surface roughness of the samples investigated

Table 2.5: Atomic percentages of *Si*, *O*, *C*, and *N* determined from the XPS spectra of fresh, plasma oxidized and thermally annealed SHTPSC surfaces together with the theoretical values.

Atom	Type	BE (eV)	Thr. (%)	Fresh (%)	Oxid. (%)	Annl. (%)
Si	D	101.4	5.20	3.96	1.37	3.10
Si	Q	103.2	30.00	28.74	30.58	29.70
O	D	532.9	60.60	55.79	61.34	55.58
C1	CH3	284.5	11.55	11.35	4.58	11.42
C2	C-N	286.0	0.15	–	1.05	–
C3	C=O	288.8	0.08	–	0.71	–
N	N-C	–	0.15	0.15	0.37	0.20
O/C	–	–	5.14	4.91	9.67	4.87
O/C1	–	–	5.25	4.91	13.4	4.87

in the course of two exposure/recovery cycles are plotted in Fig. 2.18. As seen in this figure, average roughness values do not show any significant change after completing individual treatment steps within the two cycles. Exemplary WLI images of investigated surfaces are provided in the supporting information.

2.3.5 Rewritable Hydrophilic Channels

As a representative application of our surfaces developed with switchable wettability, we demonstrate preparation of reconfigurable hydrophilic tracks on a hydrophobic TPSC surface. These linear hydrophilic tracks shown in Fig. 2.19 were obtained by localized plasma activation of TPSC surfaces. To this end, we used a PDMS mask which defined the pattern layout consisting of a straight track (length: 15 *mm*, width: 1 *mm*) terminated by circular reservoirs (diameter: 3 *mm*) at each end. After placing the mask firmly on top of the TPSC film, the films were plasma-oxidized for 10 *sec* at 1 *W*. Subsequently, the mask was removed and 15 μ *L* of distilled water

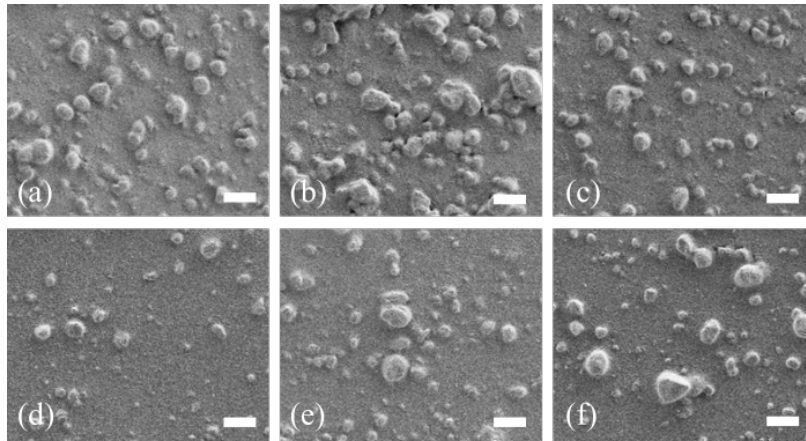


Figure 2.17: SEM images of superhydrophobic surfaces; (a) fresh SHPMMA, (b) plasma oxidized SHPMMA, and (c) thermally annealed SHPMMA, (d) fresh SHTPSC, (e) plasma oxidized SHTPSC, and (f) thermally annealed SHTPSC. All scale bars are $10\ \mu m$.

containing regular ink was placed on input reservoir. Upon deposition, water started flowing along the hydrophilic track until equilibrium was achieved in approximately $1\ min$ and water accumulated at the output reservoir. After completing the wetting experiment, the surface was dried and kept in an oven at $100^\circ C$ for $20\ min$ for thermal annealing which recovered full surface hydrophobicity and erased the pattern. Plasma oxidation through the mask was then repeated three times with the mask placed over the surface with a 45° rotation relatively to its previous orientation. As shown in Fig. 2.19, in this way, water channels were obtained over the same TPSC surface at four different angles, after consecutive plasma oxidation and thermal recovery cycles. In all four consecutive channel writing/erasing experiments, water spread along the channels with a similar speed and the confinement of aqueous filaments to the plasma-treated TPSC region was comparably good. These results clearly demonstrate the possibility of fabricating completely recoverable microfluidic channels on TPSC surfaces.

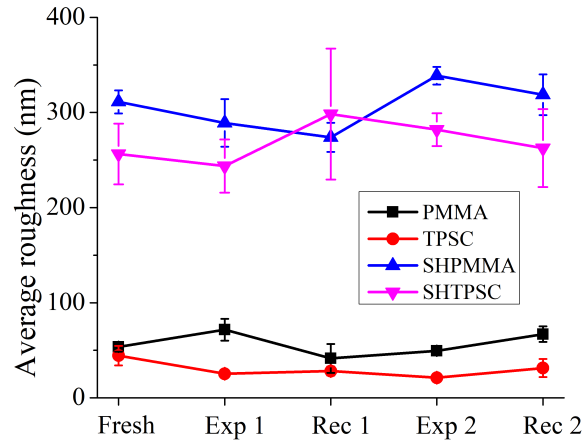


Figure 2.18: Changes in the average values of roughness of polymer surfaces during two plasma exposure/thermal annealing cycles, determined by WLI.

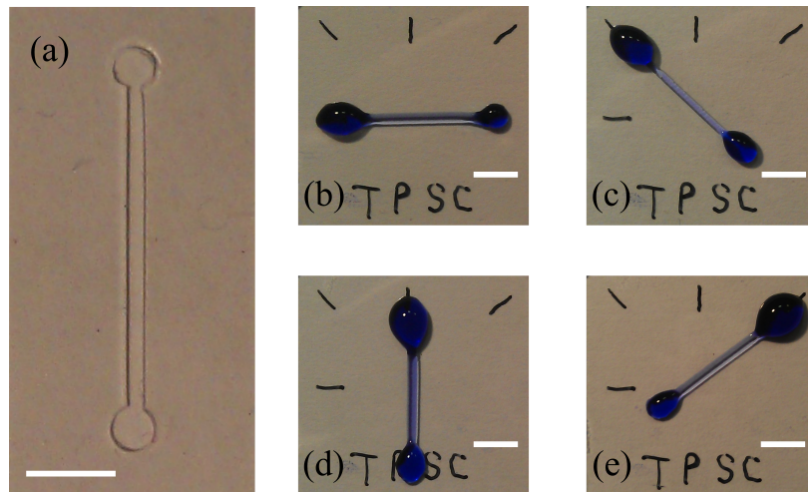


Figure 2.19: Fabrication of erasable hydrophilic tracks on hydrophobic TPSC surfaces. (a) PDMS mask used to obtain hydrophilic patterns shown in (b – e). All patterns were created consecutively on the same hydrophobic TPSC film. All scale bars are 6 mm.

Chapter 3

GUIDING OF EMULSION DROPLETS ALONG OPTICALLY PATTERNED SHALLOW TRACKS

In this chapter, passive manipulation and guiding of emulsion droplets of polar liquids suspended in an oil-based host liquid is demonstrated. The droplets are forced to move along wetting and topographic defects represented by hydrophilic tracks obtained by removing thin (thickness: $1 - 2 \mu m$) hydrophobic polydimethylsiloxane (PDMS) coatings spun on glass surfaces. Because of the shallow track depths, droplet deformation is much smaller than observed previously [Abbyad et al., 2010a, Xu et al., 2012, Yoon et al., 2014] [see Fig. 3.1(b) for illustration].

In order to obtain the droplet guiding tracks, localized ablation of PDMS layer with focused femtosecond (fs) laser pulses is used. Selective removal of PDMS layer serves two purposes: (a) it exposes hydrophilic glass surface surrounded by hydrophobic PDMS areas and (b) it generates a topographic feature (a shallow trench) which further forces the droplet to stay within its boundaries. Ablated PDMS-coated glass substrates are then plasma-bonded onto PDMS blocks containing microfluidic channels that are fabricated by standard soft lithography methods. Figs. 3.1(a) and 3.1(b) provide a schematic diagram of the droplet guiding system.

The height of the main fluidic channel, h , is $40 \mu m$ and the depth of the guiding track, t , is $1 - 2 \mu m$. Shallow depth of the guiding track used in experiments increases the relative importance of surface chemistry over surface topography in determining the outcome of the interaction between the droplet and the patterned surface. Experiments performed with two different droplet compositions (water/ethylene glycol) with and without surfactant and the smallest track depth of $1 \mu m$ show that droplet

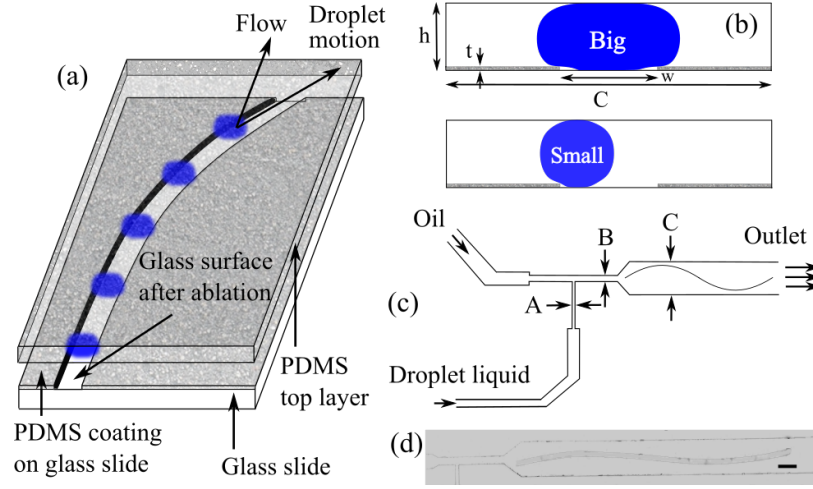


Figure 3.1: Microfluidic chip used in droplet guiding experiments. (a) Schematic overall diagram of the chip. (b) Illustration of the channel cross-section with big (top) and small (bottom) guided droplets. $C = 400 \mu\text{m}$, $h = 40 \mu\text{m}$, $t = 1 - 2 \mu\text{m}$ and $w = 62.4 - 70.8 \mu\text{m}$. (c) Schematic diagram of T-junction device (d) Snapshot of an actual device. T-junction for the generation of emulsion droplets is visible in the left part of the chip, the actual guiding track of sinusoidal shape fabricated in the main fluidic channel is visible in the central to right part of the chip. Scale bar is $200 \mu\text{m}$.

guiding is indeed caused mainly by the modification of the channel surface energy along the tracks rather than the presence of topographical steps on the surface.

3.1 Preparation of Microfluidic Chips with Droplet Guiding Tracks

Glass slides (dimensions: $76 \text{ mm} \times 26 \text{ mm} \times 1 \text{ mm}$) were initially cleaned by dipping in Hellmanex II with 2% concentration in distilled water for 70 min . Hellmanex II is an alkaline liquid detergent which is simply mixed with water to yield an effective cleaning solution for quartz and glass slides. Since the aqueous solution of Hellmanex II reduces significantly the surface tension of water, its good wetting action ensures the efficient removal of dirt particles from the glass surface. At the same time, its high emulsifying and dispersing capabilities prevent the redeposition of the loosened particles. These glass slides were then spin-coated with PDMS diluted in toluene at

different concentrations in order to obtain the desired film thickness. In particular, three PDMS-to-toluene weight mixing ratios of 1 : 4, 1 : 3, and 1 : 2 were used, producing 1 μm , 1.5 μm , and 2 μm thick layers, respectively. PDMS solution was prepared by mixing its base and curing agents at 10 : 1 weight ratio and then keeping the mixture in vacuum to remove air bubbles. After mixing the PDMS with toluene, cleaned glass slides were spin coated with the mixture at 6000 *rpm* for 2 *min*. The coated glass slides were cured in an oven at 75°C for 2 *hr*.

Droplet guiding tracks were fabricated by laser ablation of the coated glass substrates using a fs-pulsed laser beam with Gaussian beam diameter of 1 *mm*, pulse duration of 550 *fs*, wavelength of 1030 *nm*, repetition rate of 1 *kHz*, and average power of 130 *mW*. The actual beam power used for ablation could be controlled by a combination of a half-wave plate and a polarizing beam splitter. Precise two-dimensional steering of the beam across the sample necessary for creating the tracks was achieved by a pair of scanning galvo-mirrors. In order to focus the ablation beam on the sample surface, a scan lens with effective focal length of 39 *mm* was placed in the optical path. The beam was sent through the glass substrate and focused at its rear surface that was coated with PDMS. This geometry enables self-focusing of the laser beam within the glass substrate and increases selectivity in removing the PDMS coating without damaging the bulk of the substrate [Jonas et al., 2014]. Approximately 20 μm wide tracks were ablated in a single pass over the surface. By exposing the substrate to the laser beam repeatedly five times, displacing the laser focus by 10 μm after each beam pass, ablated channels with a total width of around 60 μm could be produced. The actual pattern used for droplet guiding had a sinusoidal shape with peak to peak amplitude of 300 μm and length of 7 *mm* [see Figs. 3.1(c) and 3.1(d)]. After laser ablation, surface profiles of the produced guiding tracks were determined by Dektak profilometer. Surface profilometry measurements shown in Fig. 3.2 reveal the surface profiles of the glass substrates recorded across the guiding tracks after the selective removal of PDMS coatings by laser ablation.

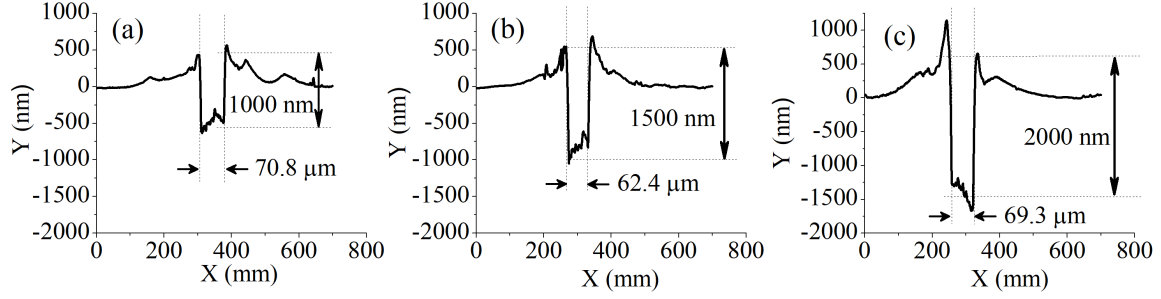


Figure 3.2: Surface profile of (a) Chip A, (b) Chip B and (c) Chip C after laser ablation.

All surface profilometry measurements show peaks at the track boundaries which correspond to the accumulation of PDMS from the central track region after the laser ablation. Height of these peaks is greater for deeper tracks because of the removal and redeposition of larger amounts of PDMS. It can be seen from the surface profilometry measurements that the ablated track region is not flat, instead, there are random bumps in the profile which indicate residual PDMS particles left behind on the glass surface.

Microfluidic devices based on PDMS elastomer were fabricated using conventional soft lithography technique [Unger et al., 2000]. Negative mold of the chip with fluidic channels of height $h = 40 \mu m$ was prepared from SU-8-50 photoresist spin-coated on a silicon wafer. T-junction geometry shown in Fig. 3.1(c) was selected for droplet generation. The widths of the channel segments *A*, *B*, and *C* were $50 \mu m$, $100 \mu m$, and $400 \mu m$, respectively. After PDMS curing at elevated temperature, the two parts were exposed to oxygen plasma after which, PDMS chips were aligned with the laser-ablated PDMS-coated microscope slides such that the sinusoidal guiding tracks were centered on the axis of channel section *C* and then immediately bonded together by firmly joining them. After bonding, microfluidic devices were kept in an oven at $120^\circ C$ for $72 hr$ in order to hasten the recovery of the hydrophobic nature of the PDMS surfaces, required for successful droplet generation [Wu et al., 2008].

An actual ablated glass slide bonded with a T-junction chip is shown in Fig. 3.1(d). The pictures of various sections of the T-junction chip were taken by a CCD camera, combined, and subsequently processed to remove background. The three chips used in this study will be referred to as Chip A, Chip B, and Chip C throughout the chapter. Wetting track depths and track widths for Chips A, B, and C are 1/1.5/2 μm and 70.8/62.4/69.3 μm , respectively.

3.2 Emulsion Systems Used in Droplet Experiments

In this work, study of surface-assisted droplet guiding with two different emulsion systems, in particular, polar droplets of (i) water and (ii) ethylene glycol with and without surfactant suspended in olive oil serving as the host liquid is presented. Droplets with added surfactant were prepared by mixing sodium dodecyl sulphate (SDS) with either deionized water or pure ethylene glycol to the final SDS concentration of 10 mM which is more than the critical micelle concentrations (CMC) of both droplet liquids [Cookey et al., 2015]. Thus, prepared droplets are called water/SDS and ethylene glycol/SDS droplets throughout the thesis. The presence of surfactant in the droplet liquid serves three purposes. Firstly, it makes droplet formation easier. Secondly, it prevents fusion or merging of neighboring droplets flowing in the stream with one another [Tullis et al., 2014]. Most importantly, upon adding surfactant, contact angle (CA) of water droplets with a glass surface immersed in olive oil increases with respect to that of pure water on glass in oil. On the other hand, CA of ethylene glycol/SDS droplets with glass immersed in oil does not increase significantly with respect to that of pure ethylene glycol at the same surfactant concentration. This allows to investigate the effect of CA and interfacial tension (IFT) on the stability of droplet guiding.

In the experiments, olive oil forming the continuous phase of the flow was injected from the top inlet of the chip [see Fig. 3.1(c)], using a syringe pump operating at a flow rate of 20 or 30 $\mu\text{L}/\text{h}$. The dispersed (droplet) phase was then injected from the lower

inlet of the chip using another syringe pump at a flow rate of $1 \mu\text{L}/h$ and emulsion droplets were generated at the T-junction [Garstecki et al., 2006]. Subsequently, the droplets entered the channel section C which contained the sinusoidal guiding track.

3.3 Computational Fluid Dynamics Study

There are various reasons for conducting numerical simulations of microfluidic experiments. Among the most important motivations are independent verification of experimental results, reduction of the number of experiments and test parameters and investigation of system configurations whose direct experimental study and evaluation is not feasible. Since the capabilities of numerical simulations have evolved considerably due to the developments in computer science and technology, the number of numerical investigations reported in the literature dealing with modeling of microfluidic devices in chemical and biological engineering applications has increased dramatically in the last few decades [Teh et al., 2008].

The choice of a particular computational method suitable for modeling a specific examined fluid dynamics problem depends heavily on the involved space and time scales that can lie anywhere between sub-atomic scale to the continuum concept. Here, the problem of interest is a two-phase flow of immiscible fluids in a microfluidic device; for modeling this class of fluid dynamics problems, the continuum concept and Lattice-Boltzmann methods are well suited [Worner, 2012]. There are many available numerical methods to model such a problem depending on the thickness of the interface between the considered fluid phases. While the arbitrary Lagrangian-Eulerian formulation [Ganesan, 2012] and level set methods [Choi and Son, 2008] assume 0 interface thickness, the Phase Field [Menech et al., 2008] and the Volume of Fluid (VOF) [Gupta et al., 2009] methods operate with a continuous interface of finite thickness. In the literature, various flow solvers have been used to tackle such kind of fluid dynamics problems: these include in-house developed source codes [Karapetsas et al., 2016], commercial softwares such as Ansys Fluent [Gupta et al.,

2009] or Comsol [Lim and Lam, 2014], and open-source codes such as OpenFoam [Malekzadeh and Roohi, 2015].

3.3.1 Solver Settings

In order to investigate the multi-phase flow of immiscible liquids, Ansys-Fluent commercial flow solver based on cell-centered finite-volume computational algorithm was used. To track the interface between the phases, Volume of Fluid (VOF) method was applied. Continuum surface stress model was selected for modeling surface tension effects. In addition, PISO (Pressure Implicit with Splitting of Operator) algorithm was used for pressure-velocity coupling where the first-order approximations were used for both spatial and temporal discretization.

3.3.2 Governing Equations

VOF method was used to track the shape and position of the interface between the immiscible dispersed and host fluids. In the VOF model, the volume fraction of each fluid in each discrete cell of a fixed mesh is computed and tracked at each time step. Volume fraction α of each phase can be calculated using the continuity equation given as:

$$\frac{\partial}{\partial t}(\alpha_l \rho_l) + \nabla(\alpha_l \rho_l \vec{u}) = 0 \quad (3.1)$$

where the subscript l indicates the phase of interest ($l = host, dispersed$), α_l is the volume fraction, ρ_l is the density, and \vec{u} is the flow velocity [Ans, 2013]. The right-hand side of Eq. (3.1) equals to 0 since the mass transfer between the phases and mass source terms are absent in our problem. The continuity equation was not directly solved for the host liquid phase, instead, the constraint was used to determine the volume fraction of the host liquid α_{host} from the calculated volume fraction of the dispersed liquid $\alpha_{dispersed}$.

$$\alpha_{host} + \alpha_{dispersed} = 1 \quad (3.2)$$

In order to calculate the velocity field, a single momentum equation was shared by both fluids. This momentum equation in vector form is given as:

$$\frac{\partial}{\partial t}(\rho \vec{u}) + \nabla \cdot (\rho \vec{u} \vec{u}) = -\nabla p + \nabla \cdot [\mu(\nabla \vec{u} + \nabla \vec{u}^T)] + \rho \vec{g} + \vec{F}. \quad (3.3)$$

Here, $\rho = \sum_l \alpha_l \rho_l$ is the density of the mixture, $\mu = \sum_l \alpha_l \mu_l$ is the dynamic viscosity of the mixture ($l = \text{host, dispersed}$), p is the pressure in the fluid, \vec{g} is the acceleration due to gravity, and \vec{F} is the density of all additional volume forces. The solution of Eq. (3.3) then gives the velocity field \vec{u} of both phases. From the definition of ρ and μ , it follows that Eq. (3.3) depends on the volume fraction of each phase through the coupled continuity equation (3.1) and constraint (3.2).

3.3.3 Computational Domain and Boundary Conditions

The geometry of chips used in the experimental part of the study consisted of a T-Junction followed by a larger channel where a single period of a sine wave-shaped track was ablated into the channel base [see Figs. 3.1(c) and 3.1(d)]. The main goal of the numerical study was to investigate droplet guiding along the ablated tracks. As the guiding can be observed starting from the beginning of the ablated pattern, only the first quarter of the pattern was included into simulations in order to reduce the computational cost. Fig. 3.3 shows a schematic of the computational domain.

Since, in the experiments, the droplets are created in a T-junction, most of the flow parameters such as the droplet velocity, droplet diameter, and distance between the droplets are dependent on each other and also on the fluid properties (in particular, fluid viscosity and surface tension). In order to control the flow parameters independently and also to reduce the computational cost, the length of the inlet channel was reduced from $1800 \mu\text{m}$ to $600 \mu\text{m}$ by excluding the first two-thirds of the channel with the T-junction from the simulation domain. Instead of the T-junction, the simulated droplets were generated by changing the inlet volume fraction of the dispersed fluid between 0 and 1 periodically. The desired distance between the neighboring droplets

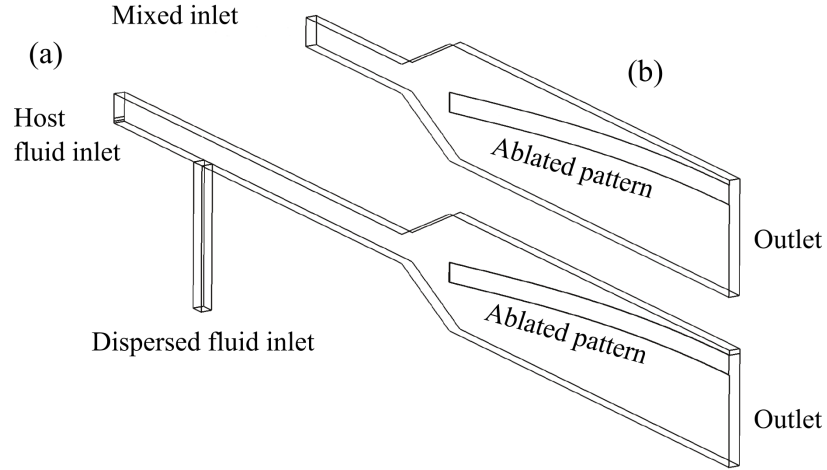


Figure 3.3: Microfluidic chip geometry used in computational fluid dynamics simulations. (a) Full chip including the T-junction and droplet guiding region; (b) reduced geometry containing only the droplet guiding region.

and the droplet size were then controlled by changing the period of the dispersed fluid feed and the duration of the dispersed fluid feed relative to the feed period, respectively.

The whole computational domain was initialized with 0 velocity magnitude, water volume fraction and effective pressure. Constant velocity and constant pressure boundary conditions were applied at the inlet and outlet channel boundaries, respectively. No-slip boundary conditions with experimentally obtained values of CAs were applied at the walls. Since the T-junction was excluded from the simulation, the inlet velocity was calculated using the total mass-flow-rate of the host and dispersed fluid. The inlet volume fraction of the dispersed fluid phase was kept at 0 for 1 *sec* before the first droplet was sent into the channel by changing the inlet volume fraction to 1.

3.3.4 Mesh Dependency

In numerical studies, the effects of the pattern depth and CA of the dispersed fluid with the pattern on the stability of droplet guiding is investigated. In order to verify

the numerical results and find the proper number and size of the cells that do not lead to computational artifacts, a mesh dependency test was conducted. To this end, simulations of droplet guiding along a $2\ \mu\text{m}$ deep track using block-structured meshes with different total numbers of cells were carried out. In order to capture the strong gradients of the flow characteristics, the cells of the mesh were finer near the channel walls, region of expansion from thin to wide channel, and around the sinusoidal guiding track. In these test simulations, it is observed that a mesh with 2.9 million cells reproduced well the observed experimental results and increasing the number of cells did not lead to further changes in the simulated droplet trajectories. Thus, 2.9 million cell mesh in all simulations reported in this study are used. The actual structure of the mesh is shown in Figs. 3.4(a – d).

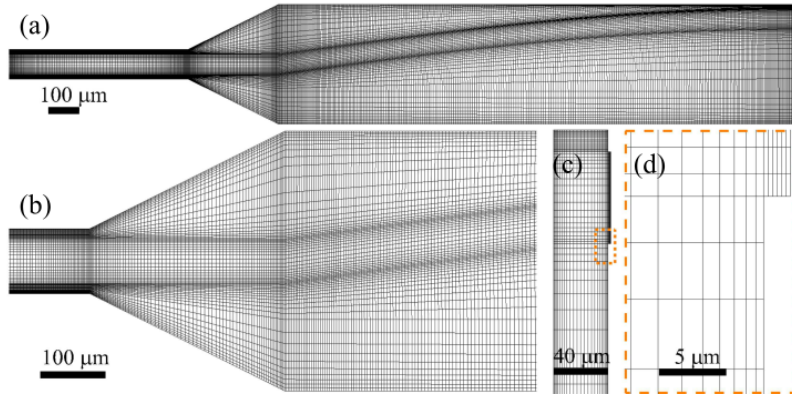


Figure 3.4: (a) An overall top view of the whole computational domain including the mesh. (b) Detail of the channel expansion region (top view). (c) Side view of the channel outlet. (d) Detailed side view of the region near the track within the area denoted by orange rectangle in part (c). L-shaped mesh domain represents the edge of the guiding track.

3.4 Results and Discussion

The results presented and discussed in this article are based on eight sets of experiments performed with different guiding chips and different droplet liquids. Table 3.1

shows a summary of material parameters and experimental conditions studied in these experiments. In particular, Experiments I-III studying the influence of the track depth on the stability of droplet guiding are introduced in Subsection 3.4.1 whereas Experiments IV-VIII dealing with the guiding of emulsion droplets formed from different polar liquids are described in Subsection 3.4.3. Normalized cross correlation-based tracking algorithm has been employed for tracking the positions of moving droplets. This algorithm has been widely used in the literature for its high efficiency and robustness in tracking moving objects of micrometer size [Sidram and Bhajantri, 2015].

3.4.1 Experiments With Different Depths of the Wetting Track

In this subsection, the results of droplet guiding experiments performed with water/SDS droplets in Chips A, B and C, corresponding to Experiments I, II, and III shown in Table 3.1, respectively are summarized. The results of numerical studies simulating guiding experiments in Chip A and Chip C (Experiments I and III in Table 3.1) are also reported.

In these experiments, water/SDS droplets of different sizes and speeds were employed. Droplet sizes and speeds ranged between $70 - 148 \mu m$ and $199 - 244 \mu m/sec$ for Chip A, $71 - 146 \mu m$ and $193 - 277 \mu m/sec$ for Chip B, and $55 - 151 \mu m$ and $215 - 288 \mu m/sec$ for Chip C, respectively. Figs. 3.6(a-c) show the trajectories obtained by image analysis for all droplets studied in the particular set of experiments with a single chip. Trajectories followed by unguided, partially guided, and completely guided droplets are shown by red, yellow and green colors, respectively, and the edges of surface-ablated tracks are indicated by blue curves. For each chip, three still images recorded during the motion of an exemplary droplet are also provided. For Chip A with the shallowest track depth of $1 \mu m$, all droplet trajectories are parallel to the walls of the fluidic channel; they follow the direction of the flow and not the ablated track. Hence, none of the droplets are guided for this case. In contrast, for Chip C with the deepest $2 \mu m$ track, all the droplets are guided. For the intermediate

Table 3.1: Parameters of microfluidic systems used in different sets of experiments.

Exp #	Droplet liquid	Track depth [μm]/Chip	Contact angle on PDMS/Glass in oil [$^\circ$]	Interfacial tension [mN/m]	Oil/droplet liquid flow rate [$\mu\text{L/h}$]	Guiding (Yes/No/Partial)
I	Water/SDS	1.0/Chip A	163.3/111.2	2.5	20/1	No
II	Water/SDS	1.5/Chip B	163.3/111.2	2.5	20/1	Partial
III	Water/SDS	2.0/Chip C	163.3/111.2	2.5	20/1	Yes
IV	Water/SDS	1.0/Chip A	163.3/111.2	2.5	20/1	No
V	Water	1.0/Chip A	171.3/47.7	16.4	30/1	Yes
VI	Ethylene glycol	1.0/Chip A	164.4/44.4	12.0	20/1	Yes
VII	Water	1.0/Chip A	171.3/47.7	16.4	20/1	Yes
VIII	Ethylene glycol/SDS	1.0/Chip A	160.8/51.8	—	20/1	Yes

track depth of $1.5 \mu\text{m}$ fabricated in Chip B, partial droplet guiding (15 guided out of 31 studied droplets) is observed.

In order to compare quantitatively the stability of guiding for droplets of different sizes, a convention was adopted such that the droplets were divided into three size categories labeled small, medium, and big. For each studied chip, the classification was done so as to yield similar number of droplets in each size category. In particular, small, medium, and big refer to droplet sizes smaller than $90 \mu\text{m}$ (Chip A) / $87 \mu\text{m}$ (Chip B) / $85 \mu\text{m}$ (Chip C), between $90 - 110 \mu\text{m}$ (Chip A) / $87 - 98 \mu\text{m}$ (Chip B) / $85 - 103 \mu\text{m}$ (Chip C), and larger than $110 \mu\text{m}$ (Chip A) / $98 \mu\text{m}$ (Chip B) / $103 \mu\text{m}$ (Chip C), respectively.

Guiding performance of individual chips was then characterized by evaluating the perpendicular distance between the track center and the droplet trajectory and the

angular deviation between the track axis and the droplet trajectory for each video frame acquired along the route of the tracked droplet. This was done by comparing each droplet path coordinate with the center of the guiding track in terms of distance 'd' and angle ' ϕ ' as shown in Fig. 3.5.

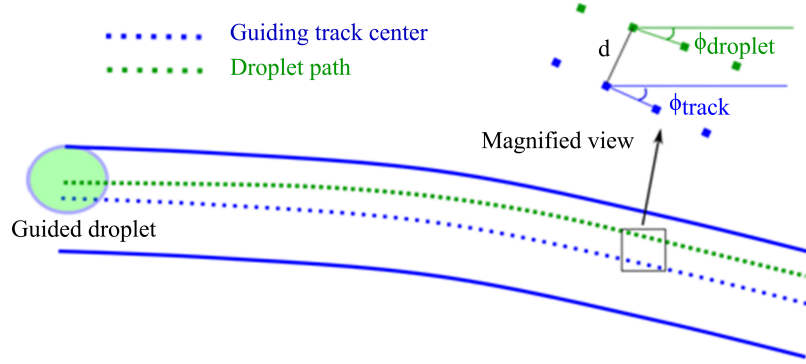


Figure 3.5: Schematics showing the droplet trajectory, guiding track center, perpendicular distance d , and angular analysis of droplet guiding.

Coordinates of the i^{th} point along the droplet trajectory and j^{th} point along the ablated track center are represented by $(r_{i,x}, r_{i,y})$ and $(s_{j,x}, s_{j,y})$, respectively. Here, subscripts x and y refer to the horizontal and vertical directions in a two dimensional image, respectively. For each position $(r_{i,x}, r_{i,y})$ along the droplet trajectory, the corresponding position $(s_{\bar{j},x}, s_{\bar{j},y})$ on the track center was found that minimizes the perpendicular distance d_i between the droplet trajectory and the track center. \bar{j} indicates the index number along the ablated track center minimizing the distance with the i^{th} point along the droplet trajectory. The value of d_i is then given by:

$$d_i = \sqrt{(r_{i,x} - s_{\bar{j},x})^2 + (r_{i,y} - s_{\bar{j},y})^2} \quad (3.4)$$

Local directions of the droplet trajectory at point $(r_{i,x}, r_{i,y})$ and of the center of the ablated track at point $(s_{\bar{j},x}, s_{\bar{j},y})$ with respect to the channel side walls are characterized by angles $\phi_{droplet,i}$, $\phi_{track,\bar{j}}$ defined as:

$$\phi_{droplet,i} = \tan^{-1} \left[\frac{r_{(i+1),y} - r_{i,y}}{r_{(i+1),x} - r_{i,x}} \right], \quad (3.5a)$$

$$\phi_{track,\bar{j}} = \tan^{-1} \left[\frac{s_{(\bar{j}+1),y} - s_{\bar{j},y}}{s_{(\bar{j}+1),x} - s_{\bar{j},x}} \right], \quad (3.5b)$$

Angular deviation between the droplet trajectory and the track center at a given pixel is then obtained as:

$$\Delta\phi_i = |\phi_{droplet,i} - \phi_{track,\bar{j}}|. \quad (3.6)$$

The same analysis is done for all the droplets and the results are combined to evaluate the overall quality of guiding for the studied system. The values of d_i and $\Delta\phi_i$ obtained for all trajectory points of all droplets within individual chips have been combined and are shown as histograms in Fig. 3.7. The distance histograms reveal the confinement of the droplets within the track while the angle histograms reveal their guiding. The results obtained for Chip A (track depth: $1 \mu m$), plotted in Figs. 3.7(a) and 3.7(d), clearly show that droplets of all sizes are neither confined in the track nor following the track direction. All distance histograms of Fig. 3.7(a) are virtually flat, indicating no fixed separation between the track axis and the droplet center. In addition, the angle histograms of Fig. 3.7(d) are also quite broad, reflecting a wide range of angles between the droplet trajectory and the track axis that is parallel to the sinusoidal contour of the track. This stems from the fact that the droplets are moving predominantly in the direction of the flow, ignoring the presence of the ablated track. Overall, the data shows no guiding for Chip A, which results from insufficient depth of the ablated track. The histograms plotted in Figs. 3.7(b) and 3.7(e) correspond to Chip B (track depth: $1.5 \mu m$). In this case, due to the interplay between the flow direction and position of the topographical step, guided droplets tend to stay away from the center of the guiding track and follow its downstream edge. Therefore, all the distance histograms of Fig. 3.7(b) peak at non-zero positive values of d . However, the average separation distance \bar{d} between the track axis and the droplet center visibly decreases with increasing droplet size. Since Chip B only enables partial droplet guiding, the effect of droplet size is not too pronounced because the droplets are confined only loosely within the track. Despite this, the angle histograms of Fig. 3.7

(e) are shifted to significantly smaller values relative to the data obtained with Chip A [compare with Fig. 3.7(d)], thus showing better guiding caused by a deeper track.

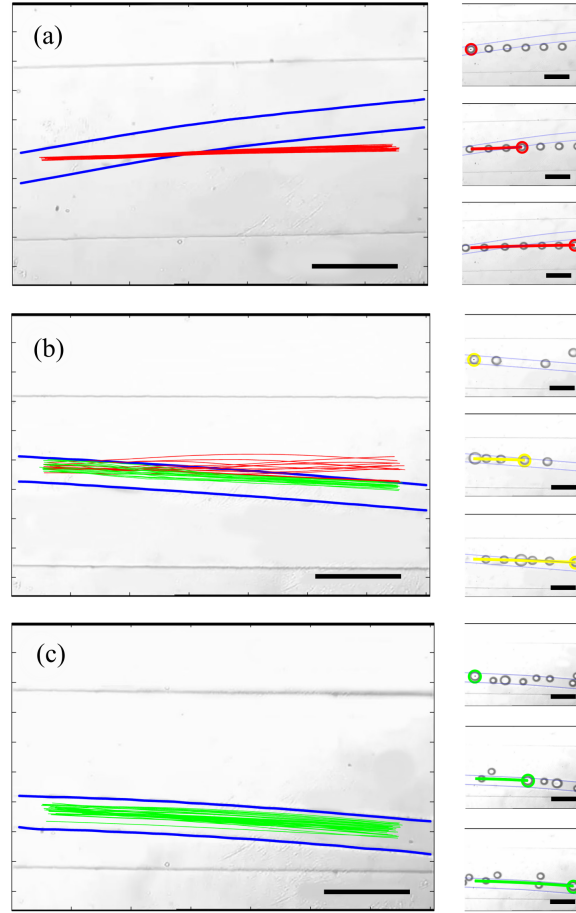


Figure 3.6: Droplet guiding as a function of the track depth. Experimental trajectories observed for water/SDS droplets in (a) Chip A with $1.0 \mu m$ depth, (b) Chip B with $1.5 \mu m$ depth, (c) Chip C with $2.0 \mu m$ depth, (Experiments I, II, and III, respectively). Red, green and yellow lines represent unguided, guided and partially guided (guided or unguided) droplet trajectories, respectively, and blue lines represent boundaries of the guiding track. All scale bars are $200 \mu m$.

Finally, the histograms plotted in Figs. 3.7(c) and 3.7(f) correspond to Chip C (track depth: $2 \mu m$). Similarly to the previous case of Chip B, small droplets tend to stay near the track edge so that the peak of their distance histogram shown in Fig. 3.7(c) (black bars) is located at a relatively large value of d . However, with

increasing droplet size, the peaks of the distance histograms shift strongly toward the 0 value of d . Because the droplet confinement is almost complete for this case, the effect of droplet size is much more pronounced than for Chip B. As seen in the angular deviation histograms of Fig. 3.7(f), Chip C enables almost perfect guiding of droplets of all sizes. Thus, the peaks of the angular deviation histograms have all shifted towards the zero value of $\overline{\Delta\phi}$.

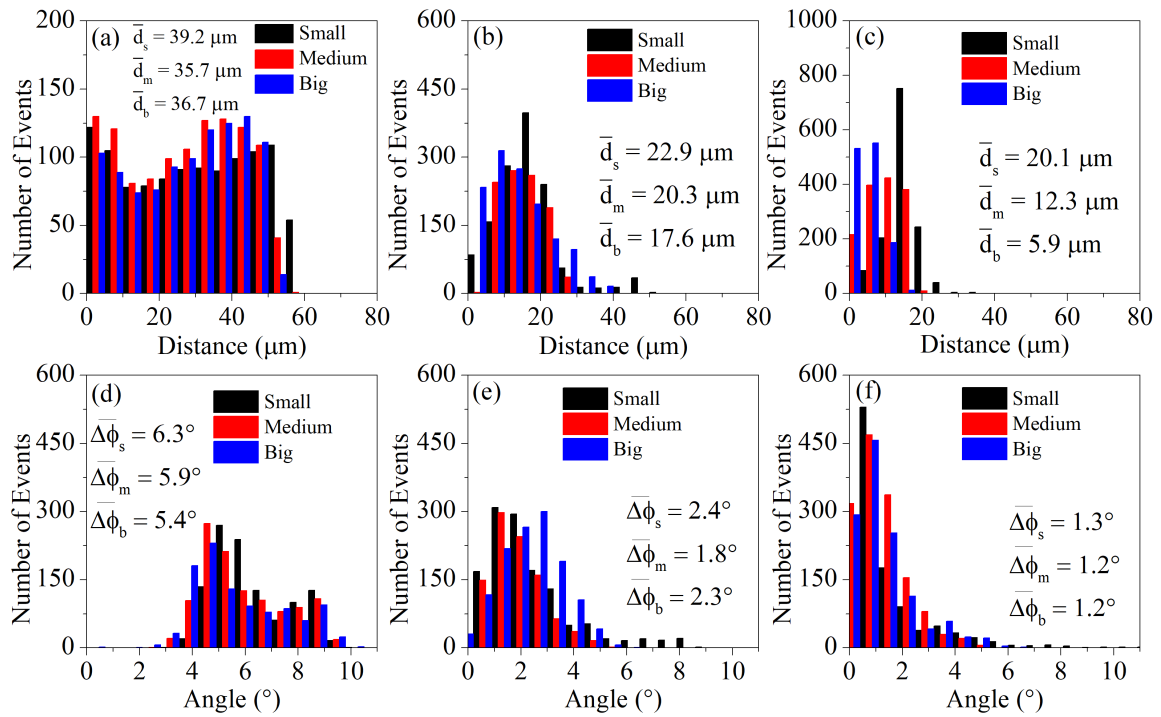


Figure 3.7: Guiding performance of surface-ablated tracks of different depths. (a-c) Distance histograms observed for Chips A, B, and C for different droplet size groups. (d-f) Angular deviation histograms observed for Chip A, Chip B, and Chip C for different droplet size groups. Mean values of the separation distances and angular deviations for different droplet size groups are indicated in figure legends. Total numbers of small/medium/big droplets studied are 10/10/10 for Chip A, 11/9/11 for Chip B and 14/16/15 for Chip C.

3.4.2 Numerical Results of Droplet Guiding

In order to gain more insight into the mechanisms of droplet guiding, the effect of ablated region depth has been investigated numerically. In this CFD study, the depth of the sinusoidal guiding pattern was chosen to be either $1\ \mu\text{m}$ or $2\ \mu\text{m}$, corresponding to the two extreme experimental cases of Chip A and Chip C (Experiments I and III in Table 3.1). It is assumed that the guiding track was formed by a clean glass surface whereas the region surrounding the track was formed by PDMS surface. Both surfaces were characterized by their static CAs which were determined experimentally for droplets of water/SDS mixture immersed in olive oil. In addition, dynamic behavior of immiscible fluids in the two-phase flow was described by their IFT which was measured for an interface between water/SDS and olive oil by the Wilhelmy plate method [Aas et al., 2013]. Measured IFT and CAs are summarized in Table 3.1; these values were applied in the simulations in order to make them as realistic as possible. In all numerical results presented in the article, droplet colors indicate different fluids where red, green, and blue colors are used for water/SDS, pure water, and pure ethylene glycol, respectively.

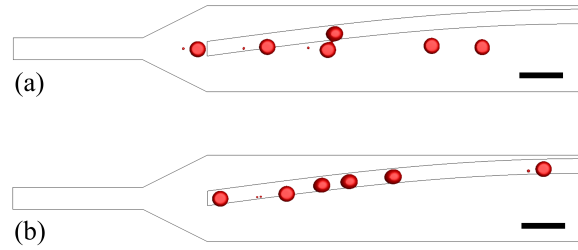


Figure 3.8: Numerical simulation of guiding of water/SDS droplets in (a) Chip A (track depth: $1\ \mu\text{m}$), and (b) Chip C (track depth: $2\ \mu\text{m}$) corresponding to Experiments I and III. All scale bars are $200\ \mu\text{m}$.

The simulations of droplet guiding yielded video files showing water/SDS droplets flowing in oil towards the channel outlet. The last frames of the simulated videos produced for $1\ \mu\text{m}$ and $2\ \mu\text{m}$ deep tracks, with 6 droplets present simultaneously in

the channel, are shown in Fig. 3.8 (a) and 3.8 (b), respectively. It is evident that majority of the droplets are not guided for the shallow track [Fig. 3.8 (a)] whereas all the droplets moving along the deep track are guided [Fig. 3.8 (b)].

3.4.3 Experiments With Other Droplet Liquids

In this subsection, the results of Experiments IV - VIII described in Table 3.1, obtained using Chip A and two different droplet liquids with different wetting properties on the glass surface immersed in oil are presented. In particular, the studied liquids include water and ethylene glycol, both used either with or without surfactant. In addition, the results of numerical studies performed for parameters corresponding to Experiments IV - VII are also presented here. All the parameters relevant to experimental and numerical studies IV–VIII are summarized in Table 3.1.

CAs measured for all studied droplet liquids on PDMS and glass surfaces immersed in olive oil are shown in Table 3.1. On the PDMS surface, CAs for pure water and pure ethylene glycol were found to be 171.3° and 164.4° , respectively. These values are similar to the CAs measured on PDMS for water/SDS droplets (163.3°) and ethylene glycol/SDS droplets (160.8°). The difference between CAs of individual liquids becomes much more prominent when the surface is changed to glass. On the glass surface, CA were measured to be 47.7° , 44.4° , 111.2° and 51.8° for pure water, pure ethylene glycol, water/SDS and ethylene glycol/SDS droplets, respectively. Consequently, the contrast between the CAs measured on PDMS and on glass is much smaller for water/SDS droplets, in comparison to water, ethylene glycol and ethylene glycol/SDS droplets.

Experimental and simulated trajectories determined for water/SDS and pure water droplets in Chip A (Exps. IV and V) are shown in Fig. 3.9. In order to obtain similar droplet sizes in both experiments, oil flow rate of $30 \mu\text{L}/h$ was used in Exp. V with pure water droplets whereas in Exp. IV with water/SDS droplets, oil flow rate was kept at $20 \mu\text{L}/h$. This difference in the applied flow rates is due to almost 7-fold

difference in IFT for both cases. Consequently, the droplet speed in Exp. V is considerably higher than the droplet speed in Exp. IV because the size and speed of moving droplets are interrelated [Garstecki et al., 2006]. In particular, for the data presented in Fig. 3.9(a), droplet size and speed ranged from $72 - 82 \mu\text{m}$ and $267 - 280 \mu\text{m/sec}$, respectively. In contrast, for the data presented in Fig. 3.9(b), droplet size and speed ranged from $75 - 89 \mu\text{m}$ and $394 - 440 \mu\text{m/sec}$, respectively. Despite the higher droplet speeds, all droplets are observed to be guided in Exp. V (water) while in Exp. IV (water/SDS), no single droplet is guided.

From the comparison of Exp. IV (water/SDS) and V (water), it is concluded that the main mechanism enabling droplet guiding is the modification of interfacial energy between the droplet surface and the surface of the guiding track rather than the topography of the track. In other words, due to a higher contrast of CAs between the PDMS and glass surfaces for pure water droplets as compared to water/SDS droplets (see Table 3.1), pure water droplets are much more strongly attracted to the laser ablated track. These experimental results have also been verified by numerical simulations whose outcome is shown in Figs. 3.9(c) and 3.9(d). In the simulations, material constants provided in Table 3.1 for Exp. IV and V were used. In agreement with the experimental results shown in Figs. 3.9(a) and 3.9(b), no droplets are observed to be guided in Fig. 3.9(c) while all droplets are strongly guided in Fig. 3.9(d). In Fig. 3.9(d), the simulated droplets are observed to be strongly deformed and flattened as they are guided along the track; this behavior was not observed in the experiments presented in Fig. 3.9(b). This difference in the droplet behavior can be attributed to incomplete removal of PDMS from the laser-ablated tracks. In the experiments, some residues of PDMS are left on the glass surface after laser ablation. This is indicated by the roughness observed in the surface profiles of the ablated tracks shown in Fig. 3.2. Residual PDMS remaining on the track surface then renders this surface less hydrophilic which results in a higher CA of pure water on this surface and, consequently, lower wetting of the surface by the droplets of pure water. Thus, the size

of the contact area between the droplet and the track decreases, resulting in more spherical droplets observed in the experiments, in contrast to the simulated droplet shape.

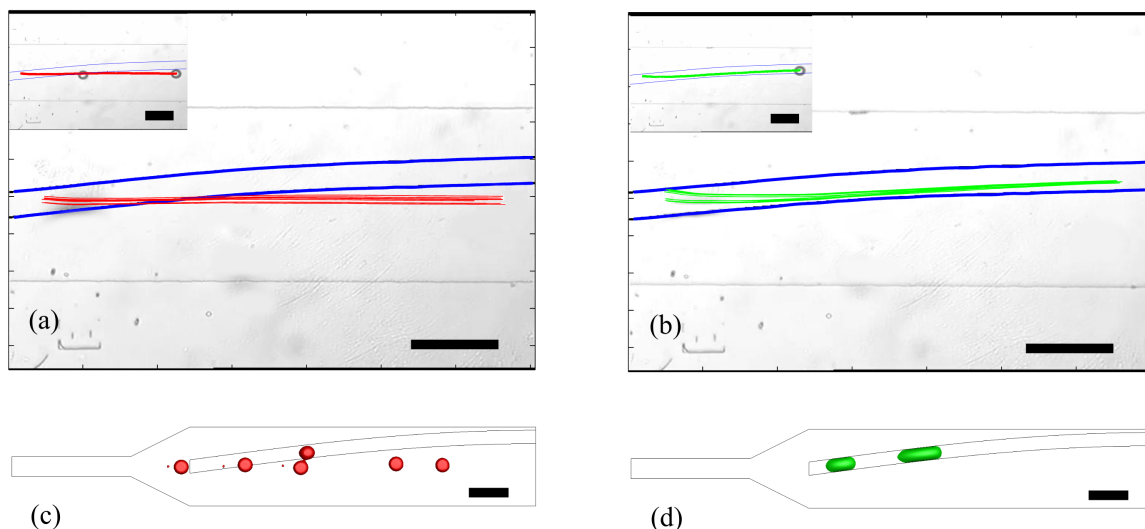


Figure 3.9: Droplet guiding experiments performed with (a) water/SDS and (b) pure water droplets in Chip A (Experiments IV and V). Parts (c) and (d) show the simulation results for the experiments presented in parts (a) and (b), respectively. Droplet spreading in part (d) of the figure results from the low CA of pure water on the clean glass surface which is actually not achieved in the experiments (see discussion in the text.) All scale bars are $200\ \mu\text{m}$.

Experimental and simulated trajectories observed in Chip A for pure ethylene glycol and pure water droplets are shown in Fig. 3.10 (Exps. VI and VII). Pure water and pure ethylene glycol have different polarity and IFT in olive oil but they display similar CAs on glass and PDMS when immersed in the oil. Similarity of the results obtained for pure water and pure ethylene glycol then shows that the main guiding mechanism taking place is due to the increased wettability - or reduced CA - in the central ablated region. The flow rates of oil and droplet liquid in both cases were kept at $20\ \mu\text{L}/\text{h}$ and $1\ \mu\text{L}/\text{h}$, respectively, yielding similar droplet sizes. In particular, droplet size and speed ranged between $96 - 106\ \mu\text{m}$ ($100 - 117\ \mu\text{m}$) and $203 - 245\ \mu\text{m}/\text{sec}$ ($267 - 286\ \mu\text{m}/\text{sec}$) in Figs. 3.10(a) [Fig. 3.10(b)], respectively.

For both ethylene glycol and water droplets, complete guiding is observed in Figs. 3.10(a) and 3.10(b). These results have also been verified by the numerical simulations shown in Figs. 3.10(c) and 3.10(d). Similarly to the simulation result of Fig. 3.9(d), simulated droplets in Figs. 3.10(c) and 3.10(d) are observed to be deformed due to strong wetting of the guiding tracks. Such deformations were not observed in the experiments because of the residual PDMS left on the guiding track surface after the laser ablation, resulting in decreased wettability of the track surface with polar droplet liquids.

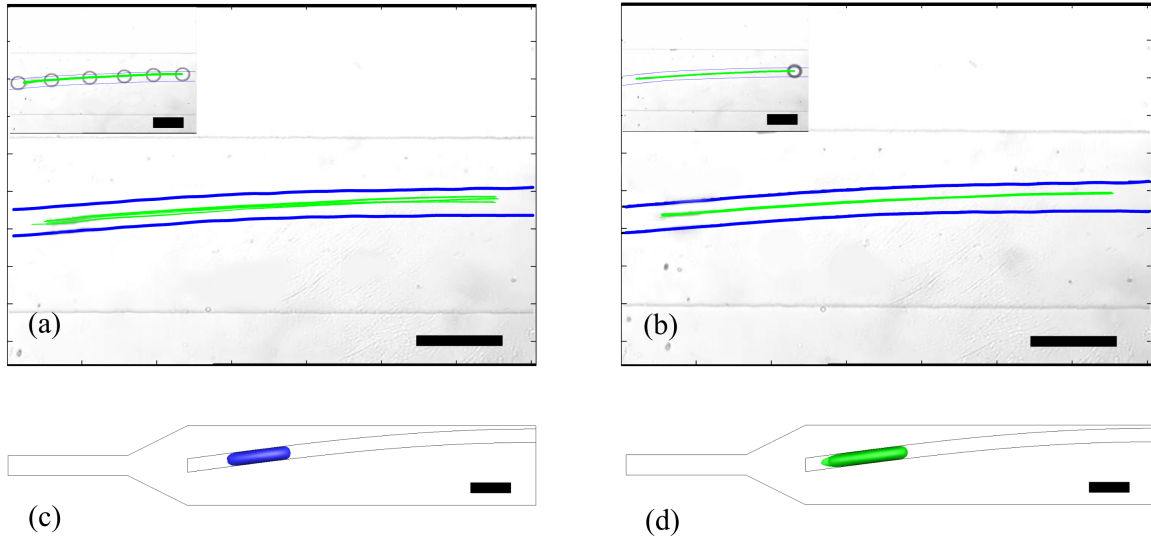


Figure 3.10: Droplet guiding experiments performed with (a) pure ethylene glycol and (b) pure water droplets in Chip A (Experiments VI and VII). Parts (c) and (d) show the simulation results for the experiments presented in parts (a) and (b), respectively. All scale bars are $200\ \mu\text{m}$.

Finally, experiments with ethylene glycol/SDS droplets were carried out in chip A (Exp. VIII). In these experiments, flow rates of oil and water were kept at $20\ \mu\text{L}/\text{h}$ and $1\ \mu\text{L}/\text{h}$, respectively. Resulting size of the droplets then varied from $96\ \mu\text{m}$ to $103\ \mu\text{m}$ and the speed of the droplets varied from $228\ \mu\text{m}/\text{sec}$ to $265\ \mu\text{m}/\text{sec}$. Experimental trajectories of the droplets are shown in Fig. 3.11. The CA of ethylene glycol/SDS droplets on a glass surface immersed in olive oil was measured to be 51.8° ,

very similar to the cases of pure water and pure ethylene glycol droplets surrounded by oil. Consequently, due to the relatively good wetting of the glass surface, ethylene glycol/SDS droplets display complete guiding, just like the droplets of pure water and pure ethylene glycol. This finding is in strong contrast with the results obtained for water/SDS droplets under similar operating conditions (droplet size and speed) as shown in Fig. 3.9(a) where no guiding is observed for water/SDS droplets. Comparison of the results obtained for both water and ethylene glycol droplets without and with the surfactant suggests that the organization of the surfactant layer at the droplet surface represents a major factor determining the stability of droplet guiding. Specifically, while the addition of the surfactant causes a dramatic change in the guiding behavior of water droplets, no such change is observed for ethylene glycol droplets upon adding the surfactant. These results also indicate that the polarity of the bulk droplet liquid plays only a marginal role in the guiding, which is almost completely controlled by the droplet interfacial energy given by the complex physico-chemical interactions between the droplet liquid, the surfactant layer, and the host medium.

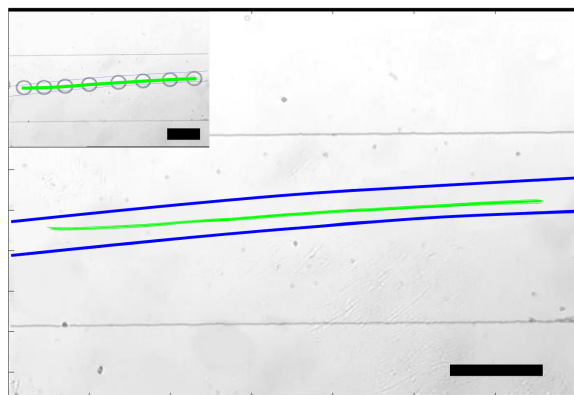


Figure 3.11: Droplet guiding experiments performed with ethylene glycol/SDS droplets. Scale bar is 200 μm .

Chapter 4

PASSIVE SORTING OF EMULSION DROPLETS

The advancement in the field of digital microfluidics demands elegant and meticulous control over motion of droplets and/or enclosed species to store them at the correct location, for instance, towards the starting position of another protocol or a position where they can be analyzed or held for incubation. Sorting or separating such species in a populated stream at rapid speed with high success rate is of paramount importance in microfluidics for parallelization, diagnostics, isolated chemical reactions and high throughput screening [Abate et al., 2010]. This kind of directed manipulation requires high degree of control over individual droplets with minimal harm to its chemical properties or physical structure [Ahn and Kerbage, 2005]. In this chapter, passive sorting based on the interfacial properties of droplets is achieved by employing droplet guiding tracks that are obtained by laser ablation of thin (thickness $\sim 0.6 \mu m$) polydimethylsiloxane (PDMS) coatings over glass substrates. In the continuous phase of oil, pure water droplets are guided much better than water/surfactant droplets due to their larger interfacial tension (IFT) and larger contrast of contact angles (CAs) on surfaces inside and outside the guiding track. Schematic diagram of the microfluidic device used for droplet sorting is shown in Fig. 4.1(a). Initially, an analytical model is developed based on drag, frictional, and trapping forces [schematically shown in Fig. 4.1(b)] acting on a droplet. Droplet trajectories are obtained by this model using a finite difference time domain approach which reveals droplet velocities at different positions when the net force acting on the droplet is assumed to be 0. Subsequently, the results from the theoretical model are matched with systematic experiments using pure water droplets in oil. In these experiments, the effects of track slope and droplet

flow speed on their guiding are studied. Passive droplet sorting is then demonstrated using microfluidic devices in which emulsion droplets of pure water and water/sodium dodecyl sulphate (water/SDS) mixture are generated simultaneously. These experimental results are also verified by the theoretical model and it is shown that the interfacial properties of the droplets (IFT, CAs on surfaces inside and outside the track) play critical roles in determining their dynamic confinement inside a guiding track.

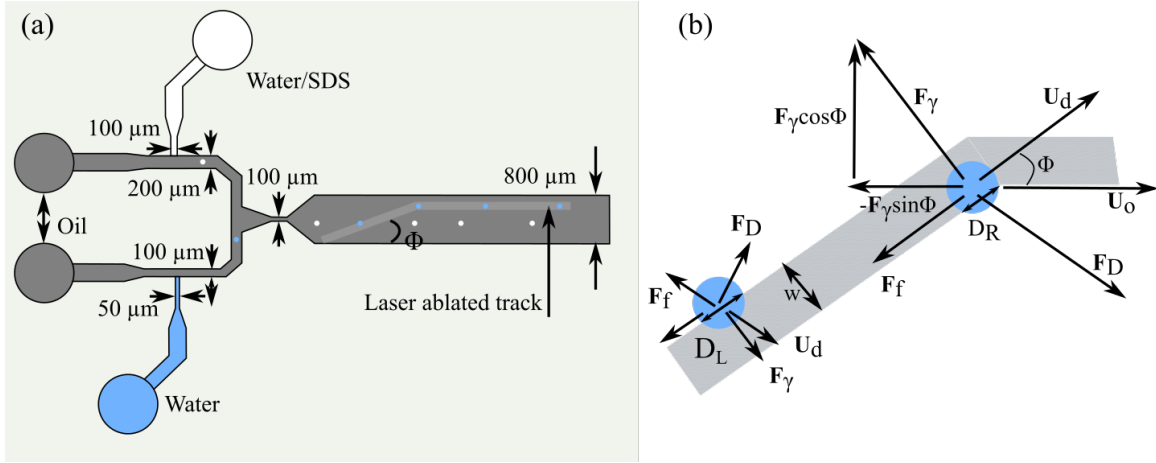


Figure 4.1: (a) Schematic diagram of the droplet sorting device. (b) Forces acting on a droplet guided in the track.

4.1 Materials and Methods

About 0.6 μm thick PDMS (Dow Corning, Sylgard 184) layers were spin coated on glass substrates and femtosecond (fs) laser micromachining technique was used for removal of the PDMS coatings along droplet guiding tracks. PDMS microfluidic devices were then obtained by aligning and consecutive bonding of a top microfluidic PDMS layer to the bottom substrate that contains a droplet guiding track. Microfluidic devices had two separate T-junctions for independent generation of droplets of two liquids which eventually enter a common tapered region and Hele-Shaw channel

as shown in Fig. 4.1(a). The tapered region with a width of $100\ \mu\text{m}$ (similar to droplet diameter) enabled the droplets from both liquids to flow at the center of the Hele-Shaw channel. Droplet guiding tracks were designed to have inclined sections at angles, Φ , of 5° (Chip A), 10° (Chip B and Chip D) and 15° (Chip C) and then a straight section as shown in Fig. 4.1(a). For each chip, the width of the droplet guiding track was kept constant at about $110\ \mu\text{m}$. Due to slight misalignments of the droplet guiding tracks with respect to the Hele-Shaw channels, Φ values were measured to be 5.5° , 9.5° , 15.5° , and 10.1° for chips A, B, C and D, respectively.

For systematic studies of droplet guiding, chips A, B and C were used where the top dispersed phase inlet was blocked by not punching the inlet hole. Olive oil was injected at the continuous phase from both T-junctions and droplet liquid (water or water/SDS) was injected from the disperse phase using syringe pumps. Oil flow rate from the bottom inlet was kept constant at $25\ \mu\text{L}/\text{h}$, while, the oil flow rate from the top inlet was varied between $20\ \mu\text{L}/\text{h}$ and $280\ \mu\text{L}/\text{h}$. This scheme worked well to achieve broad range of droplet velocities without considerably changing droplet size. For demonstration of droplet sorting using Chip D, both dispersed phase inlets had punched inlet holes such that water and water/SDS droplets were generated in olive oil from the top and bottom inlets, respectively. Water/SDS solutions were prepared with a final SDS concentration of $10\ \text{mM}$. Blue dye was added to pure water in order to enable visual differentiation of water droplets from water/SDS droplets. Because water/SDS droplets have a much smaller IFT, under the same flow conditions, T-junctions with similar dimensions generate much smaller water/SDS droplets as compared to water droplets. In order to keep the sizes of both droplet types similar, the widths of both continuous phase and dispersed phase inlets of the T-junction for generating water/SDS droplets were kept double in size as shown in Fig. 4.1(a). The typical droplet diameter for generated water and water/SDS droplets was about $100\ \mu\text{m}$. For Chip D, water and water/SDS were injected at a flow rate of $1\ \mu\text{L}/\text{h}$, while oil flow rate was kept at $25\ \mu\text{L}/\text{h}$ in each of the oil inlet.

4.2 Modeling

The model used for droplet guiding considers the drag force (\mathbf{F}_D), frictional force (\mathbf{F}_f) and trapping force (\mathbf{F}_γ) that are schematically shown in Fig. 4.1(b). Obtained as the sum of viscous drag, $\mathbf{F}_{D,v}$ and pressure drag, $\mathbf{F}_{D,p}$ contributions, \mathbf{F}_D is given as [Dangla et al., 2011, Beatus et al., 2012]:

$$\mathbf{F}_D = \mathbf{F}_{D,p} + \mathbf{F}_{D,v} = \xi \left(\mathbf{U}_o - \frac{\mathbf{U}_d}{2} \right) \quad (4.1)$$

where $\xi = 24\pi\mu\frac{R_2^2}{h} \left(1 + 2\frac{K_1(q)}{qK_0(q)} \right)$ is the drag coefficient, μ is the viscosity of host fluid, R_2 is the central radius of the squeezed droplet inside the track, h is the channel height, and \mathbf{U}_o and \mathbf{U}_d are the oil and average droplet velocities. $q = 2\sqrt{3} R_2/h$ and K_0 and K_1 are the modified Bessel functions of the second kind [Pit et al., 2016]. Frictional force acting on the moving droplet is modeled as $\mathbf{F}_f = -\beta\mathbf{U}_d$ where β is the friction coefficient [Beatus et al., 2012]. In the absence of track, the terminal velocity ratio of droplet and oil, ($\alpha = U_d/U_o$) was measured to be 0.85 for water droplet and 1.55 for water/SDS droplet. At the low-Reynolds limit, $Re \ll 1$, inertial effects are negligible and the net force acting on the droplet must be 0. Therefore, the value of β can be derived as follows:

$$\mathbf{F}_D + \mathbf{F}_f = 0 \quad (4.2a)$$

$$\xi \left(\mathbf{U}_o - \frac{\mathbf{U}_d}{2} \right) - \beta\mathbf{U}_d = 0 \quad (4.2b)$$

$$\beta = \xi \left(\frac{1}{\alpha} - \frac{1}{2} \right) \quad (4.2c)$$

β values are determined to be 0.68ξ and 0.14ξ for water and water/SDS droplets respectively. Within a guiding track, a droplet experiences the trapping force, \mathbf{F}_γ , exerted at a right angle to the track boundaries as shown in Fig. 4.1(b), which tends to hold the droplet within the track. In general, \mathbf{F}_γ can be composed of trapping forces due to droplet surface energy gradient, $F_{\gamma,s}$, [Dangla et al., 2011] and due to the wetting defect, $F_{\gamma,w}$, inside the track [Pit et al., 2016]. The total F_γ can be

written as the sum of the two forces as:

$$F_\gamma = \gamma \frac{\Delta A}{d} + \gamma(D_R - D_L)(\cos \theta_t - \cos \theta_p) \quad (4.3)$$

where γ is the IFT, D_L and D_R are the droplet lengths overlapping with the left and right track edges [see Fig. 4.1(b)], θ_t and θ_p are the CAs of droplet over track and PDMS surfaces respectively and d is the incremental displacement covered by the droplet.

4.2.1 Volume of a Flattened Droplet

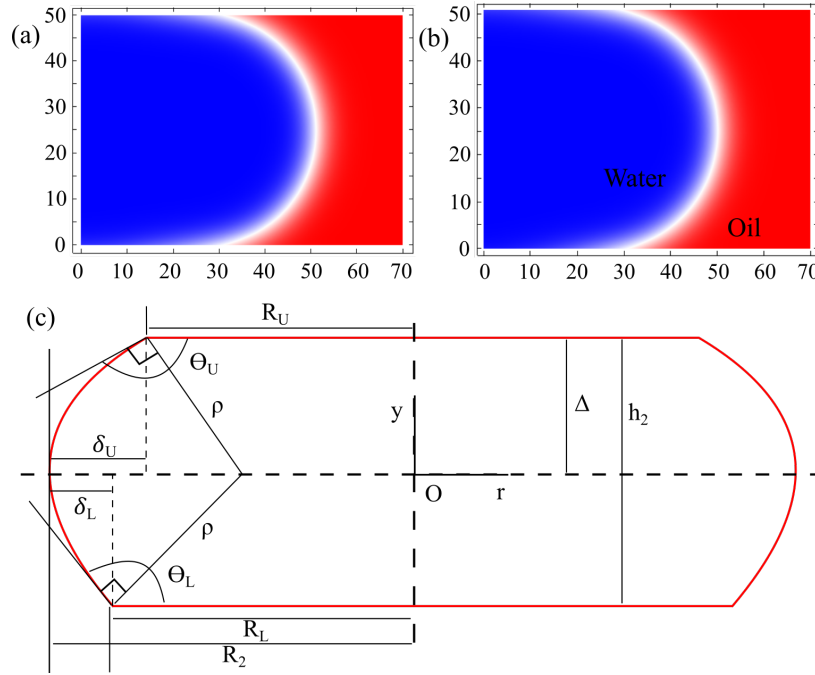


Figure 4.2: Simulated profiles of a flattened droplet a) outside the guiding track ($\theta_L = 172^\circ$, $h_1 = 50 \mu\text{m}$) and b) inside the guiding track ($\theta_L = 167.5^\circ$, $h_2 = 51 \mu\text{m}$). (c) Geometry of an asymmetric flattened droplet assumed in the derivation of expressions for the droplet volume.

In order to determine the droplet profile inside the microfluidic channel, FEM analysis is carried out, specifying the channel height and CAs for the top and bottom

walls of the channel. When a droplet of pure water is outside the guiding track, the channel height is $h_1 = 50 \mu\text{m}$ and the top and bottom surfaces are both PDMS with CAs $\theta_U = \theta_L = 172^\circ$ [see Fig. 4.2(a)]. When the same droplet is inside the guiding track, the channel height is $h_2 = 51 \mu\text{m}$, the top surface is PDMS ($\theta_U = 172^\circ$) and the bottom surface is ablated PDMS with CA $\theta_L = 167.5^\circ$ [see Fig. 4.2(b)]. In both cases, the droplet is flattened by the top and bottom channel walls; in addition, the droplet is asymmetric inside the track due to different CAs at the top and bottom surfaces. For asymmetric flattened droplets with cross-sectional profile shown in Fig. 4.2(c), general mathematical expressions are derived for the volume and surface area of the droplet to be used in calculating the confinement force. Initially, the radius of curvature, ρ , of the round lateral surface of the droplet is evaluated in terms of the top and bottom CAs, θ_U and θ_L , and the height of the channel, h_2 [See Eq. (4.4c)]. The radii, R_U and R_L of the upper and lower contact areas between the droplet and the channel walls are then calculated from the apparent lateral radius R_2 of the droplet as:

$$\frac{\Delta}{\rho} = \sin(\theta_U - \frac{\pi}{2}) = -\cos \theta_U \quad (4.4a)$$

$$\frac{h_2 - \Delta}{\rho} = \sin(\theta_L - \frac{\pi}{2}) = -\cos \theta_L \quad (4.4b)$$

$$\rho = -\frac{h_2}{\cos \theta_U + \cos \theta_L} \quad (4.4c)$$

$$R_U = R_2 - \delta_U = R_2 - \rho[1 - \sin \theta_U] \quad (4.4d)$$

$$R_L = R_2 - \delta_L = R_2 - \rho[1 - \sin \theta_L] \quad (4.4e)$$

For the case of a symmetric droplet located outside the guiding track, $\theta_U = \theta_L = \theta$, $R_U = R_L = R$, $R_2 = R_1$ and $h_2 = h_1$, and the radius R of the contact areas can be represented as:

$$R = R_1 + \frac{h_1}{2 \cos \theta} (1 - \sin \theta) \quad (4.5)$$

In order to calculate the volume, V , of the droplet, consider Fig. 4.2(c). Because the droplet has rotational symmetry with respect to the y-axis, its top half can be

represented as a stack of elementary circular disks centered on the y-axis, with radii that depend on the y-coordinate as:

$$r(y) = R_U + \delta_U(y) = R_U + \sqrt{\rho^2 - y^2} - \rho \sin \theta_U \quad (4.6)$$

The volume, V_U , of the upper half of the droplet is then given as:

$$V_U = \int_0^\Delta \pi r^2(y) dy = \pi \int_0^\Delta \left(R_U + \sqrt{\rho^2 - y^2} - \rho \sin \theta_U \right)^2 dy \quad (4.7a)$$

$$V_U = \pi \Delta \left[(R_U + \Delta \tan \theta_U) \left\{ R_U + \frac{\Delta}{\cos^2 \theta_U} \left(\theta_U - \frac{\pi}{2} \right) \right\} + \Delta^2 \left(\frac{1}{\cos^2 \theta_U} - \frac{1}{3} \right) \right] \quad (4.7b)$$

Similarly, the volume, V_L , of the lower half of the droplet is given by the following integral:

$$V_L = \int_0^{h_2 - \Delta} \pi r^2(y) dy = \pi \int_0^{h_2 - \Delta} \left(R_L + \sqrt{\rho^2 - y^2} - \rho \sin \theta_L \right)^2 dy \quad (4.8)$$

The total volume, V_2 , is then given by:

$$V_2 = V_U + V_L \quad (4.9)$$

For the symmetric droplet case outside the guiding track region, the upper and lower volumes are identical and the total volume, V_1 , is given by:

$$V_1 = \pi h_1 \left[\left(R + \frac{h_1 \tan \theta}{2} \right) \left\{ R + \frac{h_1}{2 \cos^2 \theta} \left(\theta - \frac{\pi}{2} \right) \right\} + \frac{h_1^2}{4} \left(\frac{1}{\cos^2 \theta} - \frac{1}{3} \right) \right] \quad (4.10)$$

The central radius of the droplet, R_1 , outside the track can be determined by examining experimental videos. From the known channel height, h_1 , and CA, θ , on the PDMS surface, the value of R - and, subsequently, the value of V_1 - can be calculated using Eqs. (4.5) and (4.10). When the droplet enters the track, its volume remains the same, but R_U and R_L are now different and R_1 changes to R_2 because of a different channel height, h_2 , and wetting asymmetry, ($\theta_L \neq \theta_U$). The value of R_2 can be determined from Eq. (4.9) upon substituting for R_U and R_L from Eqs. (4.4d) and (4.4e), inserting all other known quantities (h_2 , Δ , θ_L , θ_U), and using the volume

conservation $V_1 = V_2$. The volume conservation condition provides a transcendent equation for R_2 that can be solved numerically, by specifying R_1 as the initial guess to the solver. The found value of R_2 can be then used in calculating the droplet surface area.

4.2.2 Surface Area of a Flattened Droplet

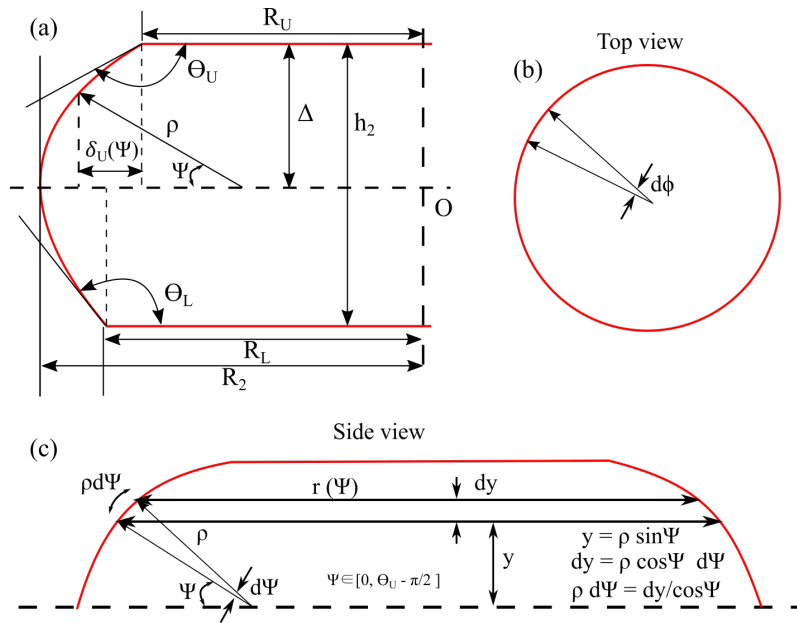


Figure 4.3: (a) Geometry of an asymmetric flattened droplet assumed in the derivation of expressions for the droplet surface area. (b) Top view of the droplet. (c) Full side view of the droplet.

The area of the lateral surface of a flattened droplet can be calculated by integrating over suitably chosen elements of the droplet surface, using the symmetry of the droplet. Again, divide the droplet into the top and bottom half, using the same geometrical considerations as in the volume calculations. This time, the dependent variable, $r(\psi)$, that enters into the integral is expressed as a function of polar angle, ψ , [see Fig. 4.3 for the definition of $r(\psi)$ and ψ]. Because the droplet has a rotational symmetry with respect to the y-axis, its top half can be represented as a stack of

elementary truncated cones centered on the y-axis, with base radii, $r(\psi)$ that depend on ψ as:

$$r(\psi) = R_U + \delta_U(\psi) = R_U + \rho \cos \psi - \rho \sin \theta_U \quad (4.11)$$

and half-apex angles, ψ , [see Fig. 4.3 (c)]. The total lateral area of the droplet is then equal to the sum of lateral areas of all stacked truncated conical slices. The element of the lateral surface area of the droplet can be expressed as:

$$dA_U = \{r(\psi)d\phi\}\rho d\psi \quad (4.12)$$

where $\phi \in [0, 2\pi]$ and $\psi \in [0, \theta_U - \pi/2]$. Substituting for $\rho = -\Delta/\cos \theta_U$ and integrating over the full ranges of ϕ and ψ gives the lateral surface area of the top half of the droplet as:

$$A_{U,lat} = -\frac{2\pi\Delta}{\cos \theta_U} \left[\{R_U + \Delta \tan \theta_U\} \left(\theta_U - \frac{\pi}{2} \right) + \Delta \right] \quad (4.13)$$

In a completely analogical fashion, the lateral surface area of the bottom half of the droplet is given by

$$A_{L,lat} = -\frac{2\pi(h_2 - \Delta)}{\cos \theta_L} \left[\{R_L + (h_2 - \Delta) \tan \theta_L\} \left(\theta_L - \frac{\pi}{2} \right) + h_2 - \Delta \right] \quad (4.14)$$

The total surface area equal to the sum of the lateral surface areas and contact areas between the droplet and the top and bottom channel walls can be expressed as:

$$A_2 = A_{U,lat} + A_{L,lat} + A_{U,con} + A_{L,con} \quad (4.15a)$$

$$= A_{U,lat} + A_{L,lat} + \pi R_U^2 + \pi R_L^2 \quad (4.15b)$$

For the symmetric case corresponding to a droplet located outside the track, the lateral surface area, ($A_{lat,sym}$), and total surface area, (A_1), are given as:

$$A_{lat,sym} = -\frac{2\pi h_1}{\cos \theta} \left[\left\{ R + \frac{h_1 \tan \theta}{2} \right\} \times \left(\theta - \frac{\pi}{2} \right) + \frac{h_1}{2} \right] \quad (4.16)$$

$$A_1 = A_{lat,sym} + 2\pi R^2 \quad (4.17)$$

4.2.3 Confinement Force Due to Droplet Shape

The confinement force, $F_{\gamma,s}$, acting on a droplet with interfacial tension, γ , due to the change of its surface area, A , is equal to the negative gradient of the surface energy, E , of the droplet: $F_{\gamma,s} = -\nabla E = -\gamma \nabla A$. When the droplet crosses the edge of the guiding track, its surface area changes only when the droplet has a displacement component in the direction, ζ , perpendicular to the track edge; thus, $F_{\gamma,s} = -\gamma dA/d\zeta$. In current situation, the actual value of $F_{\gamma,s}$ is approximated by its average value estimated by evaluating the total change in the droplet surface area ΔA :

$$F_{\gamma,s} = -\gamma \frac{dA}{d\zeta} \approx -\gamma \frac{\Delta A}{\Delta \zeta} = -\gamma \frac{\Delta A}{2R_L}. \quad (4.18)$$

In Eq. (4.18), $\Delta A = (A_2 - A_1)$ [$\Delta A = (A_1 - A_2)$] is the change of the droplet surface area upon moving from the outside to the inside [from the inside to the outside] of the track. The corresponding droplet displacement perpendicular to the track edge is then $\Delta \zeta = 2R_L$, equal to the diameter of the droplet contact area with the lower channel surface (see Fig. 4.4). It is assumed that R_L does not change when the droplet is inside and outside the track. Note that F_γ changes sign from negative to positive as droplet enters the track from left edge and exits from right edge.

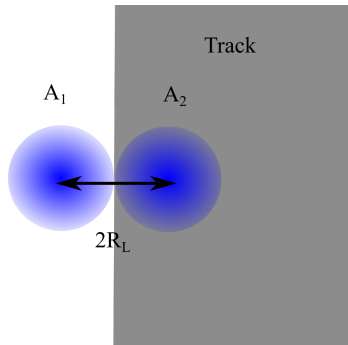


Figure 4.4: Interpolation of area of moving droplet across the track.

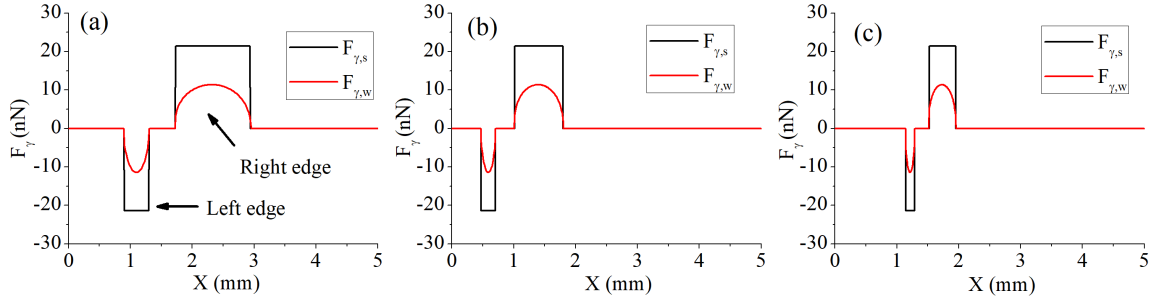


Figure 4.5: Trapping forces on water droplet passing through the track edges in (a) Chip A ($U_d = 2357 \mu\text{m/s}$), (b) Chip B ($U_d = 985 \mu\text{m/s}$) and (c) Chip C ($U_d = 528 \mu\text{m/s}$).

4.2.4 Equations of Motion

IFTs of water and water/SDS droplets in olive oil are $\gamma_w \sim 16 \text{ mN/m}$ [Than et al., 1988] and $\gamma_{w/SDS} \sim 2.5 \text{ mN/m}$ [Rashid et al., 2017], respectively. Droplet CAs were measured over PDMS and laser ablated surfaces by placing a $10 \mu\text{L}$ droplet immersed in oil. Average CAs for water (water/SDS) droplets were measured to be 172° and 167.5° (177° and 172°) over PDMS and laser ablated surfaces, respectively. Applying the equilibrium condition by equating the net force acting on the droplet to 0.

$$\mathbf{F}_D + \mathbf{F}_\gamma + \mathbf{F}_f = 0 \quad (4.19a)$$

$$\xi \left(U_o - \frac{U_{d,x}}{2} \right) - F_\gamma \sin \Phi - \beta U_{d,x} = 0 \quad (4.19b)$$

$$\xi \left(-\frac{U_{d,y}}{2} \right) + F_\gamma \cos \Phi - \beta U_{d,y} = 0 \quad (4.19c)$$

$$U_{d,x} = \frac{\xi U_o - F_\gamma \sin \Phi}{\beta + \xi/2} \quad (4.19d)$$

$$U_{d,y} = \frac{F_\gamma \cos \Phi}{\beta + \xi/2} \quad (4.19e)$$

$$x_{i+1} = x_i + U_{d,x} \Delta t \quad (4.19f)$$

$$y_{i+1} = y_i + U_{d,y} \Delta t \quad (4.19g)$$

By this multi-step iterative method, the position of droplet after each time step is determined to get overall droplet path. The magnitudes of both trapping forces over

the droplet when it passes through the track edges are plotted in Fig. 4.5

4.3 Results and Discussion

Figs. 4.6(a), 4.6(b) and 4.6(c) show the experimental and theoretical trajectories determined for water droplets in chips A, B, and C, respectively. In these sub-figures, the experimental trajectories of the droplets were determined by analyzing videos using a normalized cross-correlation algorithm, which also revealed droplet velocities at different positions in a given trajectory [Rashid et al., 2017]. In each sub-figure, the left plot shows experimental and theoretical trajectories for 5 droplets moving at different speeds, while the right plot shows all experimental trajectories of more than 30 droplets moving at different speeds. At low speeds, water droplets are observed to be fully guided. As droplet speed is increased, droplets start partially following the guiding track, leaving the track at a particular vertical distance, ΔH (the track exit height), which is measured with respect to their initial vertical position as they enter the Hele-Shaw channel. When the droplets are fully guided, they cover ΔH more than the critical value (ΔH_{crit}) which is measured from the center of the Hele-Shaw channel to the lower track edge as shown in Fig. 4.6(b). ΔH_{crit} for chips A, B and C were measured to be $260 \mu m$, $270 \mu m$ and $270 \mu m$ respectively. The maximal speed at which the droplet can be fully guided decreases with increasing Φ .

Fig. 4.7(a) shows the variation of ΔH as a function of U_d measured using water droplets in chips A, B and C together with predictions obtained using the theoretical trajectories. Horizontal plateaus observed at low U_d values in Fig. 4.7(a) indicate full droplet guiding. Deviations between the ΔH values corresponding to the horizontal plateaus for each chip are due to slight misalignments in the droplet guiding tracks with respect to the Hele-Shaw channels. A good match is observed between the theoretical curves and experimental data points in Fig. 4.7(a), especially for chips B and C.

For highest speeds ($U_d > 1000 \mu m$), the droplets undergo slight vertical deflection

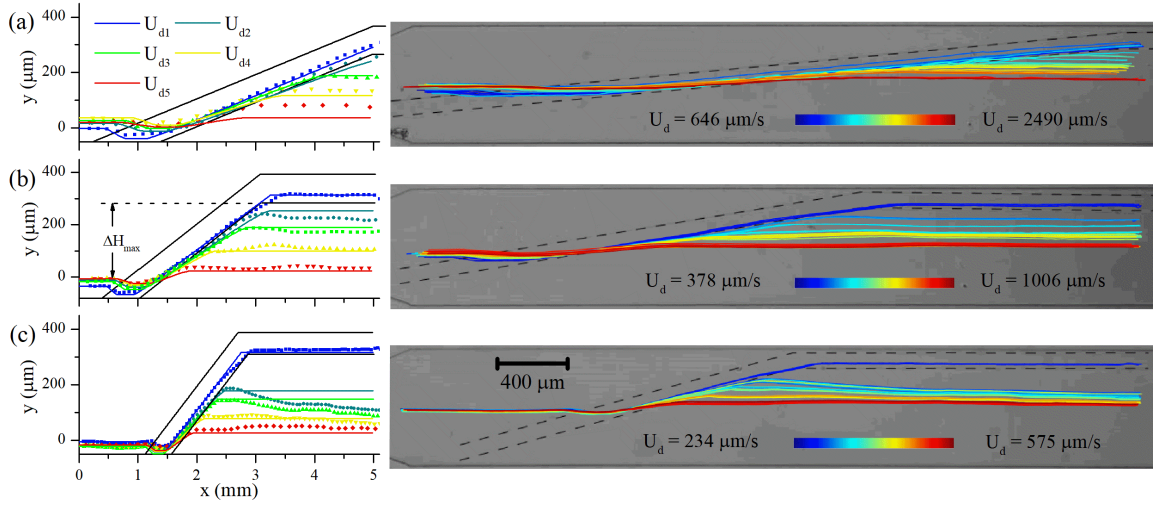


Figure 4.6: Experimental (dashed) and simulated (solid) trajectories of water droplets at different U_d in (a) Chip A [$U_{d(1,2,3,4,5)} = (660, 1060, 1218, 1533, 2357) \mu\text{m/s}$], (b) Chip B [$U_{d(1,2,3,4,5)} = (378, 463, 490, 510, 985) \mu\text{m/s}$] and (c) Chip C [$U_{d(1,2,3,4,5)} = (234, 272, 293, 347, 528) \mu\text{m/s}$].

experimentally which causes deviation from theoretical points for all chips. This disagreement is attributed to the presence of inhomogeneities at the track edge due to the accumulation of residual PDMS after laser ablation which further enhance the droplet confinement within the track. In accordance with the expectations, Fig. 4.7(a) shows that, for similar U_d values, guiding of water droplets is improved (*i.e.* larger ΔH values are reached) with decreasing Φ . Hence, for a given U_d , a desired ΔH can be achieved by designing a guiding track with an appropriate track angle Φ . Such a deviation of ΔH with U_d can also be used for directing droplets with different speeds to specific compartments at different vertical positions. Results of the droplet experiments performed in chips A, B, and C using water/SDS droplets are shown in Fig. 4.7(b) together with theoretical predictions. For this case, experimental points indicate very small partial guiding of droplets despite almost no droplet guiding predicted by the theoretical model. Experimentally observed very small guiding of water/SDS droplets can be attributed to the inhomogeneities at track edges caused

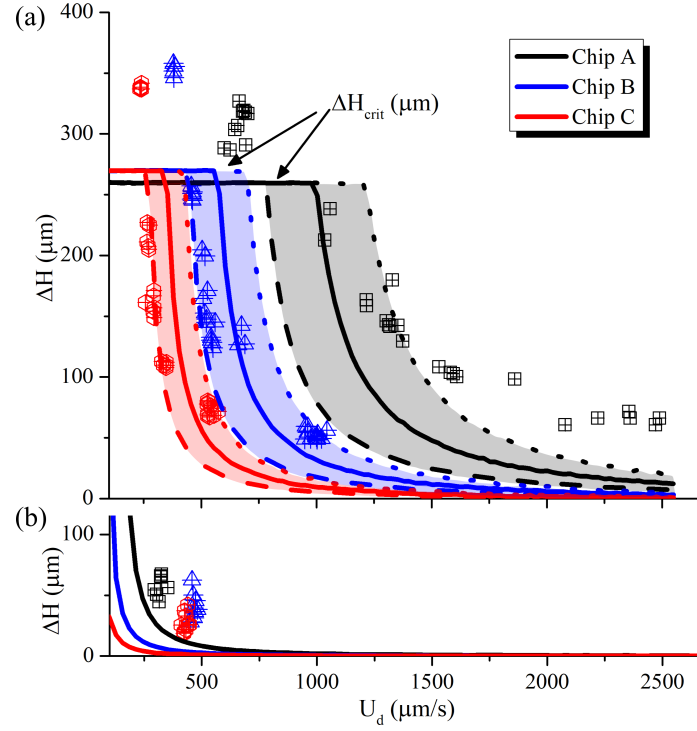


Figure 4.7: Track exit height ΔH of (a) water and (b) water/SDS droplets as a function of U_d . For each chip shown in part (a), the three solid lines indicate theoretical results carried out with $\theta_p = 172^\circ$, $\theta_t = [161^\circ (- - -), 163^\circ (—), \text{and } 165^\circ (\dots)]$. In part (b), $\theta_t = 172^\circ$ and $\theta_p = 177^\circ$.

by residual PDMS accumulated after laser ablation. Hence, Figs. 4.7(a) and 4.7(b) show a clear contrast in ΔH values observed for water and water/SDS droplets for same chips and U_d values. This large contrast constitutes the essence of the droplet sorting mechanism demonstrated in this paper.

Sorting of water and water/SDS droplets of similar sizes that are concurrently generated in Chip D is demonstrated in Fig. 4.8. In this experiment, the bottom and top T-junctions are used for generation of water and water/SDS droplets, and the frequency of droplet generation from both T-junctions is kept sufficiently small to ensure propagation of droplets in the Hele-Shaw channel without merging. Two experimental trajectories determined for exemplary water and water/SDS droplets are

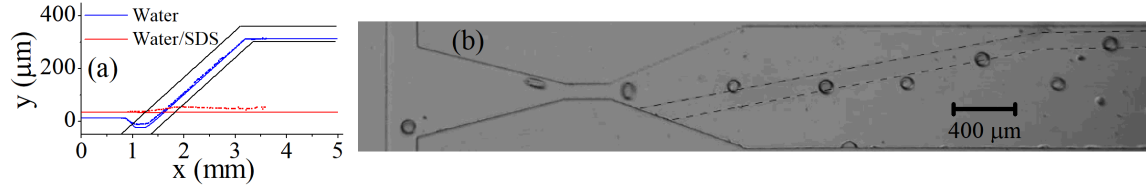


Figure 4.8: Sorting of water ($U_d = 337 \mu\text{m/s}$) and water/SDS ($U_d = 609 \mu\text{m/s}$) droplets in Chip D. (a) Experimental (dashed) and simulated (solid) trajectories of water and water/SDS droplets. (b) Merged image showing trajectories followed by a water and water/SDS droplet in Chip D. Water/SDS droplet can be identified by its slightly lighter color and increased deformation due to higher velocity and lower IFT.

shown in dashed lines in Fig. 4.8(a) together with theoretically predicted trajectories shown in solid lines. These trajectories clearly show water droplet being fully guided while the water/SDS droplet being almost completely unguided by the track. Image shown in Fig. 4.8(b) is an exemplary image demonstrating sorting of water and water/SDS droplets that is obtained by merging camera snapshots recorded at different times. In this image, snapshots are taken from the same water or water/SDS droplet while it passes through the tapered and guiding track regions of the microfluidic chip.

Chapter 5

MODELING OF OPTOFLUIDIC HOLEY FIBER DYE LASER

In this chapter, modeling of a holey fiber dye laser is carried out using space dependent first order rate equations. Schematic diagram of a possible implementation of the model dye laser based on a holey fiber is shown in Fig. 5.1. The dye solution encapsulated within the fiber is continuously injected by a fluid pump, so that, the intracavity concentration of the dye is not affected by photobleaching. At the same time, the dye is optically pumped with external continuous wave (CW) laser light coupled into and guided along the fiber length. The gain medium can either directly overlap with the guided mode field for maximum excitation or it can couple to the evanescent tails of the mode for maximum propagation distance along the fiber. In general, the useful laser output power depends on the reflectivity R_2 of the cavity output mirror (see Fig. 5.1), which, therefore, has to be carefully optimized. In fiber-based lasers, abundant gain medium is efficiently excited and, thus, the internal power can reach high levels even for low values of R_2 . A realistic experimental system will suffer from additional losses due to imperfect coupling of light between the cavity and the fiber. These coupling losses can be estimated and included in the simulations by modifying the effective values of R_1 and R_2 . Besides, designing of optimum couplers that ensure coupling of both light and liquid flow in and out of the holey fiber is a very critical challenge for the success of the holey fiber dye lasers studied in this chapter [Cubillas et al., 2013, Gerosa et al., 2015]. Recently, various experimental demonstrations of pulsed dye lasers [Vasdekis et al., 2007, Yonenaga et al., 2015, Stolyarov et al., 2012], and pulsed [Nampoothiri et al., 2012] and CW [Nampoothiri

et al., 2015] gas lasers that employ holey fibers have been reported.

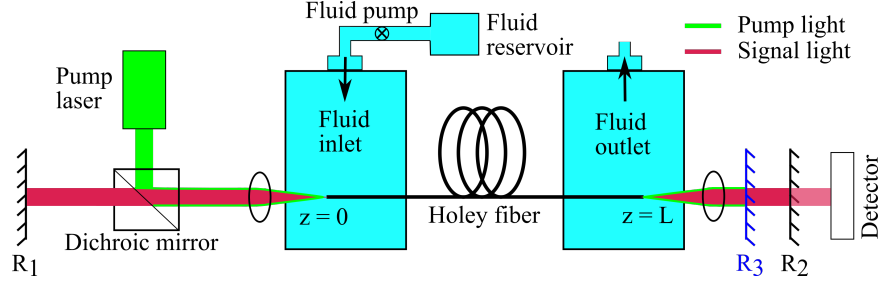


Figure 5.1: Schematic diagram of a model optofluidic dye laser based on a holey fiber of total length L filled with an aqueous dye solution circulating through the fiber. Fabry-Perot-type laser cavity is formed between the input mirror (reflectivity R_1) and the output mirror (reflectivity R_2). The optofluidic laser is pumped by an external laser source coupled to the system using a dichroic mirror. Pumping efficiency is further increased with a pump mirror (reflectivity R_3) that reflects the pump light back into the fiber while transmitting the signal light.

The purpose of this research work is to carry out a comprehensive performance analysis of optofluidic fiber dye lasers, using rate equations that describe the excited-state population of the gain medium and the spatial variation of the pump and signal powers in the steady state of laser operation. Three different geometries of holey fiber dye lasers are considered: double-cladding suspended-core fiber (SCF), double-cladding hollow-core fiber (HCF), and single-cladding HCF. The performance of holey fiber dye lasers for different concentrations of dye molecules and scattering loss coefficients is studied. It is observed that holey fiber dye lasers operate most efficiently at an optimum fiber length; this is true even in the absence of scattering losses in the system. For benchmarking purposes, the performance of dye jet lasers is also discussed. The analysis reveals that the performance of SCF-based dye lasers is considerably worse than all other cases due to very small coupling between the gain medium and the lasing mode. In contrast, double-cladding HCF-based dye lasers reach performance levels comparable to dye jet lasers, while single-cladding HCF-based dye lasers reach performance levels superior to all other cases.

5.1 Geometry of Holey Fibers and Characterization of Their Guided Modes

In the double-cladding SCF and double-cladding HCF geometries, it is assumed that the inner cladding confines the lasing mode propagating in the suspended or hollow signal core whereas the outer air cladding formed by a ring of air holes confines the pump light in the multimode pump core [see Figs. 5.2(a) and 5.3(a)]. In comparison with the standard single-cladding approach, this geometry provides a higher numerical aperture for coupling the pump light into the fiber (input NA ranging from 0.72 to 0.91), better thermal management, and lower pump losses [Franczyk et al., 2014]. As a third geometry, we consider single-cladding HCF, in which the pump beam is assumed to be fully coupled to the signal core that also confines the lasing mode. For the SCF design, the configuration used by Schartner *et al.* [Schartner et al., 2011] operating at 532 nm is assumed (Fig. 5.2). Laser gain medium formed by Rhodamine B dye dissolved in water fills the fiber holes surrounding the suspended core, indicated by blue color. Since the refractive index of the aqueous dye solution ($n_{cl} = 1.33$) is smaller than that of the suspended silica fiber core ($n_c = 1.45$), the fiber infiltrated with the dye solution retains its light-guiding capacity. HCF geometry shown in Fig. 5.3 is inspired by a commercially available photonic crystal fiber [NKT,]. The fiber is operated as a liquid-core light guide, with the central core opening infiltrated with aqueous dye solution and inner cladding holes filled with air ($n_{air} = 1$; see Fig. 5.3(b) for details) [Van et al., 2017]. Consequently, a fiber that guides light due to the effective refractive index mechanism is obtained; the light is strongly confined within the central hole filled with aqueous dye solution by total internal reflection for all visible wavelengths. The only difference between the double-cladding and single-cladding HCF geometry is the presence or absence of the outer air cladding in the fiber cross-section.

Finite element method (FEM) is used to calculate the distributions of the electric and magnetic fields of fundamental guided modes in holey fibers at the signal (lasing)

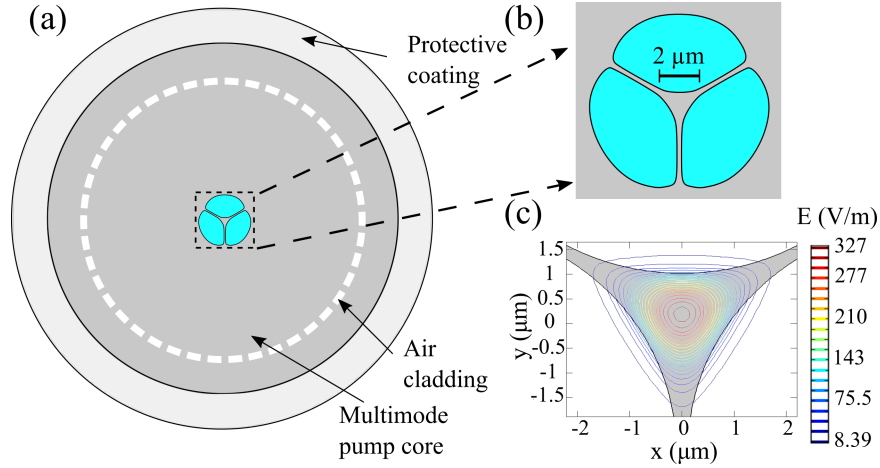


Figure 5.2: Suspended-core fiber for optofluidic dye lasers. (a) Double-cladding SCF geometry, (b) magnified view of the hole region filled with dye solution (blue color) and (c) distribution of the electric field amplitude $|E(x, y)|$ of the fundamental guided mode at 560 nm. Fiber design parameters: $A^{liquid} = 8.80 \times 10^{-7} \text{cm}^2$.

wavelength, $\lambda_s = 560 \text{ nm}$. Transverse profiles of the electric field amplitude, $|E(x, y)|$, are shown in Figs. 5.2(c) and 5.3(c) for SCF and HCF, respectively. Knowing the transverse profile of the guided-mode fields, signal filling factor, Γ_s , can be calculated as the ratio of the signal power contained within the liquid-filled region, P_s^{liquid} , to the total power, P_s^{total} , of the guided signal mode as [Gong et al., 2007]:

$$\Gamma_s = \frac{\int_{liquid} (E_x H_y - E_y H_x) dx dy}{\int_{total} (E_x H_y - E_y H_x) dx dy}. \quad (5.1)$$

Here, E_x, E_y (H_x, H_y) represent the position-dependent transverse components of the electric (magnetic) field of the guided signal mode. The pump filling factor, Γ_p , is considered to be 1 for the case of single-cladding HCF. For the double-cladding SCF and double-cladding HCF cases, assuming the pump light intensity is uniform within the multimode pump core, Γ_p is given by the ratio of the cross-sectional area of liquid-filled region, A^{liquid} , marked by blue color in Figs. 5.2(a) and 5.3(a) to the total cross-sectional area of the multimode pump core, A^{total} ($\Gamma_p = A^{liquid}/A^{total}$). For a fair comparison, Γ_p is assumed to have the same value of 0.02 for both studied

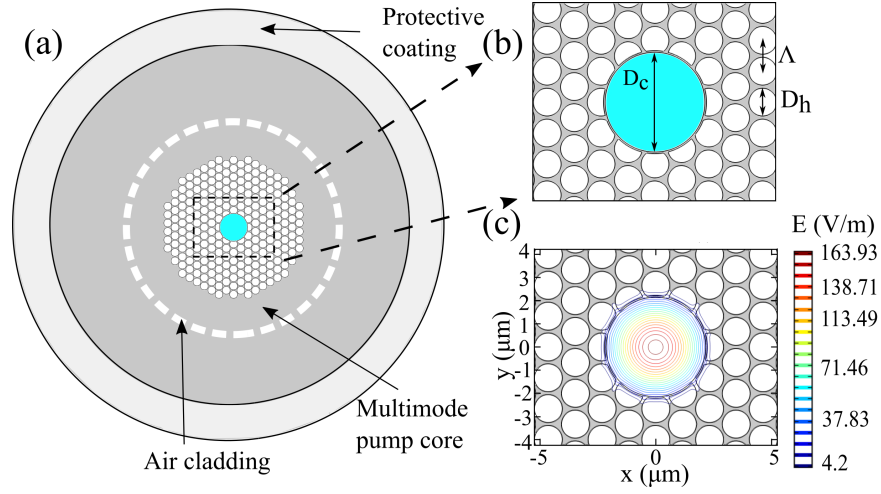


Figure 5.3: Hollow-core fiber for optofluidic dye lasers. (a) Double-cladding HCF geometry, (b) magnified view of the central hole filled with dye solution (blue color) and (c) distribution of the electric field amplitude $|E(x, y)|$ of the fundamental guided mode at 560 nm. Fiber design parameters: $D_c = 4.7 \mu\text{m}$, $D_h = 1.2 \mu\text{m}$, $D_h/\Lambda = 0.9$.

double-cladding cases.

5.2 Modeling of Holey Fiber Dye Lasers

The following system of nonlinear, coupled differential equations was employed in modeling the operation of holey fiber dye lasers [Aas et al., 2016, Kelson and Hardy, 1999]:

$$\frac{N_2(z)}{N} = \frac{\frac{P_p^{tot}(z)\Gamma_p\lambda_p\sigma_{ap}}{A_p} + \frac{P_s^{tot}(z)\Gamma_s\lambda_s\sigma_{as}}{A_s}}{\frac{hc}{\tau} + \frac{P_p^{tot}(z)\Gamma_p\lambda_p\sigma_p^{tot}}{A_p} + \frac{P_s^{tot}(z)\Gamma_s\lambda_s\sigma_s^{tot}}{A_s}}, \quad (5.2)$$

$$\pm \frac{dP_p^\pm(z)}{dz} = \Gamma_p [\sigma_p^{tot} N_2(z) - \sigma_{ap} N] P_p^\pm(z) - \alpha_p P_p^\pm(z), \quad (5.3)$$

$$\pm \frac{dP_s^\pm(z)}{dz} = \Gamma_s [\sigma_s^{tot} N_2(z) - \sigma_{as} N] P_s^\pm(z) - \alpha_s P_s^\pm(z). \quad (5.4)$$

In these equations, $N_2(z)$ is the population density of the upper lasing level, $P_p(z)$ and $P_s(z)$ represent the pump and signal powers as a function of distance z measured along the fiber, and the superscripts "+" and "-" correspond to the forward- and backward-

propagating pump and signal powers, respectively. $P_{p(s)}^{tot}(z) = (P_{p(s)}^+(z) + P_{p(s)}^-(z))$ denotes the sum of the forward- and backward-propagating pump (signal) powers, $\sigma_{p(s)}^{tot} = (\sigma_{ap(as)} + \sigma_{ep(es)})$ is the sum of the absorption and stimulated emission cross-sections at the pump (signal) wavelength, $\alpha_p(\alpha_s)$ is the scattering loss coefficient at the pump (signal) wavelength, τ is the fluorescence lifetime of the excited state, N is the uniform concentration of the gain medium, and $A_{p(s)}$ is the effective overlap area of the pump (signal) beam with the liquid gain medium. Since the pump light is assumed to be uniform across the multimode pump core, $A_p = A^{liquid}$. The same definition of A_p is also adopted for the single-cladding HCF. A_s is calculated using the concept of effective mode area as [Agarwal, 2001]:

$$A_s = \frac{\left(\int \int_{liquid} |E(x, y)|^2 dx dy \right)^2}{\int \int_{liquid} |E(x, y)|^4 dx dy}. \quad (5.5)$$

In Eq. (5.5), integration is carried out over the liquid-filled cross-sectional area. Values of all parameters that appear in our calculations are listed in Table 5.1; some of them are material constants while the remaining ones are calculated by FEM simulations described in the previous section. Taking the pump power coupled into the fiber at $z = 0$ to be P_{in} , the solution of the coupled differential equations (5.2) – (5.4) is carried out subject to four boundary conditions: $P_p^+(0) = P_{in}$, $P_p^-(L) = R_3 P_p^+(L)$, $P_s^+(0) = R_1 P_s^-(0)$ and $P_s^-(L) = R_2 P_s^+(L)$, where L is the total length of the fiber. When solving the coupled differential equations (5.2)–(5.4) $P_p^-(0)$ and $P_s^-(0)$ are initially guessed using the shooting method [Kelson and Hardy, 1999]. Subsequently, the guessed values are adjusted by the nonlinear solver after several iterations to satisfy the boundary conditions at $z = L$ for both pump and signal powers. In all calculations, R_1 and R_3 are considered to be 0.99, while R_2 is considered to be 0.50 except for the results presented in Fig. 5.10, where R_2 is a variable.

In the following, detailed numerical analysis of the different geometries of holey fiber dye lasers introduced in Section II is carried out. Among these geometries, double-cladding SCF layout is observed to perform considerably worse than both

Table 5.1: Descriptions and numerical values of parameters used in the rate equation model [Aas et al., 2016, Kelson and Hardy, 1999]

Parameter	Description	Num. value
λ_p	Pump wavelength	532 nm
λ_s	Signal wavelength	560 nm
σ_{ap}	Absorption cross section at λ_p	$3.42 \times 10^{-16} \text{ cm}^2$
σ_{as}	Absorption cross section at λ_s	$1.00 \times 10^{-16} \text{ cm}^2$
σ_{ep}	Stimulated emission cross section at λ_p	$2.00 \times 10^{-17} \text{ cm}^2$
σ_{es}	Stimulated emission cross section at λ_s	$3.78 \times 10^{-16} \text{ cm}^2$
α_p	Scattering loss coefficient at λ_p	$2 \times 10^{-4} \text{ cm}^{-1}$
α_s	Scattering loss coefficient at λ_s	$2 \times 10^{-4} \text{ cm}^{-1}$
$A_{p,\text{SCF}}$	Area of pump overlap with liquid in SCF	$8.80 \times 10^{-7} \text{ cm}^2$
$A_{s,\text{SCF}}$	Area of signal overlap with liquid in SCF	$8.18 \times 10^{-9} \text{ cm}^2$
$A_{p,\text{HCF}}$	Area of pump overlap with liquid in HCF	$1.73 \times 10^{-7} \text{ cm}^2$
$A_{s,\text{HCF}}$	Area of signal overlap with liquid in HCF	$1.73 \times 10^{-7} \text{ cm}^2$
τ	Fluorescence lifetime	4 ns
$\Gamma_{s,\text{SCF}}$	Signal filling factor for SCF	0.0143
$\Gamma_{s,\text{HCF}}$	Signal filling factor for HCF	0.9957
n_c	Refractive index of silica	1.45
n_{cl}	Refractive index of aqueous dye solution	1.33
R_1	Reflectivity of input mirror	0.99
R_2	Reflectivity of output mirror	0.50
R_3	Reflectivity of pump mirror	0.99
h	Planck's constant	$6.63 \times 10^{-34} \text{ J.s}$
c	Speed of light	$3.00 \times 10^8 \text{ m/s}$

double-cladding HCF and single-cladding HCF layouts in terms of the threshold pump power and slope efficiency. Therefore, the initial analysis is performed only for the double-cladding and single-cladding HCF geometries, and the double-cladding SCF geometry is discussed only briefly at the end of Section III. In order to ensure the studied laser systems operate above the threshold, P_{in} is chosen to be 1 W for the double-cladding and single-cladding HCF laser calculations and 25 W for the double-cladding SCF laser calculations. In all calculations, the value of α_p was kept constant at $2 \times 10^{-4} \text{ cm}^{-1}$.

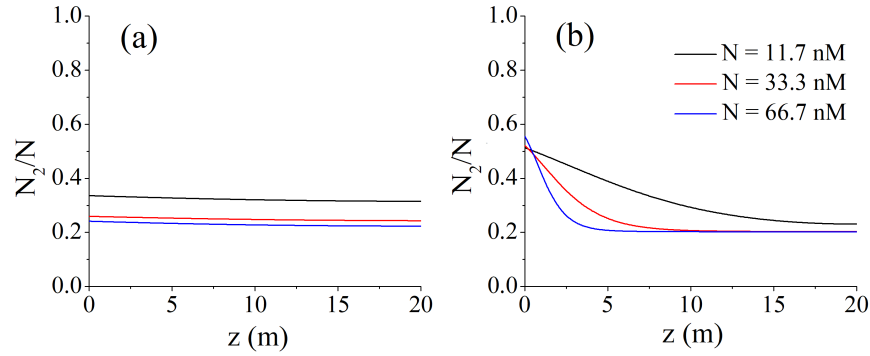


Figure 5.4: Normalized population of the upper lasing level, $N_2(z)/N$, at different N in (a) double-cladding and (b) single-cladding HCF dye lasers.

5.2.1 Spatial Variations of Upper Lasing Level Population

For typical laser systems based on rare-earth-doped fibers, $\sigma_{as} \ll \sigma_{es}$ and $\sigma_{as} \ll \sigma_{ap}$. This results in the second term in the numerator of Eq. (5.2) being negligible with respect to the first term, leading to a very small value of $N_2(z)/N$ everywhere along the fiber [Kelson and Hardy, 1999]. In contrast, for a dye-based gain medium, σ_{as} is of the same order as σ_{es} and σ_{ap} (for Rhodamine B, $\sigma_{es} \approx 3.78\sigma_{as}$ and $\sigma_{ap} \approx 3.42\sigma_{as}$). Higher absorption at the signal wavelength then results in $N_2(z)$ being of the same order of magnitude as N , which leads to larger values of $N_2(z)/N$. In Fig. 5.4, $N_2(z)/N$ is plotted along the fiber length calculated for double-cladding HCF [part (a)] and

single-cladding HCF [part (b)] for different values of N , assuming $\alpha_s = 2 \times 10^{-4} \text{ cm}^{-1}$ and the total fiber length $L = 20 \text{ m}$. It is notable that in the single-cladding HCF, the relative population of the upper lasing level $N_2(z)/N$ varies significantly with z , in contrast to the double-cladding HCF layout. This behavior results from highly efficient absorption of pump light by the gain medium in the single-cladding HCF geometry with $\Gamma_p = 1$; the gain medium is strongly pumped near the beginning of the fiber and pumping efficiency then falls off rapidly, as the pump beam is progressively absorbed by the dye molecules.

5.2.2 Spatial Variations of Pump and Signal Powers

Variation of the pump power $P_p^\pm(z)$ with distance z along the fiber is governed by Eq. (5.3). Since losses dominate the change in $P_p^\pm(z)$, both $P_p^+(z)$ and $P_p^-(z)$ decay along their respective directions of propagation. The profiles of $P_p^+(z)$ and $P_p^-(z)$ for three different values of N and $\alpha_s = 2 \times 10^{-4} \text{ cm}^{-1}$ are plotted in Fig. 5.5 for both double-cladding [part (a)] and single-cladding [part (b)] HCF. For the double-cladding HCF, $P_p^+(z)$ does not decay to 0 at $z = L$ due to a low Γ_p . On the other hand, for the single-cladding HCF with $N > 11.7 \text{ nM}$ and the total fiber length $L = 20 \text{ m}$, $P_p^+(z)$ decays virtually to 0 at $z = L$, as the pump beam is efficiently absorbed ($\Gamma_p = 1$). Hence, the power $P_p^-(z)$ of backward-propagating pump light can be neglected and the pump reflector R_3 (see Fig. 5.1) is effectively redundant in the system. However, when N and/or L are lowered, reflector R_3 becomes important for efficient pumping of the gain medium.

Eq. (5.4) describes the variation of the signal power $P_s^\pm(z)$ with distance z along the fiber. Within the initial section of the fiber where $N_2(z)$ reaches its highest values (see Fig. 5.4), stimulated emission dominates over absorption and scattering losses under proper parametric conditions and, consequently, $P_s^+(z)$ is gradually amplified. At the point $z = z_{\text{max}}$ where the gain is exactly equal to the sum of absorption and scattering losses, $P_s^+(z)$ reaches a maximum. Since $N_2(z)$ is monotonically decreasing

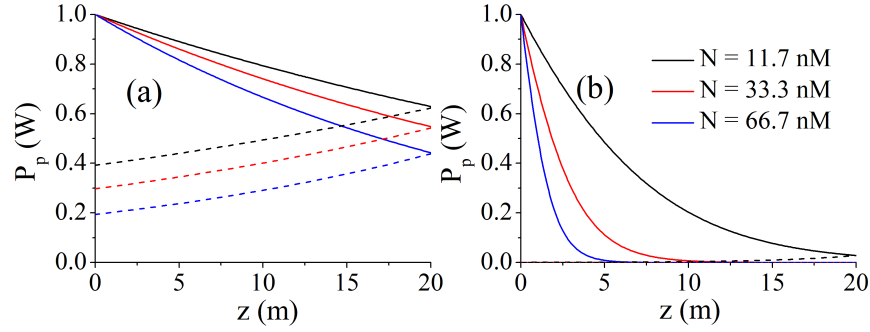


Figure 5.5: $P_p^+(z)$ (—) and $P_p^-(z)$ (- -) at different N in (a) double-cladding and (b) single-cladding HCF dye lasers.

with z , for $z > z_{\max}$, losses become dominant, leading to a gradual decrease of $P_s^+(z)$. In general, this trend is observed even in the absence of scattering losses (i.e. for $\alpha_s = 0$). Hence, there is always an optimum fiber length, $L_{opt} = z_{\max}$, at which $P_s^+(z)$ is maximum. At this optimum length, maximum output power can be obtained from the holey fiber dye laser. For a cavity with an output coupler of reflectivity R_2 , this maximum output power can be expressed as: $P_{out}(L_{opt}) = P_s^+(L_{opt})[1 - R_2]$. Spatial profiles of $P_s^+(z)$ and $P_s^-(z)$ are plotted for three different values of N assuming $\alpha_s = 2 \times 10^{-4} \text{ cm}^{-1}$ in Fig. 5.6. The rate of change of $P_s^+(z)$ with z depends directly on the variations of $N_2(z)$. Since $N_2(z)$ falls off more rapidly for larger N for both fiber types (see Fig. 5.4), maximum of $P_s^+(z)$ shifts to a smaller value of z_{\max} and $P_s^+(z)$ increases and decays faster. According to Eq. (5.4), the dynamics of spatial changes of $P_s^\pm(z)$ is also determined by scattering losses. The distributions of $P_s^+(z)$ and $P_s^-(z)$ along the fiber length at $N = 33.3 \text{ nM}$ and three different values of α_s are shown in Fig. 5.7. Clearly, an increase in α_s leads to an overall decrease in the value of $P_s^\pm(z)$ due to larger losses within the laser cavity. At the same time, with higher scattering losses, $P_s^+(z)$ reaches its maximum at lower values of z ; thus, L_{opt} is also reduced.

The optimum fiber length L_{opt} is determined by an interplay between the dye concentration, scattering losses, and pump power. Due to the nonlinear nature of

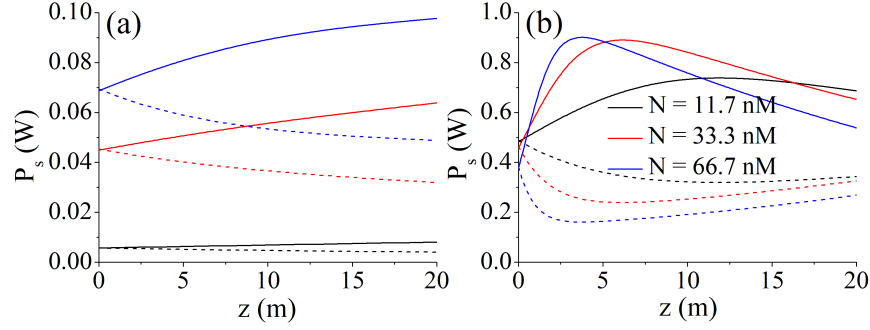


Figure 5.6: $P_s^+(z)$ (—) and $P_s^-(z)$ (- - -) at different N in (a) double-cladding and (b) single-cladding HCF dye lasers, assuming $\alpha_s = 2 \times 10^{-4} \text{ cm}^{-1}$.

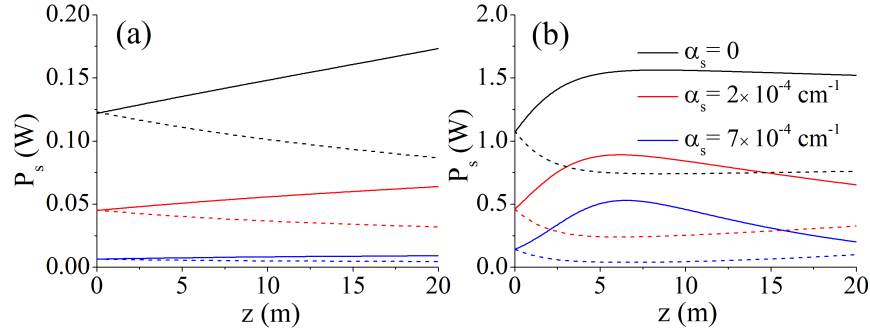


Figure 5.7: $P_s^+(z)$ (—) and $P_s^-(z)$ (- - -) at different α_s in (a) double-cladding and (b) single-cladding HCF dye lasers, assuming $N = 33.3$ nM.

the system, L_{opt} is a variable that changes when the fiber length L is changed. In order to determine the value of L_{opt} , at which the fiber-dye laser provides the highest possible signal power, Eqs. (5.2) - (5.4) are solved iteratively for different values of L and considered the value of L_{opt} that maximized the peak of the spatial profile of P_s^+ . The variation of L_{opt} with N at different values of α_s is plotted in Figs. 5.8(a) and 5.8(b) for double-cladding and single-cladding HCF dye lasers respectively. Due to less efficient absorption of the pump light in the double-cladding HCF geometry with smaller Γ_p , double-cladding HCF lasers display values of L_{opt} that are consistently higher than those of single-cladding HCF lasers for all values of N . For a given HCF geometry, higher absorption of the pump and signal light at higher N results in smaller

L_{opt} . The total output power at the optimum fiber length $P_{out}(L_{opt})$ is also shown in Fig. 5.8 as a function of N for double-cladding and single-cladding HCF lasers. In general, it is observed that laser operation at higher N is preferable for achieving maximum output power. As the dye concentration increases above $\sim 1 \mu\text{M}$, output power and optimum fiber length become relatively insensitive to small variations in α_s and the output power tends to saturate. Hence, good operating parameters for double-cladding HCF and single-cladding HCF are revealed as $[N \sim 1 \mu\text{M}, L_{opt} \sim 1 - 10 \text{ m}]$ and $[N \sim 1 \mu\text{M}, L_{opt} \sim 0.1 - 1 \text{ m}]$, respectively. Note that thermal and photobleaching effects are not included in our analysis. Both of these effects will generally result in changes in the optimum operating parameters of holey fiber dye lasers.

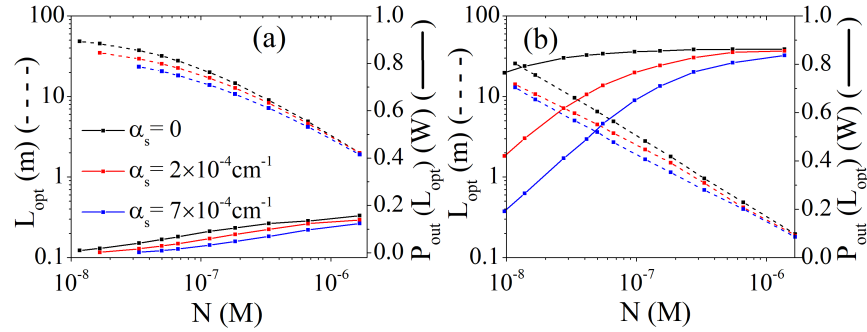


Figure 5.8: Variation of L_{opt} (---) and $P_{out}(L_{opt})$ (—) with N at different α_s in (a) double-cladding and (b) single-cladding HCF dye laser.

5.2.3 Threshold Pump Power and Slope Efficiency

In order to determine the slope efficiency η_{slope} and threshold pump power P_{th} of our holey fiber dye lasers, the coupled rate equations (5.2)–(5.4) are solved for increasing values of P_{in} and different values of R_2 . Assuming that the system was always operated at optimum conditions, which were different for each studied P_{in} and R_2 , the fiber length is set equal to L_{opt} and, subsequently, the output power of the laser is calculated as $P_{out}(L_{opt})$. Exemplary plots showing $P_{out}(L_{opt})$ as a function of P_{in} for $R_2 = 0.50$

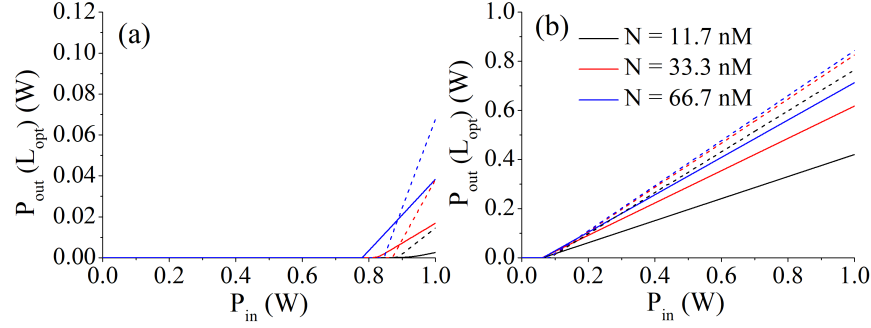


Figure 5.9: Variation of $P_{out}(L_{opt})$ with P_{in} at different N for $\alpha_s = 0$ (---) or $\alpha_s = 2 \times 10^{-4} \text{ cm}^{-1}$ (—) in (a) double-cladding and (b) single-cladding HCF dye laser.

are shown in Fig. 5.9. From the dependence of $P_{out}(L_{opt})$ on P_{in} , both η_{slope} and P_{th} can be directly determined. Fig. 5.10 shows the change in η_{slope} and P_{th} with R_2 for both double-cladding and single-cladding HCF lasers. For both geometries, η_{slope} and P_{th} are observed to decrease monotonically with R_2 . Hence, the trade-off between low P_{th} and high η_{slope} is clearly visible, and R_2 value should be carefully selected for the required operating regime.

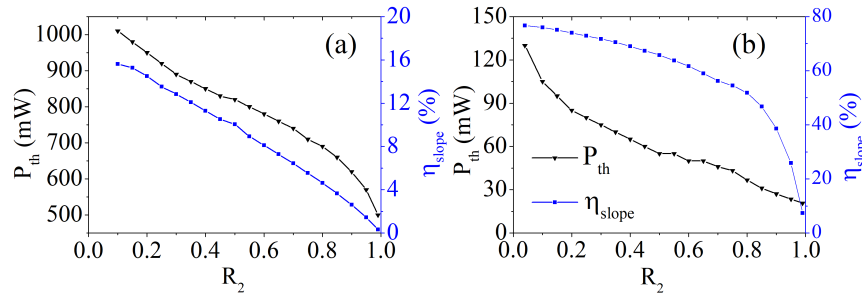


Figure 5.10: Variation of P_{th} and η_{slope} with R_2 at $N = 33.3 \text{ nM}$ in (a) double-cladding and (b) single-cladding HCF dye laser.

5.2.4 Optofluidic Fiber Dye Laser Summary

P_{th} , L_{opt} , and η_{slope} are the key characteristics of the holey fiber dye lasers studied in this research work. The values of these characteristic parameters as a function of N are summarized in Figs. 5.11(a), 5.11(b), and 5.12(b) for the double-cladding HCF, single-cladding HCF, and double-cladding SCF geometries, respectively. In these figures, both zero ($\alpha_s = 0$; dashed lines) and non-zero ($\alpha_s = 2 \times 10^{-4} \text{ cm}^{-1}$; solid lines) signal scattering losses are considered. For the double-cladding SCF, the value of P_{th} is larger than $\sim 15 \text{ W}$ and η_{slope} remains below 1% for all studied N and α_s . This results from the very small values of Γ_p and Γ_s that characterize this geometry and cause inefficient pumping of the gain medium and inefficient coupling of the dye emission to the guided lasing mode. Hence, it is concluded that the considered double-cladding SCF geometry performs significantly worse than the other two holey fiber dye laser geometries. Out of these two geometries, single-cladding HCF dye laser performs better than the double-cladding HCF dye laser in all aspects. With the single-cladding HCF geometry, P_{th} and η_{slope} values of $\sim 80 \text{ mW}$ and $> 90\%$ can be simultaneously achieved for $L_{opt} \sim 0.2 \text{ m}$ and $N \sim 1 \mu\text{M}$.

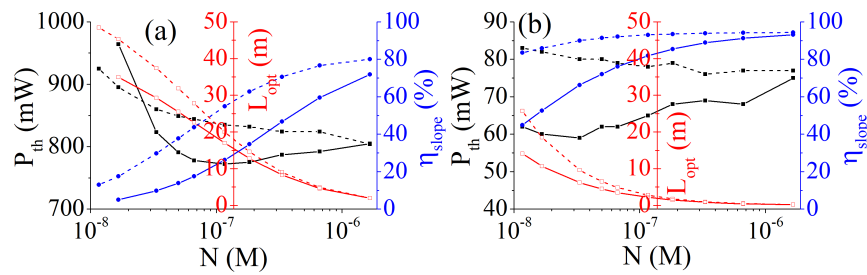


Figure 5.11: Variation of P_{th} , L_{opt} and η_{slope} with N for $\alpha_s = 0$ (---) and $\alpha_s = 2 \times 10^{-4} \text{ cm}^{-1}$ (—) in (a) double-cladding and (b) single-cladding HCF dye laser.

On the other hand, double-cladding HCF dye laser reaches P_{th} and η_{slope} values of $\sim 800 \text{ mW}$ and $> 60\%$ for $L_{opt} \sim 5 \text{ m}$ and $N \sim 1 \mu\text{M}$. As it is shown in the following section, these are still quite respectable performance parameters when dye

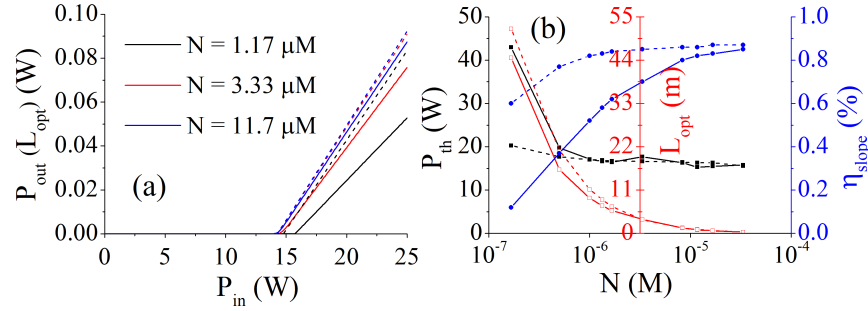


Figure 5.12: (a) Variation of $P_{out}(L_{opt})$ with P_{in} at different N for $\alpha_s = 0$ (---) or $\alpha_s = 2 \times 10^{-4} \text{ cm}^{-1}$ (—) in double-cladding SCF dye laser. (b) Variation of P_{th} , L_{opt} and η_{slope} with N for $\alpha_s = 0$ (---) and $\alpha_s = 2 \times 10^{-4} \text{ cm}^{-1}$ (—) in double-cladding SCF dye laser.

jet lasers are considered. It is notable that for some configurations of fiber dye lasers studied in Fig. 5.11, the value of P_{th} for $\alpha_s = 0$ is higher than P_{th} of a laser with finite scattering losses and the same value of N . This seemingly counterintuitive result is due to different values of L_{opt} that are obtained for different α_s with the optimization procedure described in Sec. 5.2.2. In general, smaller α_s is associated with a larger L_{opt} , which in turn requires a higher pump power for creating threshold population inversion along the fiber length.

5.3 Modeling of Conventional Dye Jet Lasers

Dye jet lasers involve continuous flow of a dye solution through a narrow nozzle forming a jet of liquid gain medium. This liquid jet then passes through the common focal point of the pump and signal laser beams with the focal-point diameters ω_{p0}, ω_{s0} , respectively [Drexhage et al., 1973]. Pike developed analytical expressions for calculating the threshold pump power and the slope efficiency of such dye jet lasers [Pike, 1971]. Within Pike's formalism, the threshold pump power P_{th} is given as:

$$P_{th} = (T + L_c)B, \quad (5.6)$$

where T is the useful single-pass loss of the cavity due to the output coupler transmission [$T = (-\ln R_2)/2$], L_c is the non-useful single-pass loss of the cavity related to absorption and scattering, and $B = [(1 + \varrho)b_p hc]/[4\sigma_{as}\tau(1 - e^{-N\sigma_{ap}d})]$. In the expression for B , ϱ is the beam diameter ratio (also known as the mode match parameter) defined as $\varrho = \omega_{p0}^2/\omega_{s0}^2$, d is the length of the path traversed by the pump and signal laser beams within the gain medium, and b_p is the confocal parameter (or depth of focus) of the pump beam which is equal to the distance between the two end points of the Rayleigh range, i.e $b_p = 2z_{R,p} = (2\pi\omega_{p0}^2)/\lambda_p$. The output signal power can be then expressed as [Schrdoer et al., 1977]:

$$P_{out} = \frac{TA(P_{in} - P_{th})}{T + L_c}, \quad (5.7)$$

where $A = [(1 - e^{-N\sigma_{ap}d})\varrho]/\sqrt{1 + \varrho^2}$. The maximum output power that is available from the laser at a given pump power, P_{in} , is obtained at the optimum value of useful cavity losses T_{opt} that maximizes Eq. (5.7). The resultant T_{opt} and η_{slope} at T_{opt} are given as:

$$T_{opt} = L_c \left(\sqrt{\frac{P_{in}}{BL_c}} - 1 \right), \quad (5.8)$$

$$\eta_{slope} = \frac{dP_{out}}{dP_{in}} = \frac{AT_{opt}}{T_{opt} + L_c}. \quad (5.9)$$

In dye jet lasers, T_{opt} is a parameter analogous to L_{opt} in fiber dye lasers and it characterizes the system performance. Using the parameters of Rhodamine B dye listed in Table 5.1 and assuming optimum transmission $T = T_{opt}$ of the output coupler at each studied configuration, we calculated P_{th} and η_{slope} for typical operating parameters of a dye jet laser ($d = 0.2$ cm, $\omega_{p0} = 20$ μ m, $L_c = 4\%$) [Frolich et al., 1976]. Concentration dependences of T_{opt} , P_{th} , and η_{slope} are plotted in Fig. 5.13 for different values of ϱ . In calculating the values presented in Fig. 5.13, T_{opt} was determined at each N and ϱ using Eq. (5.8) and assuming $P_{in} = 1$ W, which represents typical pumping conditions above threshold. Subsequently, P_{th} , and η_{slope} were found from Eqs. (5.6) and (5.9), respectively.

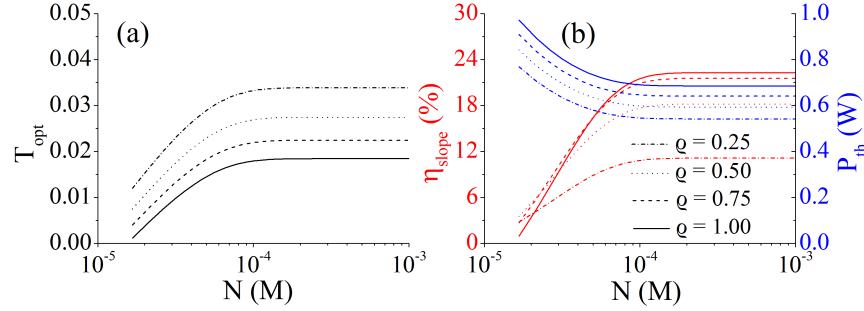


Figure 5.13: Dye jet laser characteristics as a function of N for different values of ρ . (a) T_{opt} (b) η_{slope} (left ordinate) and P_{th} (right ordinate).

For small values of N , the absolute population inversion - and, consequently, the optical gain at a given signal intensity - is low [Drexhage et al., 1973]. The steady-state operation of the laser requires corresponding lowering of the overall losses of the cavity. Thus, for optimal performance, the reflectivity of the output coupler has to be increased, resulting in smaller T_{opt} . Smaller T_{opt} also leads to a smaller η_{slope} , as dictated by Eq. (5.9). When N is increased, P_{th} decreases and η_{slope} increases in accordance with Eqs. (5.6) and (5.9), respectively. For the dye concentration varying from 20 μM to 1 mM, P_{th} is observed to change between 1 W and 541 mW for different values of ρ . This range of P_{th} of a typical dye jet laser is significantly better than that of the double-cladding SCF laser (15.3 – 43 W), comparable to that of the double-cladding HCF laser (772 – 964 mW), and significantly worse than that of the single-cladding HCF laser (59 – 83 mW). Maximal η_{slope} calculated for the dye jet laser is 22%. This value is much higher than the maximum calculated for the SCF laser ($\eta_{slope} = 0.9\%$), but significantly lower than the maximal efficiencies of both double-cladding and single-cladding HCF lasers ($\eta_{slope} = 80\%$ and $\eta_{slope} = 94\%$, respectively). From Fig. 5.13, it is evident that saturation is observed in both P_{th} and η_{slope} beyond $N \simeq 0.12$ mM. Thus, from the practical point of view, it is not advantageous to operate dye jet lasers too high above this saturation concentration.

Chapter 6

CONCLUSION AND OUTLOOK

In chapter 2, polymeric surfaces with wetting properties that can be repeatedly switched from superhydrophobic to superhydrophilic, using fairly simple processes of plasma oxidation and thermal annealing were demonstrated. For this purpose, four polymer systems with inherently quite different surface properties; in particular, hydrophilic PMMA, hydrophobic TPSC and their superhydrophobic versions obtained by incorporation of hydrophobic fumed silica into the polymer matrix are reported. For all studied polymer systems, reversible switching of surface wettability over many cycles of surface treatment is observed. By determining optimum parameters for oxygen plasma exposure and thermal treatment, the efficiency of the process in terms of speed of surface recovery, contrast of water contact angle (CA) between the two extremal wetting states, and number of useful recovery cycles are optimized. A comprehensive physical and chemical characterizations of the studied polymer surfaces are carried out in order to understand the principal phenomena taking place at the surfaces. Characterization results clearly show that reversible switching of wetting characteristics took place solely due to chemical modification of polymer surfaces without any topographical alteration or deterioration. Using the above described simple processes for surface switching and a PDMS mask, patterning of hydrophilic water channels on hydrophobic TPSC films by localized plasma oxidation is achieved. The channels could be erased by thermal annealing of the patterned sample in an oven at 100°C for 20 *min* and could be successfully rewritten multiple times along an arbitrary direction, without any degradation of wetting contrast. Such reconfigurable and patternable surfaces hold promise for applications in surface microfluidics, droplet

microfluidics and optofluidics, in which chemical or biological reagents encapsulated in droplets or even light confined in a liquid can be guided with ease and flexibility.

In chapter 3, a comprehensive study of guiding of emulsion microdroplets along surface tracks obtained by laser ablation of PDMS films of micrometer thickness deposited on glass slides is demonstrated. These guiding tracks are defined by topography and wettability of the patterned surface. The stability of droplet guiding for different polar liquids with different interfacial properties with respect to the host liquid formed by olive oil is analyzed. Experiments with water/SDS droplets moving along $1.0\ \mu\text{m}$, $1.5\ \mu\text{m}$, and $2.0\ \mu\text{m}$ deep guiding tracks revealed no guiding, partial guiding, and complete guiding, respectively, in the three considered cases. These experiments show that for constant chemical properties of the surface, surface topography plays an important role in the stability of droplet guiding, especially for track depths larger than $2\ \mu\text{m}$. Experimental results have been verified by numerical simulations showing the presence and absence of guiding of water/SDS droplets along $2\ \mu\text{m}$ and $1\ \mu\text{m}$ deep tracks, respectively. Experiments with guiding of water/SDS droplets along tracks of different depths indicate that large droplets (diameters larger than $\sim 100\ \mu\text{m}$) display the highest sensitivity of the confinement – characterized by the distance of the guided droplet center from the track center – to the depth of the guiding track. This is a direct result of the capacity of these bigger droplets to interact physically with both sides of the track and benefit from additional surface support. With increasing depth of the track, the differences in confinement of droplets of different sizes become more pronounced. This size dependence of the droplet confinement can be potentially used for sorting droplets with different sizes.

Analysis of guiding of droplets of pure water, pure ethylene glycol, water/SDS and ethylene glycol/SDS mixtures along a $1\ \mu\text{m}$ deep guiding track indicates complete guiding for water, ethylene glycol and ethylene glycol/SDS cases and no guiding for water/SDS case. Guiding of water, ethylene glycol and ethylene glycol/SDS droplets is ensured by their low CAs on the glass surface immersed in oil (close to 50°).

In contrast, water/SDS droplets exhibit higher CA on glass in oil (more than 110°) which prevents their efficient guiding. These experiments show that, for the shallowest guiding track of $1\ \mu\text{m}$ depth, modification of the interfacial interaction energy rather than the topographical step on the surface is the main mechanism responsible for droplet guiding. This dependence of guiding stability on the interfacial energy can be potentially used for droplet sorting according to their surface energy. For the droplets of pure water and pure ethylene glycol moving along a $1\ \mu\text{m}$ deep track, numerical simulations have revealed stronger confinement than observed experimentally. This difference is attributed to the residual PDMS remaining on the track surface after laser ablation which results in a decreased wettability of the guiding track by polar liquids in the experiments.

The presented novel technique for surface-assisted droplet guiding along laser ablated tracks is exploited for passive sorting of microdroplet mixtures in chapter 4. The droplets flowing in the same microfluidic chip are sorted based on their inherent wetting properties and IFT. A theoretical model is also developed incorporating fundamental equations of drag, frictional and trapping forces acting on a droplet which exhibits good agreement with experiments performed with water and water/SDS droplets at different speeds and track angles. Sorting of water and water/SDS droplets of similar sizes that are generated by two different T-junctions in the same microfluidic chip is also demonstrated. The presented approach can be used to design custom passive microfluidic devices to guide and sort droplets without extensive fine tuning of experimental protocols. This study also paves the way for autonomous solutions for integrated lab-on-a-chip biological screening, therapeutic agent delivery, diagnostic chips, drug discovery and isolation of dissolved chemical compounds. Substrate surfaces and tracks of materials with tunable wettability can be modeled with a high precision, quick response and at a reduced computation/memory cost. The fact that the droplet guiding can be achieved purely on the basis of surface energy modifications can also inspire other droplet guiding schemes that would enable defining

reconfigurable tracks by surface wetting modifications obtained using other external control mechanisms such as electric field [Mannetje et al., 2014] or light [Lim et al., 2006b].

In chapter 5, optofluidic dye lasers based on holey fibers and investigated their potential for complementing or replacing dye jet lasers in high-power applications are introduced. A mathematical model of such fiber laser systems using coupled steady-state rate equations is developed and solved to determine the laser performance characteristics under various operating conditions. In this parametric study, three different fiber laser geometries with different mode areas and pump/signal filling factors are considered, in particular, double-cladding SCF laser, double-cladding HCF laser, and single-cladding HCF laser. For benchmarking purposes, the results are compared with the performance characteristics of dye jet lasers.

Among the studied fiber dye laser geometries and the dye jet laser, the single-cladding HCF laser has been found to perform the best in terms of low P_{th} and high η_{slope} . This is mainly due to the large pump and signal filling factors in this arrangement that allow for efficient collection and transport of light within the active gain medium. Double-cladding HCF laser has been found to perform comparably to the dye jet laser when the pump filling factor is similar to or larger than the value of $\Gamma_p = 0.02$ assumed in the paper. Taking into account better thermal management and ease of coupling of the pump beam into the fiber, double-cladding HCF laser has the potential to be the most practical geometry for holey fiber dye lasers. Double-cladding SCF geometry has been found to be highly inefficient, with $P_{th} > 10$ W and $\eta_{slope} < 1\%$, caused mostly by the extremely small value of Γ_s that results from evanescent coupling of the signal light to the guided mode of the fiber. For a given dye concentration, N , there is an optimum fiber length, L_{opt} , that maximizes the output power of the holey fiber dye laser. The analysis shows that good operating parameters for double-cladding and single-cladding HCF lasers are $N \sim 1 \mu\text{M}$, $L_{opt} \sim 4.7$ m and $N \sim 1 \mu\text{M}$, $L_{opt} \sim 0.45$ m, respectively. Optimum operating conditions of the

proposed optofluidic lasers have been determined considering realistic parameters. Practical holey fiber dye lasers that can serve as fiber-based alternatives of conventional dye jet lasers as well as novel biological/chemical sensors and bio-lasers can be designed using the presented framework. Natural extension of this work will incorporate thermal effects and dye photobleaching into the analysis of laser performance. This way, holey fiber dimensions including the fiber length and the cross-section of the liquid-filled channel can be further optimized and optimal flow speed of the dye solution through the fiber can be determined.

Chapter 7

APPENDIX

7.1 Droplet Tracking Algorithm

```
clear all;
clc;
close all;
close variables;
[ sFileName, sPathName] = uigetfile('Video path/*.mp4', ...
'Select experimental video for droplet position tracking:');
% read video file into Matlab
objExperimentalVideo = VideoReader(strcat(sPathName,sFileName));
% determine number of frames in the video file and frame rate
vNumOfFrames = objExperimentalVideo.NumberOfFrames;
vFrameRate = objExperimentalVideo.FrameRate;
wImage_Template_Whole = double(rgb2gray(read(objExperimentalVideo,1)));
hDropletImageHandle = figure;
set(hDropletImageHandle, 'OuterPosition', [50, 50, 400, 400], ...
'NumberTitle','off','Name', 'Select image region containing tracked
droplet');
image(wImage_Template_Whole);
colormap(gray(256));
axis image;
xlabel('X-position (pixels)','FontWeight','bold');
ylabel('Y-position (pixels)','FontWeight','bold');
```

% Subsequently, user is prompted to select image region containing the target droplet. "ginput" function is used to select corner points of a rectangular region by pointing and clicking the mouse twice.

NOTE: x-position corresponds to image columns, y-position corresponds to image rows.

```
wDropletRegionSelection = ginput(2);
vXmin = min(floor(wDropletRegionSelection(1)), ...
floor(wDropletRegionSelection(2))); %xmin
vXmax = max(ceil(wDropletRegionSelection(1)), ...,
ceil(wDropletRegionSelection(2))); %xmax
vYmin = min(floor(wDropletRegionSelection(3)), ...
floor(wDropletRegionSelection(4))); %ymin
vYmax = max(ceil(wDropletRegionSelection(3)), ...
ceil(wDropletRegionSelection(4))); %ymax
% Make sure dimensions of the template image (vXmax-vXmin+1) and ...
(vYmax-vYmin+1) are even numbers
if (((vXmax - vXmin)/2) == round((vXmax - vXmin)/2))
vXmin = vXmin + 1;
end
if (((vYmax-vYmin)/2) == round((vYmax-vYmin)/2))
vYmin = vYmin + 1;
end
% Display selected image region containing tracked droplet.
NOTE: x-position corresponds to image columns, y-position corresponds
to image rows.
wImage_Template = wImage_Template_Whole(vYmin:vYmax,vXmin:vXmax));
set(hDropletImageHandle, 'NumberTitle','off','Name', 'Tracked droplet
image');
```

```

image(wImage_Template);
colormap(gray(256));
axis image;
xlabel('X-position (pixels)','FontWeight','bold');
ylabel('Y-position (pixels)','FontWeight','bold');
% Display width and height of the droplet template image
vTargetWidth = size(wImage_Template,2);
% X-direction -> number of image columns
vTargetHeight = size(wImage_Template,1);
% Y-direction -> number of image rows
disp(strcat('Target image width: ', num2str(vTargetWidth)));
disp(strcat('Target image height: ', num2str(vTargetHeight)));
% change the type of image data to 'double' for further correlation
analysis
wImage_Template = double(wImage_Template_Whole(vYmin:vYmax,vXmin:vXmax));
% subtract background
wImage_Template = wImage_Template - (round(mean(mean(wImage_Template))));
% decide if image correlation results will be stored or not
vStoreCorrelationResults = 1;
% create folder for storing the results of image correlation analysis
if ((~isdir(strcat(sPathName,sFileName(1:length(sFileName)-4), ...
'_CA')))) && vStoreCorrelationResults)
mkdir(strcat(sPathName,sFileName(1:length(sFileName)-4),'_CA'));
end
% preallocate matrices for the droplet position data
% x-direction:  image columns
% y-direction:  image rows
wX_Track = zeros(1,vNumOfFrames);

```

```
wY_Track = zeros(1,vNumOfFrames);

% half-width of the region centered on the maximum of image correlation
% function which is used in fitting the correlation function with a
2-D Gaussian
vNumPoints = 20;

h = waitbar(0, strcat('Processing video file: ', sFileName));
tic

% create video file for storing the results of droplet position tracking
% -> in this video, target droplet appears marked with a cross
vOutputVideoFile = VideoWriter(strcat(sFileName ...
(1:length(sFileName)-4), '_Track'), 'MPEG-4');
open(vOutputVideoFile)

% actual tracking of the droplet position in individual video frames
for vCounter = 1:1:vNumOfFrames
% read image frame from the video file
wActual_Image = double(rgb2gray(read(objExperimentalVideo, vCounter)));
% subtract background
vImageOffset = round(mean(mean(wActual_Image)));
wActual_Image = wActual_Image - vImageOffset;
% calculate 2-D correlation between template image and actual image
frame
wCorrelation = normxcorr2(wImage_Template, wActual_Image);
% normalize calculated 2-D correlation to unity
wCorrelation = wCorrelation/max(max(wCorrelation));
% precise determination of the location of maximal correlation between
template image and actual image frame to avoid problems with multiple
droplets present simultaneoulsy in the field of view maximum of image
cross-correlation is only searched for within the region where the droplet
```

was located in the previous frame; for the first frame in the movie, search is carried out within the original user-selected region, search region has to be shifted by $[vTargetHeight/2, vTargetWidth/2]$ to account for image padding added by the correlation operation.

NOTE: x-position corresponds to image columns, y-position corresponds to image rows.

```
% find maximal cross-correlation value within the target region.
vTargetMaximalCorr = max(max(wCorrelation((vYmin + ...
vTargetHeight/2):(vYmax + vTargetHeight/2), (vXmin + ...
vTargetWidth/2):(vXmax + vTargetWidth/2))));
% find coordinates of the cross-correlation image pixel whose grayscale
% value is equal to the above found maximum
% y-position of the correlation peak corresponds to row index (first
parameter)
% x-position of the correlation peak corresponds to column index (second
parameter)
[wY_MaxCorr, wX_MaxCorr] = find(wCorrelation == vTargetMaximalCorr);
% region of the calculated image cross-correlation data which is used
in the actual 2-D Gaussian fitting to the cross-correlation peak
wFitCorrelation = wCorrelation(wY_MaxCorr-vNumPoints: ...
wY_MaxCorr+vNumPoints, wX_MaxCorr-vNumPoints:wX_MaxCorr+vNumPoints);
% starting guess for 2-D Gaussian fitting
% Gaussian offset along the z-axis
wStartingGuess(1) = 0;
% Gaussian amplitude -> cross-correlation is normalized to unity
wStartingGuess(2) = 1;
% x-coordinate of Gaussian center -> should be around the center of
the region used for fitting
```

```

wStartingGuess(3) = vNumPoints+1;

% y-coordinate of Gaussian center -> should be around the center of
the region used for fitting
wStartingGuess(4) = vNumPoints+1;

% Gaussian width
wStartingGuess(5) = 5;

% set options for the function minimalization
vOptions = optimset('MaxFunEvals',10000, ...
'MaxIter', 10000, 'TolFun',1e-3, 'Display', 'off');

% actual fitting of the 2-D Gaussian function
wFittedValues = fminsearch(@(wX) f2D_Gaussian(wX,wFitCorrelation), ...
wStartingGuess,vOptions);

% fit results for 2-D Gaussian fitting
VX_Peak = wFittedValues(3);

% column index
vY_Peak = wFittedValues(4);

% row index

% Determination of X and Y positions of the tracked object in the
original image since the analysis of image cross-correlation only
takes place within a small region in the vicinity of the cross
correlation maximum, fitted peak position [vX_Peak, vY_Peak] of the
cross-correlation maximum has to be shifted by [(wX_MaxCorr -
vNumPoints - 1), (wY_MaxCorr - vNumPoints - 1)] to give the peak
position with respect to the origin of the full image cross
correlation matrix due to image padding introduced by correlation
operation, coordinates need to be further shifted down by half of
the template image dimensions.

wX_Track(vCounter)=(wX_MaxCorr-vNumPoints-1)+vX_Peak-vTargetWidth/2;

```

```

wY_Track(vCounter)=(wY_MaxCorr-vNumPoints-1)+vY_Peak-TargetHeight/2;

% update position of the region where the maximum of image
% cross-correlation will be searched for in the next frame;
% this region is centered on the location of the particle in the
current frame

vXmin = round(wX_Track(vCounter)) - vTargetWidth/2;
vXmax = round(wX_Track(vCounter)) + vTargetWidth/2;
vYmin = round(wY_Track(vCounter)) - vTargetHeight/2;
vYmax = round(wY_Track(vCounter)) + vTargetHeight/2;

% store results of image correlation analysis in a dedicated folder
if (vStoreCorrelationResults)

% create correct file name for storing results of image correlation
analysis

if (vCounter < 10)

sOutFileName = strcat(sPathName,sFileName(1:length(sFileName)-4), ...
'_CA/Position_000',num2str(vCounter),'.jpg');

sOutFileName_CC = strcat(sPathName,sFileName(1:length(sFileName) ...
-4), '_CA/Position_CC_000',num2str(vCounter),'.jpg');

elseif (vCounter < 100)

sOutFileName = strcat(sPathName,sFileName(1:length(sFileName)-4), ...
'_CA/Position_00',num2str(vCounter),'.jpg');

sOutFileName_CC = strcat(sPathName,sFileName(1:length(sFileName) ...
-4), '_CA/Position_CC_00',num2str(vCounter),'.jpg');

elseif (vCounter < 1000)

sOutFileName = strcat(sPathName,sFileName(1:length(sFileName)-4), ...
'_CA/Position_0',num2str(vCounter),'.jpg');

sOutFileName_CC = strcat(sPathName,sFileName(1:length(sFileName) ...
-4), '_CA/Position_CC_0',num2str(vCounter),'.jpg');

```

```

else
    sOutFileName = strcat(sPathName,sFileName(1:length(sFileName)-4), ...
        '_CA/Position_', num2str(vCounter), '.jpg');
    sOutFileName_CC = strcat(sPathName,sFileName(1:length(sFileName) ...
        -4), '_CA/Position_CC_', num2str(vCounter), '.jpg');
end

% shift the actual image back to the original grayscale level
wActual_Image = uint8(wActual_Image + vImageOffset);

% add white cross at the location of the tracked droplet center in the
actual image
wActual_Image(round(wY_Track(vCounter))-6:round( ...
wY_Track(vCounter))+6, round(wX_Track(vCounter))) = 255;
wActual_Image(round(wY_Track(vCounter)), ...
round(wX_Track(vCounter))-6:round(wX_Track(vCounter))+6) = 255;

% save actual image with labeled droplet center
% imwrite(wActual_Image,sOutFileName,'jpeg')
% imwrite(wCorrelation((vY_Center-wROI_Size):(vY_Center+wROI_Size),
% (vX_Center-wROI_Size):
(vX_Center+wROI_Size)),sOutFileName,'jpeg');
% wCorrelation(round(wY_Track(vCounter)), ...
round(wX_Track(vCounter))) = 0;

% imwrite(wCorrelation,sOutFileName_CC,'jpeg');
% imwrite(wFitCorrelation,sOutFileName,'jpeg');
writeVideo(vOutputVideoFile,wActual_Image);
end

waitbar((vCounter/vNumOfFrames),h);
end

close(vOutputVideoFile);

```

```

close(h)

toc

% plot the results of droplet position tracking analysis
% generate scaled time axis for the input video file
wTime = (1:1:length(wY_Track))/vFrameRate;

% droplet position plotting
hPositionPlotHandle = figure;
set(hPositionPlotHandle, 'OuterPosition', [450, 50, 400, 400], ...
    'NumberTitle','off', 'Name', 'Droplet position tracks');
subplot(2,1,1)
plot(wTime,wX_Track)
title(strcat('Input video file:',sFileName), 'FontWeight', 'bold', ...
    'Interpreter', 'none');
axis tight
xlabel('Time (seconds)', 'FontWeight', 'bold')
ylabel('X-position ( $\mu m$ )', 'FontWeight', 'bold')
subplot(2,1,2)
plot(wTime,wY_Track)
axis tight
xlabel('Time (seconds)', 'FontWeight', 'bold')
ylabel('Y-position ( $\mu m$ )', 'FontWeight', 'bold')

% calculate velocity of the tracked droplet using droplet position track
% and known frame rate of the experimental video file.
wX_Velocity = diff(wX_Track)*vFrameRate;
wY_Velocity = diff(wY_Track)*vFrameRate;
p_factor=800/142;
Size(1:length(wY_Track))=(vXmax-vXmin)*p_factor;
Velocity(1:length(wY_Track))=p_factor*sqrt((mean(wX_Velocity))^2+ ...

```

```

(mean(wY_Velocity))^2);
w_Velocity = p_factor*sqrt(wX_Velocity.^2 + wY_Velocity.^2);
display(Velocity);
Velocity(1:length(wY_Track))=Velocity;
height(1:length(wY_Track)) = (wY_Track(1)-min(wY_Track))*p_factor;
% save x and y positions of the tracked droplet
sOutFile = strcat(sPathName, sFileName(1:length(sFileName)-4), ...
'_Position.txt');
wOutData = [(wX_Track)' (wY_Track)' Velocity' height'];
save(sOutFile,'wOutData','-ASCII','-TABS');
% droplet velocity plotting
hVelocityPlotHandle = figure;
set(hVelocityPlotHandle, 'OuterPosition', [850, 50, 400, 400], ...
'NumberTitle','off', 'Name', 'Droplet velocities');
subplot(2,1,1)
plot(wTime(1:length(wTime)-1),wX_Velocity);
title(strcat('Input video file:',sFileName), 'FontWeight', 'bold', ...
'Interpreter', 'none');
axis tight;
xlabel('Time (seconds)','FontWeight','bold');
ylabel('X-velocity ( $\mu\text{m/s}$ )','FontWeight','bold');
subplot(2,1,2);
plot(wTime(1:length(wTime)-1),wY_Velocity);
axis tight;
xlabel('Time (seconds)','FontWeight','bold');
ylabel('Y-velocity ( $\mu\text{m/s}$ )','FontWeight','bold');
figure;
image(wImage_Template_Whole);

```



```
colormap(gray(256));  
axis image;  
hold on;  
plot(wOutData(:,1),wOutData(:,2),'g');  
fname = 'Path to store image results/images';  
% text(2,8,'A Simple Plot','Color','red','FontSize',14)  
dim = [.2 .5 .3 .3];  
str = ['Height = ' num2str(height(1)) '  $\mu\text{m}$  , ...  
Speed = ' num2str(Velocity(1)) '  $\mu\text{m}/\text{sec}$ '];  
annotation('textbox',dim,'String',str,'FitBoxToText','on');  
saveas(gca, fullfile(fname, sFileName(1:length(sFileName)-4)), 'fig');
```

BIBLIOGRAPHY

- [NKT,] NKT Photonics. Brochure.
- [Ans, 2013] (2013). *Ansys Fluent Theory Guide*, volume 15.0.
- [Aas et al., 2016] Aas, M., Chen, Q., Jonas, A., Kiraz, A., , and Fan, X. (2016). Optofluidic fret lasers and their applications in novel photonic devices and biochemical sensing. *IEEE J. Sel. Top. Quantum Electron.*, 22(4).
- [Aas et al., 2013] Aas, M., Jonáš, A., Kiraz, A., Brzobohatý, O., Ježek, J., Pilát, Z., and Zemánek, P. (2013). Spectral tuning of lasing emission from optofluidic droplet microlasers using optical stretching. *Optics Express*, 21(18):21380–21394.
- [Abate et al., 2010] Abate, A. R., Agresti, J. J., and Weitz, D. A. (2010). Microfluidic sorting with high-speed single-layer membrane valves. *Appl. Phys. Lett.*, 96(20):203509.
- [Abbyad et al., 2010a] Abbyad, P., Dangla, R., Alexandrou, A., and Baroud, C. N. (2010a). Rails and anchors: guiding and trapping droplet microreactors in two dimensions. *Lab Chip*, 115(5):813–821.
- [Abbyad et al., 2010b] Abbyad, P., Tharaux, P. L., Martin, J. L., Baroud, C. N., and Alexandrou, A. (2010b). Sickling of red blood cells through rapid oxygen exchange in microfluidic drops. *Lab Chip*, 10(19):2505–2512.
- [Acatay et al., 2004] Acatay, K., Simsek, E., Ow-Yang, C., and Menciloglu, Y. Z. (2004). Tunable, superhydrophobically stable polymeric surfaces by electrospinning. *Angew Chem Int Ed Engl.*, 299(5611):5210–5213.

- [Agarwal, 2001] Agarwal, G. P. (2001). *Nonlinear fiber optics*. Elsevier, Amsterdam Netherlands, third edition.
- [Ahn and Kerbage, 2005] Ahn, K. and Kerbage, C. (2005). Dielectrophoretic manipulation of drops for high-speed microfluidic sorting devices. *Appl. Phys. Lett.*, 88(2):24104.
- [Ahn et al., 2006] Ahn, K., Kerbage, C., Hunt, T. P., Westervelt, R. M., Link, D. R., and Weitz, D. A. (2006). Dielectrophoretic manipulation of drops for high-speed microfluidic sorting devices. *Lab Chip*, 88(2):241041–241043.
- [Aubry et al., 2011] Aubry, G., Kou, Q., Soto-Velasco, J., Wang, C., Meance, S., He, J. J., and Haghiri-Gosnet, A. M. (2011). A multicolor microfluidic droplet dye laser with single mode emission. *Appl Phys Lett*, 98(11):111111.
- [Bakal et al., 2015] Bakal, A., Vannahme, C., Kristensen, A., and Levy, U. (2015). Tunable on chip optofluidic laser. *Appl Phys Lett*, 107(21):211105.
- [Baroud, 2014] Baroud, C. N. (2014). Droplet microfluidics in two dimensional channels. In Kohler, J. M. and Cahill, B. P., editors, *Micro-Segmented Flow, Applications in Chemistry and Biology*, chapter 2, pages 7–29. Springer-Verlag Berlin Heidelberg, New York.
- [Beatus et al., 2012] Beatus, T., Bar-Ziv, R. H., and Tlusty, T. (2012). The physics of 2d microfluidic droplet ensembles. *Physics Reports*, 516(3):103–145.
- [Broeng et al., 1999] Broeng, J., Mogilevstev, D., Barkou, S. E., and Bjarklev, A. (1999). Photonic crystal fibers: A new class of optical waveguides. *Optical Fiber Technology*, 5(3):305–330.

- [Chen et al., 2013] Chen, Q., Liu, H., Lee, W., Sun, Y., Zhu, D., Pei, H., Fan, C., and Fan, X. (2013). Self-assembled dna tetrahedral optofluidic lasers with precise and tunable gain control. *Lab Chip*, 13(17):3351–3354.
- [Chetouani et al., 2006] Chetouani, H., Jeandey, C., Haguet, V., Rostaing, H., Dieppedale, C., and Reyne, G. (2006). Diamagnetic levitation with permanent magnets for contactless guiding and trapping of microdroplets and particles in air and liquids. *IEEE Transactions on Magnetics*, 42(10):3557–3559.
- [Choi and Son, 2008] Choi, J. and Son, G. (2008). Numerical study of droplet motion in a microchannel with different contact angles. *Journal of Mechanical Science and Engineering*, 22(12):2590–2599.
- [Cookey et al., 2015] Cookey, G. A., Obunwo, C. C., and O.Uzoma, D. (2015). The effect of temperature on the micellization of an anionic surfactant in mixed solvent systems. *IOSR Journal of Applied Chemistry*, 8(12):49–54.
- [Cubillas et al., 2013] Cubillas, A. M., Unterkofler, S., Euser, T. G., Etzold, B. J. M., Jones, A. C., Sadler, P. J., Wasserscheid, P., and Russell, P. S. (2013). Photonic crystal fibres for chemical sensing and photochemistry. *Chem. Soc. Rev.*, 42(22):8629–8648.
- [Dangla et al., 2011] Dangla, R., Lee, S., and Baroud, C. N. (2011). Trapping microfluidic drops in wells of surface energy. *Phys. Rev. Lett.*, 107(12):12450.
- [Dangla et al., 2014] Dangla, R., Lee, S., and Baroud, C. N. (2014). Trapping microfluidic drops in wells of surface energy. *Physical Review Letters*, 107(12):124501–1–124501–4.
- [Davydov et al., 1963] Davydov, V. Y., Kiselev, A. V., and Zhuravlev, L. T. (1963).

- Study of the surface and bulk hydroxyl groups of silica by infra-red spectra and d2o-exchange. *Trans. Faraday Soc.*, 60:2254–2264.
- [de Ruiter et al., 2014] de Ruiter, R., Pit, A. M., de Oliveira, V. M., Duits, M. H. G., van den Ende, D., and Mugele, F. (2014). Electrostatic potential wells for on-demand drop manipulation in microchannels. *Lab Chip*, 14(5):883–891.
- [Drexhage et al., 1973] Drexhage, K. H., Hansch, T. W., Ippen, E. P., Schafer, F. P., Shank, C. V., and Snively, B. B. (1973). *Dye Lasers*. Springer-Verlag, Heidelberg, Germany, first edition.
- [Duarte, 1991] Duarte, F. J. (1991). *High Power Dye Lasers*, volume 65. Springer-Verlag, Berlin, Germany.
- [Erbil et al., 2003] Erbil, H. Y., Demirel, A. L., Avci, Y., and Mert, O. (2003). Transformation of a simple plastic into a superhydrophobic surface. *Science*, 299(5611):1377–1380.
- [Erickson et al., 2011] Erickson, D., Sinton, D., and Psaltis, D. (2011). Optofluidics for energy applications. *Nature Photonics*, 5:583–590.
- [Ertman et al., 2017] Ertman, S., Lesiak, P., and Wolinski, T. R. (2017). Optofluidic photonic crystal fiber-based sensors. *J. Light. Technol.*, 35(16):3399–3405.
- [Fan and White, 2011] Fan, X. and White, I. M. (2011). Optofluidic microsystems for chemical and biological analysis. *Nature Photonics*, 5:591–597.
- [Fan and Yun, 2014] Fan, X. and Yun, S. H. (2014). The potential of optofluidic biolasers. *Nat Methods*, 11(2):141–147.
- [Fei et al., 2011] Fei, P., He, Z., Zheng, C., Chen, T., Men, Y., and Huang, Y. (2011). Discretely tunable optofluidic compound microlenses. *Lab Chip*, 11(17):2835–2841.

- [Fradet et al., 2011] Fradet, E., McDougall, C., Abbyad, P., Dangla, R., McGloin, D., and Baroud, C. N. (2011). Combining rails and anchors with laser forcing for selective manipulation within 2d droplet arrays. *Lab Chip*, 11(24):4228–4234.
- [Franczyk et al., 2014] Franczyk, M., Stepień, R., Pysz, D., Kujawa, I., and Buczynski, R. (2014). Phosphate Yb^{3+} doped air-cladding photonic crystal fibers for laser applications. *Photonics Letters of Poland*, 6(1):47–49.
- [Franke et al., 2009] Franke, T., Abate, A. R., Weitz, D. A., and Wixforth, A. (2009). Surface acoustic wave (saw) directed droplet flow in microfluidics for pdms devices. *Lab Chip*, 9(18):2625–2627.
- [Frolich et al., 1976] Frolich, D., Stein, L., Schroder, H. W., and Welling, H. (1976). Efficient frequency doubling of cw dye laser radiation. *Applied Physics*, 11(1):97–101.
- [F.Stalder et al., 2010] F.Stalder, A., Melchior, T., Muller, M., Sage, D., Blu, T., and Unser, M. (2010). Low-bond axisymmetric drop shape analysis for surface tension and contact angle measurements of sessile drops. *Colloids Surf. A Physicochem. Eng. Asp.*, 364(1):72–81.
- [Ganesan, 2012] Ganesan, S. (2012). On the dynamic contact angle in simulation of impinging droplets with sharp interface methods. *Microfluidics and Nanofluidics*, 14(3):615–625.
- [Garstecki et al., 2006] Garstecki, P., Fuerstman, M. J., Stone, H. A., and Whitesides, G. M. (2006). Formation of droplets and bubbles in a microfluidic t-junction—scaling and mechanism of break-up. *Lab Chip*, 6(3):437–446.
- [Gather and Yun, 2011] Gather, M. C. and Yun, S. H. (2011). Single-cell biological lasers. *Nature Photonics*, 5:406–410.

- [Gerosa et al., 2015] Gerosa, R. M., Sudirman, A., de S. Menezes, L., Margulis, W., and de Matos, C. J. S. (2015). All-fiber high repetition rate microfluidic dye laser. *Optica*, 2(2):186–193.
- [Gong et al., 2007] Gong, M., Yuan, Y., Li, C., Yan, P., Zhang, H., and Liao, S. (2007). Numerical modeling of transverse mode competition in strongly pumped multimode fiber lasers and amplifiers. *Optics Express*, 15(6):3236–3246.
- [Gong et al., 2015] Gong, Y., Zhang, M., Gong, C., Wu, Y., Rao, Y., and Fan, X. (2015). Sensitive optofluidic flow rate sensor based on laser heating and microring resonator. *Microfluid Nanofluid*, 19(6):1497–1505.
- [Guo et al., 2011] Guo, Z., Liu, W., and Su, B.-L. (2011). Superhydrophobic surfaces: From natural to biomimetic to functional. *J. Colloid Interface Sci.*, 353(2):335–355.
- [Gupta et al., 2009] Gupta, R., Fletcher, D. F., and Haynes, B. S. (2009). On the cfd modelling of taylor flow in microchannels. *Chemical Engineering Science*, 64(12):2941–2950.
- [Han et al., 2005] Han, J. T., Xurong, and Cho, K. (2005). Diverse access to artificial superhydrophobic surfaces using block copolymers. *Langmuir*, 21(15):6662–6665.
- [Herold and Rasooly, 2009] Herold, K. E. and Rasooly, A. (2009). *Lab on a Chip Technology: Fabrication and microfluidics*. Horizon Scientific Press.
- [Hillborg et al., 2004] Hillborg, H., Tomczak, N., Olah, A., Schonherr, H., and Vancso, G. J. (2004). Nanoscale hydrophobic recovery: A chemical force microscopy study of uv/ozone-treated cross-linked poly(dimethylsiloxane). *Langmuir*, 20(3):785–794.

- [Hong and Pan, 2010] Hong, L. and Pan, T. (2010). Surface microfluidics fabricated by photopatternable superhydrophobic nanocomposite. *Microfluid Nanofluid*, 10(991):991–997.
- [Hummer et al., 2016] Hummer, D., Kurth, F., Rainer, N. N., and Dittrich, P. S. (2016). Single cells in confined volumes: microchambers and microdroplets. *Lab Chip*, 16(447):447–458.
- [Jin et al., 2011] Jin, C., Yan, R., and Huang, J. (2011). Cellulose substance with reversible photo-responsive wettability by surface modification. *J. Mater. Chem.*, 21(43):17519–17525.
- [Jonas et al., 2014] Jonas, A., Yalizay, B., Akturk, S., and Kiraz, A. (2014). Free-standing optofluidic waveguides formed on patterned superhydrophobic surfaces. *Appl. Phys. Lett.*, 104(9):0911231–0911234.
- [Jonáš et al., 2014] Jonáš, A., Aas, M., Karadag, Y., Manioglu, S., Anand, S., McGloin, D., Bayraktar, H., and Kiraz, A. (2014). *In vitro* and *in vivo* biolasing of fluorescent proteins suspended in liquid microdroplet cavities. *Lab Chip*, 14(16):3093–3100.
- [Karapetsas et al., 2016] Karapetsas, G., Chamakos, N. T., and Papathanasiou, A. G. (2016). Efficient modelling of droplet dynamics on complex surfaces. *Journal of Physics: Condensed Matter*, 28(8):85101–1–85101–16.
- [Kelson and Hardy, 1999] Kelson, I. and Hardy, A. (1999). Optimization of strongly pumped fiber lasers. *Journal of Lightwave Technology*, 17(5):891–897.
- [Krupenkin et al., 2007] Krupenkin, T. N., Taylor, J. A., Wang, E. N., Kolodner, P., Hodes, M., and Salamon, T. R. (2007). Reversible wetting-dewetting transi-

- tions on electrically tunable superhydrophobic nanostructured surfaces. *Langmuir*, 23(18):9128–9133.
- [Lahoz et al., 2017] Lahoz, F., Martín, I. R., Walo, D., Gil-Rostra, J., Yubero, F., and Gonzalez-Elipe, A. R. (2017). A compact and portable optofluidic device for detection of liquid properties and label-free sensing. *J Phys D: Appl Phys*, 50(21):215103.
- [Latthe et al., 2012] Latthe, S. S., Gurav, A. B., Maruti, C. S., and Vhatkar, R. S. (2012). Recent progress in preparation of superhydrophobic surfaces: A review. *J. of Surf. Eng. Mat. and Adv. Tech.*, 2(2):76–94.
- [Lee et al., 2006] Lee, H., Liu, Y., Westervelt, R. M., and Ham, D. (2006). Ic/microfluidic hybrid system for magnetic manipulation of biological cells. *IEEE Journal of Solid-State Circuits*, 41(6):1471–1480.
- [Levy et al., 2006] Levy, U., Campbell, K., and Groisman, A. (2006). On-chip microfluidic tuning of an optical microring resonator. *Appl. Phys. Lett.*, 88(11):1111071–1111073.
- [Li et al., 2006] Li, Z., Zhang, Z., Emery, T., Scherer, A., and Psaltis, D. (2006). Single mode optofluidic distributed feedback dye laser. *Opt Express*, 14(2):696–701.
- [Lim and Lam, 2014] Lim, C. Y. and Lam, Y. C. (2014). Phase field simulation of impingement and spreading of micro-sized droplet on heterogeneous surface. *Microfluidics and Nanofluidics*, 17(1):131–148.
- [Lim et al., 2006a] Lim, H. S., Han, J. T., Kwak, D., Jin, M., and and Kilwon Cho (2006a). Photoreversibly switchable superhydrophobic surface with erasable and rewritable pattern. *J. Am. Chem. Soc*, 128(45):14458–14459.

- [Lim et al., 2006b] Lim, H. S., Han, J. T., Kwak, D., Jin, M., and Cho, K. (2006b). Photoreversibly switchable superhydrophobic surface with erasable and rewritable pattern. *Journal of American Chemical Society*, 128(45):14458–14459.
- [Liu and Jiang, 2012] Liu, K. and Jiang, L. (2012). Bio-inspired self-cleaning surfaces. *Annu. Rev. Mater. Res.*, 42(2):231–263.
- [Malekzadeh and Roohi, 2015] Malekzadeh, S. and Roohi, E. (2015). Investigation of different droplet formation regimes in a t-junction microchannel using the vof technique in openfoam. *Microgravity Science and Technology*, 27(3):231–243.
- [Mannetje et al., 2014] Mannetje, D., Ghosh, S., Lagraauw, R., Otten, S., Pit, A., Berendsen, C., Zeegers, J., van den Ende, D., and Mugele, F. (2014). Trapping of drops by wetting defects. *Nature Communications*, 5(3559):1–7.
- [Manoudis et al., 2008] Manoudis, P. N., Karapanagiotis, I., Tsakalof, A., Zuburtikudis, I., and Panayiotou, C. (2008). Superhydrophobic composite films produced on various substrates. *Langmuir*, 24(19):11225–11232.
- [Menech et al., 2008] Menech, M. D., Garstecki, P., Jousse, F., and Stone, H. A. (2008). Transition from squeezing to dripping in a microfluidic t-shaped junction. *Journal of Fluid Mechanics*, 595:141–161.
- [Minko et al., 2003] Minko, S., Mueller, M., Motornov, M., Nitschke, M., Grundke, K., and Stamm, M. (2003). Two-level structured self-adaptive surfaces with reversibly tunable properties. *J. Am. Chem. Soc.*, 125(13):3896–3900.
- [Nampoothiri et al., 2015] Nampoothiri, A. V. V., Debord, B., Alharbi, M., Gérôme, F., Benabid, F., and Rudolph, W. (2015). Cw hollow-core optically pumped i2 fiber gas laser. *Optics Letters*, 40(4):605–608.

- [Nampoothiri et al., 2012] Nampoothiri, A. V. V., Jones, A. M., Fourcade-Dutin, C., Mao, C., Dadashzadeh, N., Baumgart, B., Wang, Y., Alharbi, M., Bradley, T., Campbell, N., Benabid, F., Washburn, B. R., Corwin, K. L., and Rudolph, W. (2012). Hollow-core optical fiber gas lasers (hofglas): a review [invited]. *Opt. Mater. Express*, 2(7):948–961.
- [Oner and McCarthy, 2000] Oner, D. and McCarthy, T. J. (2000). Ultrahydrophobic surfaces. effects of topography length scales on wettability. *Langmuir*, 16(20):7777–7782.
- [Peterson et al., 1970] Peterson, O. G., Tuccio, S. A., and Snavely, B. B. (1970). Cw operation of an organic dye solution laser. *Appl Phys Lett*, 17(6):245–247.
- [Petroffe et al., 2015] Petroffe, G., Wang, C., Sallenave, X., Sini, G., Goubarda, F., and Peralta, S. (2015). Fast and reversible photo-responsive wettability on tio2 based hybrid surfaces. *J. Mater. Chem. A*, 3(21):11533–11542.
- [Pike, 1971] Pike, H. A. (1971). *Organic Dye Lasers*. PhD thesis, University of Rochester.
- [Pit et al., 2016] Pit, A. M., Bonestroo, S., Wijnperle, D., Duits, M. H. G., and Mugele, F. (2016). Electrode-assisted trapping and release of droplets on hydrophilic patches in a hydrophobic microchannel. *Microfluid Nanofluid*, 20(123):1–12.
- [Pit et al., 2015] Pit, A. M., Duits, M. H. G., and Mugele, F. (2015). Droplet manipulations in two phase flow microfluidics. *Micromachines*, 6(11):1768–1793.
- [Rakszewska et al., 2014] Rakszewska, A., Tel, J., Chokkalingam, V., and Huck, W. T. (2014). One drop at a time: toward droplet microfluidics as a versatile tool for single-cell analysis. *NPG Asia Materials*, 6(133):1–11.

- [Rashid et al., 2017] Rashid, Z., Coskun, U. C., Morova, Y., Morova, B., Bozkurt, A. A., Erten, A., Jonas, A., Akturk, S., and Kiraz, A. (2017). Guiding of emulsion droplets in microfluidic chips along shallow tracks defined by laser ablation. *Microfluid Nanofluid*, 21(160).
- [Richardson et al., 2010] Richardson, D. J., Nilsson, J., and Clarkson, W. A. (2010). High power fiber lasers: current status and future perspectives. *J Opt Soc Am B*, 27(11):B63–B92.
- [Roach et al., 2007] Roach, P., Shirtcliffe, N. J., and Newton, M. I. (2007). Progress in superhydrophobic surface development. *Soft Matter*, 4(2):224–240.
- [Russell, 2006] Russell, P. S. (2006). Photonic-crystal fibers. *J. Light. Technol.*, 24(12):4729–4749.
- [Schartner et al., 2011] Schartner, E. P., Heidepriem, H. E., and Monro, T. M. (2011). Low concentration fluorescence sensing in suspended-core fibers. In *Proc. SPIE 7753, Optical fiber sensors, 21*, pages 77534Q1–77534Q4, Ottawa, Canada.
- [Schrdoer et al., 1977] Schrdoer, H. W., Stein, L., Frölich, D., Fugger, B., and Welling, H. (1977). A high-power single-mode cw dye ring laser. *Appl. Phys.*, 14(4):377–380.
- [Shirtcliffe et al., 2003] Shirtcliffe, N., Mchale, G., Newton, M. I., and Perry, C. C. (2003). Intrinsically superhydrophobic organosilica sol-gel foams. *Langmuir*, 19(14):5626–5631.
- [Shirtcliffe et al., 2005] Shirtcliffe, N. J., McHale, G., Newton, M. I., Perry, C. C., and Roach, P. (2005). Porous materials show superhydrophobic to superhydrophilic switching. *Chem. Commun.*, 0(25):3135–3137.

- [Shuai et al., 2012] Shuai, B., Xia, L., Zhang, Y., and Liu, D. (2012). A multi-core holey fiber based plasmonic sensor with large detection range and high linearity. *Optics Express*, 20(6):5974–5986.
- [Sidram and Bhajantri, 2015] Sidram, M. H. and Bhajantri, N. U. (2015). Exploration of normalized cross correlation to track the object through various template updating techniques. *IOSR Journal of VLSI and Signal Processing*, 5(1):22–35.
- [Slaughter and Stevens, 2014] Slaughter, G. and Stevens, B. (2014). Comparison of hydrogen bonding in polydimethylsiloxane and polyether based urethane and urea copolymers. *Biochip J.*, 8(1):28–34.
- [Song et al., 2012] Song, W., Vasdekis, A. E., and Psaltis, D. (2012). Elastomer based tunable optofluidic devices. *Lab Chip*, 12(19):3590–3597.
- [Soz et al., 2015] Soz, C. K., Yilgor, E., and Yilgor, I. (2015). Influence of the coating method on the formation of superhydrophobic silicone–urea surfaces modified with fumed silica nanoparticles. *Prog. Org. Coat.*, 84:143–152.
- [Soz et al., 2016] Soz, C. K., Yilgor, E., and Yilgor, I. (2016). Simple processes for the preparation of superhydrophobic polymer surfaces. *Polymer*, 99:580–593.
- [Stolyarov et al., 2012] Stolyarov, A. M., Wei, L., Shapira, O., Sorin, F., Chua, S. L., Joannopoulos, J. D., and Fink, Y. (2012). Microfluidic directional emission control of an azimuthally polarized radial fibre laser. *Nature Photonics*, 6:229–233.
- [Sudirman and Margulis, 2014] Sudirman, A. and Margulis, W. (2014). All-fiber optofluidic component to combine light and fluid. *IEEE Photonics Technology Letters*, 26(10):1031–1033.
- [Sun et al., 2005] Sun, M., Luo, C., Xu, L., Ji, H., Ouyang, Q., Yu, D., and Chen, Y. (2005). Artificial lotus leaf by nanocasting. *Langmuir*, 21(19):8978–8981.

- [Sun et al., 2013] Sun, W., Zhou, S., You, B., and Wu, L. (2013). A facile method for the fabrication of superhydrophobic films with multiresponsive and reversibly tunable wettability. *J. Mater. Chem. A*, 1(9):3146–3154.
- [T. F. Johnston et al., 1982] T. F. Johnston, J., Brady, R. H., and Proffitt, W. (1982). Powerful single-frequency ring dye laser spanning the visible spectrum. *Applied Optics*, 21(13):2307–2316.
- [Tang et al., 2013] Tang, X., Wang, T., Yu, F., Zhang, X., Zhu, Q., Pang, L., Zhang, G., and Pei, M. (2013). Simple, robust and large-scale fabrication of superhydrophobic surfaces based on silica/polymer composites. *RSC Adv.*, 3(48):25670–25673.
- [Tang et al., 2014] Tang, X., Yu, F., Guo, W., Wang, T., Zhang, Q., Zhu, Q., Zhang, X., and Pei, M. (2014). A facile procedure to fabricate nano calcium carbonate–polymer-based superhydrophobic surfaces. *New J. Chem.*, 38(6):2245–2249.
- [Teh et al., 2008] Teh, S. Y., Lin, R., Hung, L. H., and Lee, A. P. (2008). Droplet microfluidics. *Lab Chip*, 8(2):198–220.
- [Than et al., 1988] Than, P., Preziosi, L., Josephl, D., and Arney, M. (1988). Measurement of interfacial tension between immiscible liquids with the spinning rod tensiometer. *Journal of Colloid and Interface Science*, 124(2):552–559.
- [Tsougeni et al., 2009] Tsougeni, K., Vourdas, N., Tserepi, A., and Cardinaud, C. (2009). Mechanisms of oxygen plasma nanotexturing of organic polymer surfaces: From stable super hydrophilic to super hydrophobic surfaces. *Langmuir*, 25(19):11748–11759.
- [Tullis et al., 2014] Tullis, J., Park, C. L., and Abbyad, P. (2014). Selective fusion of

- anchored droplets via changes in surfactant concentration. *Lab Chip*, 14(17):3285–3289.
- [Unger et al., 2000] Unger, M. A., Chou, H.-P., Thorsen, T., Scherer, A., and Quake, S. R. (2000). Monolithic microfabricated valves and pumps by multilayer soft lithography. *Science*, 288(5):113–116.
- [Van et al., 2017] Van, L. C., Anuszkiewicz, A., Ramaniuk, A., Kasztelanic, R., Xuan, K. D., Long, V. C., Trippenbach, M., and Buczyński, R. (2017). Supercontinuum generation in photonic crystal fibres with core filled with toluene. *Journal of Optics*, 19(12):1–9.
- [Vasdekis et al., 2007] Vasdekis, A. E., Town, G., Turnbull, G., and Samuel, I. D. W. (2007). Fluidic fibre dye lasers. *Optics Express*, 15(7):3962–3967.
- [Vezenov et al., 2005] Vezenov, D. V., Mayers, B. T., Conroy, R. S., Whitesides, G. M., Snee, P. T., Chan, Y., Nocera, D. G., and Bawendi, M. G. (2005). A low-threshold, high-efficiency microfluidic waveguide laser. *J Am Chem Soc*, 127(25):8952–8953.
- [Wellegehausen et al., 1974] Wellegehausen, B., Welling, H., and Beigang, R. (1974). A narrowband jet stream dye laser. *Applied Physics*, 3(5):387–391.
- [Worner, 2012] Worner, M. (2012). Numerical modeling of multiphase flows in microfluidics and micro process engineering: a review of methods and applications. *Microfluidics and Nanofluidics*, 12(6):841–886.
- [Wu et al., 2008] Wu, L., Tsutahara, M., Kim, L. S., and Ha, M. (2008). Three dimensional lattice boltzmann simulations of droplet formation in a cross-junction microchannel. *International Journal of Multiphase Flow*, 34(9):852–864.

- [Xing et al., 2011] Xing, S., Harake, R. S., and Pan, T. (2011). Droplet-driven transports on superhydrophobic-patterned surface microfluidics. *Lab Chip*, 11(21):3642–3648.
- [Xu et al., 2012] Xu, L., Lee, H., Panchapakesan, R., and Oh, K. W. (2012). Fusion and sorting of two parallel trains of droplets using a railroad-like channel network and guiding tracks. *Lab Chip*, 12(20):3936–3942.
- [Xu et al., 2009] Xu, Z., Shilpiekandula, V., Youcef-toumi, K., and Yoon, S. F. (2009). White-light scanning interferometer for absolute nano-scale gap thickness measurement. *Optics Express*, 17(17):15104–15117.
- [Xue et al., 2014] Xue, C.-H., Zhang, Z.-D., Zhanga, J., and Jia, S.-T. (2014). Lasting and self-healing superhydrophobic surfaces by coating of polystyrene/sio2 nanoparticles and polydimethylsiloxane. *J. Mater. Chem. A*, 2(36):15001–15007.
- [Yan et al., 2011] Yan, Y., Gao, N., and Barthlott, W. (2011). Mimicking natural superhydrophobic surfaces and grasping the wetting process: A review on recent progress in preparing superhydrophobic surfaces. *Adv Colloid Interface Sci.*, 169(2):80–105.
- [Yilgor et al., 2000] Yilgor, E., Burgaz, E., Yurtsever, E., and Yilgor, I. (2000). Comparison of hydrogen bonding in polydimethylsiloxane and polyether based urethane and urea copolymers. *Polymer*, 41(3):849–857.
- [Yilgor et al., 2012] Yilgor, I., Bilgin, S., Isik, M., and Yilgor, E. (2012). Facile preparation of superhydrophobic polymer surfaces. *Polymer*, 53(6):1180–1188.
- [Yonenaga et al., 2015] Yonenaga, Y., Fujimura, R., Shimojo, M., Kubono, A., and Kajikawa, K. (2015). Random laser of dye-injected holey photonic-crystal fiber. *Physical Review A - Atomic, Molecular, and Optical Physics*, 92(1).

- [Yoon et al., 2014] Yoon, D. H., Numakunai, S., Nakahara, A., Sekiguchi, T., and Shoji, S. (2014). Hydrodynamic on-rail droplet pass filter for fully passive sorting of droplet-phase samples. *RSC Advances*, 4(71):37721–37725.